THESIS FOR THE DEGREE OF DOCTOR OF PHILOSOPHY

Optical metasurfaces for momentum exchange between light and matter

Mahdi Shanei

Department of Physics
Chalmers University of Technology
Göteborg, Sweden, 2025

Optical metasurfaces for momentum exchange between light and matter

Mahdi Shanei
ISBN 978-91-8103-154-6

Doktorsavhandlingar vid Chalmers tekniska högskola
Ny serie nr 5612
ISSN 0346-718X

Division of Nano- and biophysics
Department of Physics
Chalmers University of Technology
SE-412 96 Gothenburg
Sweden
Telephone + 46 (0)31-772 1000

Cover:
On the left, a natural phenomenon in Baikal Lake, Siberia, demonstrates wind-assisted melting, forming a stable ice pillar that supports a flat rock. This occurs through isotropic melting, where ice melts uniformly in all directions under environmental conditions (permission from Olga Zimanaite). Similarly, on the right, this process is mirrored in nanofabrication, where isotropic etching of silicon beneath a flat spinner with metagratings on top is achieved using SF_6 plasma.

Printed in Sweden by
Chalmers digital printing
Chalmers Tekniska Högskola
Gothenburg, Sweden 2025

CHALMERS UNIVERSITY OF TECHNOLOGY

Department of Physics

Optical metasurfaces for momentum exchange between light and matter

Mahdi Shanei

Abstract

Light, despite being massless, carries both linear and angular momentum, allowing it to interact with matter in ways that induce tangible mechanical effects, such as translation and rotation. These effects are governed by the conservation of momentum, which dictates that any change in the momentum of light must be counterbalanced by a corresponding change in the momentum of the interacting material. Consequently, an optical force or torque can lead to observable mechanical translation and rotation. This thesis explores the reciprocal interaction between light momentum and matter, focusing on the manipulation of optical momentum through engineered subwavelength structures known as metasurfaces. This mutual exchange significantly influences both light and matter, offering opportunities to control one by altering the other.

Metasurfaces offer a wide range of possibilities for manipulating light momentum by modulation of the amplitude, phase, and polarization of transmitted and reflected light. They can also serve as compact replacements of traditional bulky elements, such as lenses and spatial light modulators. An example of this is demonstrated in the first appended paper, where a cylindrical metalens combined with a beam deflector is used to optically trap and transport particles along its line focus. Other examples, including the generation of holographic patterns and beam deflectors, are also presented in this report.

In the process of shaping a light beam, optical metasurfaces are often viewed as stationary elements that do not respond to the changing momentum of light. However, the metasurfaces themselves are subject to momentum exchange and reaction optical forces. This effect becomes evident when a metasurface is incorporated into a lightweight micro-scale object, called a *metaparticle*, which is free to move across a surface.

This thesis studies a new type of rotary metaparticle that can spin by redirecting linear photon momentum through pairs of beam deflector metasurfaces. These metaparticles consist of a transparent SiO_2 structure as the body, with embedded silicon metagratings to simulate the operational behavior of blazed gratings. Moreover, the second paper in this thesis investigates the collective behavior of spinning metaparticles, revealing unconventional orbiting patterns as they interact with each other. This study led to the discovery of a new type of optical gradient force, which acts perpendicular to the classical optical gradient force. Finally, the third paper demonstrates that the reaction optical forces generated by metagratings enable large metaparticles, up to 100 µm in diameter, to rotate by bending light at high angles. It is also shown that the torque generated by a rotor can rotate hundreds of passive microparticles in solution, suggesting potential applications for particle mixing in microfluidics.

The thesis is organized as follows: The first part is devoted to studying the fundamentals and developments of static optical metasurfaces by categorizing them based on various aspects, and the second part is dedicated to the study of optical forces and torques. The third part investigates the results that highlight the versatility of stationary and movable metasurfaces in facilitating optical manipulation of objects. Finally, the last chapter describes metasurface fabrication and characterization techniques, as well as various simulation methods used in this work.

Keywords: Flat optics, phase-gradient metasurface, metagratings, optical forces and torques, optical momentum exchange, metaparticle, rotary metamotor, particle transport.

List of publications

The following papers are included in this thesis:

I. Light-driven transport of microparticles with phase-gradient metasurfaces

Mahdi Shanei, Einstom Engay, and Mikael Käll

Optics Letters 47, no. 24 (2022): 6428-6431.

II. Transverse optical gradient force in untethered rotating metaspinners

Einstom Engay, Mahdi Shanei, Vasilii Mylnikov, Gan Wang, Peter Johansson, Giovanni Volpe, and Mikael Käll

Light: Science & Applications, accepted (2024).

III. Harnessing photon recoil for enhanced torque on light-driven metarotors

Mahdi Shanei, Gan Wang, Peter Johansson, Giovanni Volpe, and Mikael Käll

Submitted manuscript (2024).

Declaration of author contributions:

I: I did the nanofabrication, optimization and design of the metalenses, as well as numerical simulations. I assisted in the optical measurements and wrote the first draft of the manuscript.

II: I did the nanofabrication and sample characterization, and performed thermal and fluid dynamics simulations.

III: I developed the nanofabrication process, performed optical experiments, numerical calculations and simulations, and wrote the first draft of the paper.

List of supplementary publications

The following papers are not included in this thesis.

I. Directional control of transient flows generated by thermoplasmonic bubble nucleation

Pantea Dara, Mahdi Shanei, Steven Jones, and Mikael Käll

The Journal of Physical Chemistry C 127.35 (2023): 17454-17459.

My contribution: I performed the nanofabrication of plasmonic antennas.

II. Microscopic geared mechanisms

Gan Wang, Marcel Rey, Antonio Ciarlo, Mahdi Shanei, Kunli Xiong, Giuseppe Pesce, Mikael Käll, and Giovanni Volpe

arXiv:2409.17284 (2024).

My contribution: I assisted in nanofabrication and did thermal calculations.

III. Inverse design by machine learning improves the efficiency of microscopic metavehicles driven by lateral optical forces

Vasilii Mylinkov, Mahdi Shanei, and Mikael Käll

In manuscript (2024).

My contribution: I performed and optimized the nanofabrication, did the optical experiments, and analyzed the experimental results.

IV. On-chip light driven micromotor for microfluidic manipulation

Preliminary list of authors in alphabetical order: Antonio Ciarlo, Mikael Käll, Adrian Paskert, Giuseppe Pesce, Marcel Rey, Mahdi Shanei, Giovanni Volpe, Gan Wang, Raphael Wittkowski, Kunli Xiong

In manuscript (2024)

My contribution: I assisted in nanofabrication.

Acknowledgments

The past few years have been a remarkable journey of personal and scientific growth. I am deeply grateful to the many people who have inspired, guided, and supported me along the way.

Mikael. I am deeply grateful for giving me the time and resources to develop my skills. Thank you for your extensive support and for always keeping your door open. I could not imagine a better supervisor.

Daniel. Thanks for getting me started with my career and project. I am lucky that I have had your constant advice. Hope the best for you and your beautiful family.

Ruggero. Thank you for teaching me the art of nanofabrication and for being such a great buddy along the way.

Einstom and Vasilii. Thank you so much for the collaboration. It was a pleasure to work with you.

Special thanks to our group members. Pantea, Emelie, Khosro, Hana, Laura, Oliver, and Mindaugas. Also, big thanks to all the past group members.

Gan. I really enjoyed working with you on our shared project. I am looking forward to seeing your achievements. Hope the best for you and your wife.

I am thankful to Timur, Betül, Abhay, Tomasz, Sasha, Gosha, Michaela, Adriana, Santosh, Steven and Ximin. I feel so lucky to have known you all. Thank you for making our corridor a vibrant and enjoyable workplace with so many fun moments and fika breaks. Betül and Gosha, you are truly remarkable friends. I am so grateful for your friendship and kindness. I am also thankful to everyone else I’ve had the fortune to meet at NBP and GU.

Special thanks to Eva Olsson for her generous support and to Philippe Tassin, Giovanni Volpe and Peter Johansson for their ideas, suggestions and invaluable help.

Ankit and Ananthu. You are great friends and wonderful colleagues. I’m happy to have the opportunity to make more metastructures alongside you.

Hooman, Sara, Fatemeh and Gorji. I can't thank you enough for all the amazing fun and great moments we've shared. Your friendship has meant so much to me.

I am deeply grateful to my lovely parents; my appreciation is beyond words. To Sepide and Jana, for all the support through all these years.

Finally, to Jana: May this thesis inspire you in future as you inspire me every day. Stay curious and know that you have the power to bring happiness to the world around you. Just like the light I have studied; may you shine brightly in everything you do.

"Nature uses only the longest threads to weave her patterns, so that each small piece of her fabric reveals the organization of the entire tapestry."

Richard Feynman

Contents

Chapter 1

Introduction

The quest to interpret our observations of optical phenomena boils down to understanding the light-matter interaction. Materials science plays a pivotal role in advancing interdisciplinary fields, including optics and photonics. From the development of bronze and iron to the revolutionary discovery of semiconductors, materials science has consistently been an indispensable tool for improving human quality of life. When natural materials interact with light, their behavior can be described in terms of absorption and scattering. For instance, the vibrant colors of butterfly wings are often attributed to chemical pigments, such as melanin, which absorb and reflect specific wavelengths of light. However, another phenomenon, known as structural coloration, contributes to these striking appearances. Structural coloration arises from the interaction of light with periodic nanostructures in the wings. These layers, composed of periodic protein patterns, manipulate light through mechanisms such as interference and diffraction, producing vivid, iridescent hues [1, 2].

Figure 1.1: Natural and structural color of butterfly’s wing from melanin pigments and multi-layers of protein patterns shown in the insets [3].

Similar to butterfly wings, *metamaterials* represent an entirely new class of materials engineered to interact with light in ways not achievable with conventional materials. Unlike natural materials, metamaterials derive their unique properties from their artificial subwavelength structures. These three-dimensional building blocks are carefully designed to exhibit tailored interactions with electromagnetic waves, enabling phenomena such as negative refraction, cloaking, and superlensing [4, 5].

While the three-dimensional architecture of metamaterials has unlocked fascinating optical functionalities, it has some challenges in fabrication and scalability [6]. To address these limitations, researchers have turned their attention to *metasurfaces*, a two-dimensional version of metamaterials. Metasurfaces consist of optically thin arrays of subwavelength elements, designed to control the light propagation. The planar nature of metasurfaces not only simplify the fabrication process but also makes them compatible with conventional CMOS technology. This compatibility provides large-scale production and integration with existing optical systems, offering immense potential for applications in imaging, sensing, and telecommunications [7, 8].

The basic application of optical metasurfaces is beam shaping or structuring the wavefront of light. These flat surfaces can manipulate different degrees of freedom of light, including polarization, amplitude, and phase [9]. **Chapter 2** of this thesis delves into the development of optical metasurfaces, presenting their categorizations based on key aspects, including the materials used, phase control techniques, design methodologies, operational wavelengths, and their classification as active or passive devices. Furthermore, the chapter discusses various applications and the impact of metasurfaces on optical technologies. As a proof of concept, this chapter includes some of my own results obtained during the development and characterization of metasurfaces.

Metasurfaces not only allow for advanced light manipulation but also open new possibilities for controlling optical forces, which can arise from the momentum exchange between light and matter. This concept was first demonstrated by Arthur Ashkin in 1976 [10], who used it for levitating and confining particles, a breakthrough that earned him the Nobel Prize in Physics in 2018. But how exactly can light exert force on an object? A concise answer is momentum and lies in another Noble Prize in physics in 1921, where Einstein used Plank’s theory to explain the photoelectric effect. He introduced photons as quanta of light energy that can carry a well-defined momentum. Now, when a stream of millions of photons hits an object, the optical forces arise from the transferred momenta to that object.

These optical forces have revolutionized mechanical manipulation at the micro- and nanoscale. Techniques such as optical trapping, positioning, and sorting have garnered significant attention for their applications in fields such as therapy, drug delivery, diagnostics, and sensing [11-13]. Advances in these techniques depend on improving our ability to generate and control optical forces and torques. Given the various degrees of freedom of optical waves, this kind of actuation can be widely applied to manipulate objects at microscopic scales.

Hence, metasurfaces can play an important role in precisely applying optical forces and facilitating different types of momentum exchanges between light and matter. **Chapter 3** of this thesis explores the transfer of momentum from light to matter, with a focus on metasurface integrated into particles, referred to as *metaparticles*. Moreover, this Chapter deals with the interactions and dynamics of rotary metaparticles at low Reynolds numbers, where inertial effects are negligble because of the overwhelming role of viscosity. In order to get a feeling for this strange world, I refer to Purcell, "Life at low Reynolds number", whose insights into the physics of such systems are foundational [14].

> *"I want to take you into the world of very low Reynolds number a world which is inhabited by the overwhelming majority of the organisms in this room. It helps to imagine under what conditions a man would be swimming at, say, the same Reynolds number as his own sperm. Well, you put him in a swimming pool that is full of molasses, and then you forbid him to move any part of his body faster than 1 cm/min. Now imagine yourself in that condition; you're under the swimming pool in molasses, and now you can only move like the hands of a clock. If under those ground rules, you are able to move a few meters in a couple of weeks, you may qualify as a low Reynolds number swimmer."*

After exploring the fundamentals of optical forces and torques, **Chapter 4** presents experimental validations of optical manipulation through metasurfaces. The chapter begins with an overview of various actuation mechanisms for manipulating micro- and nanoscale objects, followed by a classification of optical manipulation using metasurfaces into two categories: stationary and movable metasurfaces. Figures 1.2 (a-d) depict several illustrations of optical manipulation with metasurfaces, highlighting the different degrees of freedom of the light beam.

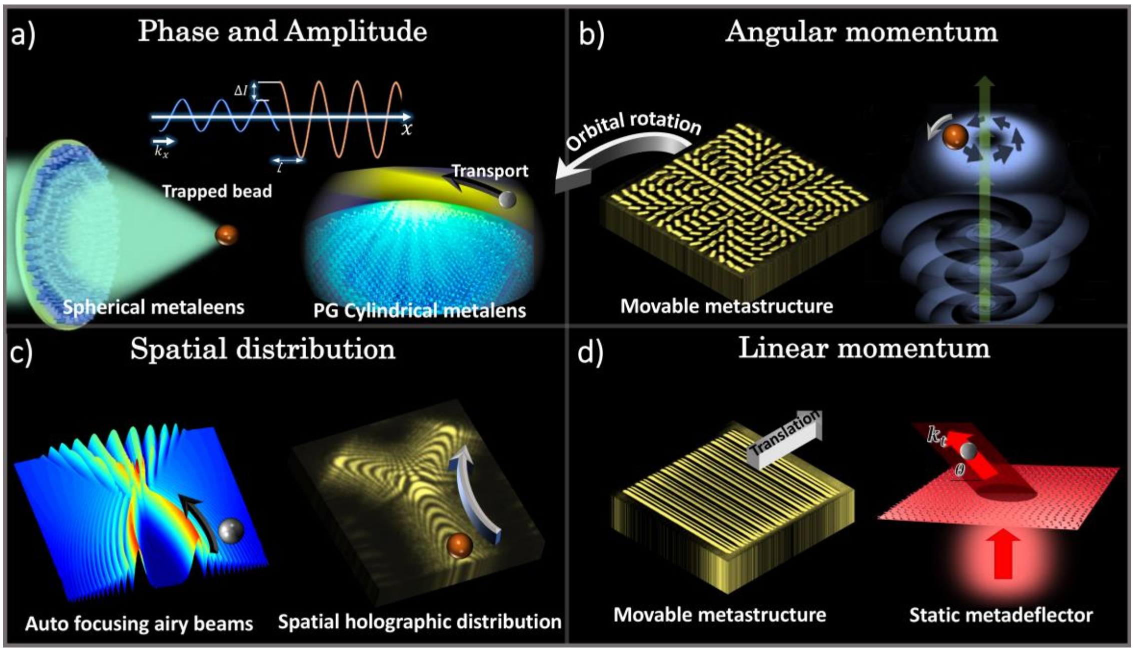

Figure 1.2: Illustration of the optical manipulation with metasurfaces based on different degrees of freedom of light beam. (a) Spherical metalens that provides three-dimensional confinement of particles (left side). Cylindrical metalens with a phase gradient along its focal line to confine and transport particles (right side). (b) Free particle with an embedded metasurface can orbit around the optical axis of the propagating helical beam (left side). A vortex beam from a static metasurface can orbit the beads in the bright area (right side). (c) Particle transport by two symmetric Airy beams and confinement in the focal area constructed by the constructive interferences of two beams (left side). Particle transport in a Y-shaped holographic pattern with a phase gradient inside branches (right side). (d) Free particle translates in the opposite direction of the deflection of the light by the embedded gratings inside the body of the particle (left side). Static metasurface that can move the particle by the radiation pressure in the illustrated direction (right side).

Conducting research in interdisciplinary fields like nanobiophotonics necessitates a multifaceted approach that combines numerical simulation, micro and nanofabrication, and experimental characterization. Each of these components plays a crucial role in advancing our understanding and achieving meaningful results. **Chapter 5** provides an overview of the research methodologies employed in this work. It details the numerical simulation and calculation techniques used to optimize, model, and predict the behavior of target metasurfaces and their performance. Additionally, it covers the micro and nanofabrication processes utilized to construct the necessary structures. This chapter also describes the experimental optical setups that were crucial for validating the theoretical predictions and characterizing the fabricated samples. **Chapter** **5** outlines the approach taken to achieve the findings presented in the appended papers. Lastly, **Chapter** **6** summarizes the appended papers and reflects on them based on a wider outlook by highlighting some tracks for the continuation of this field in the future.

Chapter 2

Flat optics and metasurfaces

Beam shaping with refractive optical components relies on the gradual phase accumulation achieved through light propagation over a distance significantly larger than the effective wavelength of light. Fabricating these elements requires precise surface polishing and alignment, often resulting in bulky and expensive components. In contrast, diffractive optics, designed with features on the scale of the light's wavelength, offer a lightweight and compact alternative [15]. However, diffractive optics suffer from the propagation of undesired spurious diffraction orders, leading to a reduction in efficiency and the emergence of ghost and virtual focal points in imaging systems [16-18]. These limitations necessitate further advancements to improve performance.

To achieve better control over beam propagation, three-dimensional metamaterials with engineered optical and electrical properties have emerged as a promising solution. These metamaterials are artificially structured materials composed of subwavelength-scale elements. In the optical field, this can usually be achieved through the spatial modification of the dielectric function of material[19]. Metamaterials are often constructed by stacking multiple layers to achieve the desired properties. This has several drawbacks, in particular a complicated fabrication process [20, 21].

The advent of flat metasurfaces, a two-dimensional version of metamaterials, provides promising possibilities for tackling the disadvantages of metamaterials. Metasurfaces consist of individual subwavelength elements, also called metaatoms, that are patterned on a two-dimensional substrate [22, 23]. Contrary to metamaterials, metasurfaces introduce abrupt changes in the amplitude, phase, and polarization of the incident wavefront because of their ultra-thin thicknesses. Metasurfaces have the potential to provide a versatile platform for different applications and scopes in optics and photonics [22]. Due to this, they have gained remarkable attention in the past decade. Features such as multifunctionality, tunability, flexibility in design, and high sensitivity make them a hot developing topic in the current literature of flat optics. In the following sections of this chapter, the development of metasurfaces is described and discussed by dividing them into different groups based on their properties and performance [24, 25].

2.1 Full-phase coverage approaches

Conventional optical refractive elements, such as lenses, can shape the phase profile of the beam wavefront by introducing different spatial phase accumulations through a curved structure. In metasurfaces, the individual planar metaatoms are instead responsible for providing the phase changes that are required to shape the wavefront. Various approaches have been used to introduce full 2π phase coverage by utilizing strong light-matter interactions between the building blocks of the metasurface and the incident wave. These techniques can be categorized into three main approaches, resonance, propagating, and geometrical, or Pancharatnam Berry (PB), phases for dielectric metasurfaces [26]. It is worth mentioning that there is also a hybrid technique combining propagating and resonance phase methods [27].

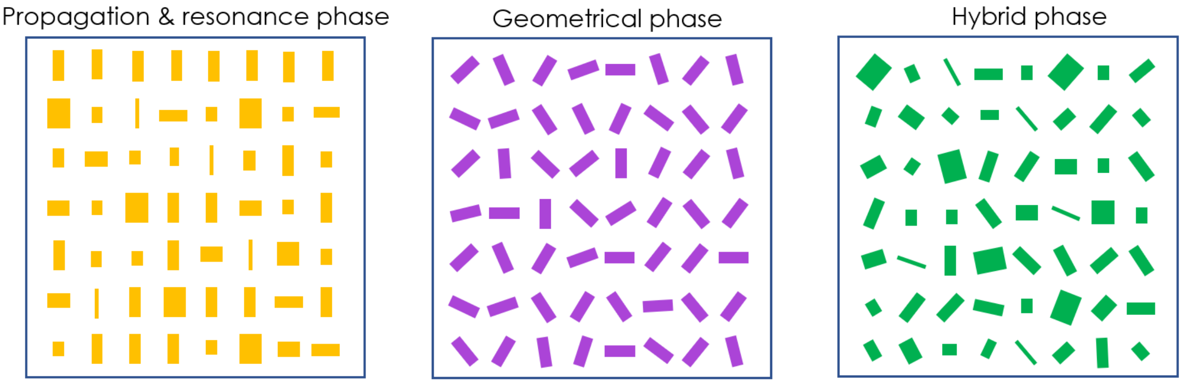

Figure 2.1: Three methods to print the required amplitude and phase modulation on a surface. Left: Different cross-sections have been used to engineer the effective refractive index of light. Metaatoms in the propagation phase approach generally have a higher aspect ratio than the ones in resonance phases. Middle: Geometrical phase technique uses the rotation of a specific metaatom in a plane perpendicular to the propagation of the incident light. Left: The hybrid phase approach combines geometrical and propagation techniques to simultaneously modulate the phase and amplitude of impinging beam [28].

Figure 2.1 schematically illustrates various techniques, shown through top views of different metasurfaces.

2.1.1 Propagating phase

The propagating phase approach is based on the simple definition of the optical path length and the accumulated phase, where they vary proportionally with the refractive index of the medium. Hence, the building blocks in a metasurface can arbitrarily define the phase of extracted beams by modulation of the effective refractive index by varying the filling factors. The phase delays can be calculated by

$$\phi_{\mathrm{WG}} = \frac{2\pi}{\lambda} n_{\mathrm{eff}} H, \tag{2.1}$$

where λ, H and n_{eff} are the vacuum wavelength, the thickness and the effective refractive index of a metaatom, respectively. The effective refractive index for a rectangular metaatom with a cross-section $a \times b$ in a square lattice with lattice constant c is

$$n_{eff} = \frac{n_m(a \times b) + n_s\,(c^2 - a \times b)}{c^2}, \tag{2.2}$$

where $n_m\ and\ n_s$ are the refractive indices of the metaatom and its surrounding medium, respectively. In this approach, the existence of Fabry–Pérot or Mie resonances can disturb the performance of metaatoms in providing ϕ_{WG} as expressed in Equation (2.1). So, to realize a metasurface with the propagation phase approach, it is necessary to implement electrodynamic simulations. It is worth mentioning that this method can also provide a polarization-sensitive metasurface [29-31].

2.1.2 Resonance phase

The early stage of phase gradient metasurfaces focused on resonance phases in plasmonic metaatoms [18]. Later, this technique was implemented for dielectric metaatoms, which support different orders of electric and magnetic Mie resonances [32, 33]. The interaction of the incident field with these resonance modes introduces phase discontinuities. For example, the phase of the scattered field can jump π and $\pi/2$ after interaction with dipole and quadrupole modes, respectively.

The frequency dependent field transmittance and reflectance coefficients of the first electric and magnetic Mie resonances can be written as

$$t(\omega) = 1 + \frac{2i\gamma_{\mathrm{e}}\omega}{\omega_{\mathrm{e}}^2 - \omega^2 - 2i\gamma_{\mathrm{e}}\omega} + \frac{2i\gamma_{\mathrm{m}}\omega}{\omega_{\mathrm{m}}^2 - \omega^2 - 2i\gamma_{\mathrm{m}}\omega} \tag{2.3}$$

$$r(\omega) = \frac{2i\gamma_{\mathrm{e}}\omega}{\omega_{\mathrm{e}}^2 - \omega^2 - 2i\gamma_{\mathrm{e}}\omega} - \frac{2i\gamma_{\mathrm{m}}\omega}{\omega_{\mathrm{m}}^2 - \omega^2 - 2i\gamma_{\mathrm{m}}\omega}, \tag{2.4}$$

where γ_{e} and γ_{m} are damping parameters of electric and magnetic resonances with spectral position ω_{e} and ω_{m}. By tuning the geometrical parameters of an individual metaatom, these resonances can destructively overlap (ω_{e}=ω_{m}) with each other. In this case, if they have a similar spectral profile with an equal damping factor, zero backward scattering is accessible that facilitates the construction of an efficient metasurface. In the resonance phase method, the realization of 2π phase coverage can be achieved when a magnetic dipole resonance with π phase delay overlaps with an electric dipole resonance with another π phase delay [34].

2.1.3 Geometrical phase

Since the discovery of the geometrical phase by Pancharatnam in 1956 [35] and the generalization of that by Berry in 1984, the so-called Pancharatnam-Berry (PB) approach has become a prevalent method to analyze the propagation of waves. The PB phase describes the contribution of the polarization state of light in the phase modulation when it is twisted via a structure. To rotate the polarization state, light should travel through an anisotropic metaatom where it experiences different refractive indices in the principal axes of the unit cell. When the metaatom rotates with an angle of θ, an additional 2θ phase delay will be added to the propagated wave. To interpret the contribution of rotation angles in the phase modulation, the transmission matrix for a metaatom with a rotation angle of θ can be written as

$$\begin{aligned}\hat{t}(\theta) &= \hat{R}^{-1}(\theta)\begin{pmatrix} t_{\mathrm{u}} & 0 \\ 0 & t_{\mathrm{v}} \end{pmatrix}\hat{R}(\theta) \\ &= \begin{bmatrix} t_{\mathrm{u}}\cos^2\theta + t_{\mathrm{v}}\sin^2\theta & (t_{\mathrm{u}} - t_{\mathrm{v}})\sin\theta\cos\theta \\ (t_{\mathrm{u}} - t_{\mathrm{v}})\sin\theta\cos\theta & t_{\mathrm{u}}\sin^2\theta + t_{\mathrm{v}}\cos^2\theta \end{bmatrix}.\end{aligned} \tag{2.5}$$

Here $\hat{R}(\theta)$ is the rotation matrix and t_u and t_v refer to the complex field transmission for light polarized parallel and perpendicular to the long in-plane axis of the anisotropic metaatom. For more details about the derivation 2θ phase delay, see [36, 37].

2.2 Materials and operating wavelengths

Development of metasurfaces started by utilizing plasmonic antennas as building blocks to provide full 2π phase coverage. Although the transmitted light can be artificially modulated by controlling the geometric parameters of plasmonic structures, they suffer from large ohmic losses that limit their efficiency [38].

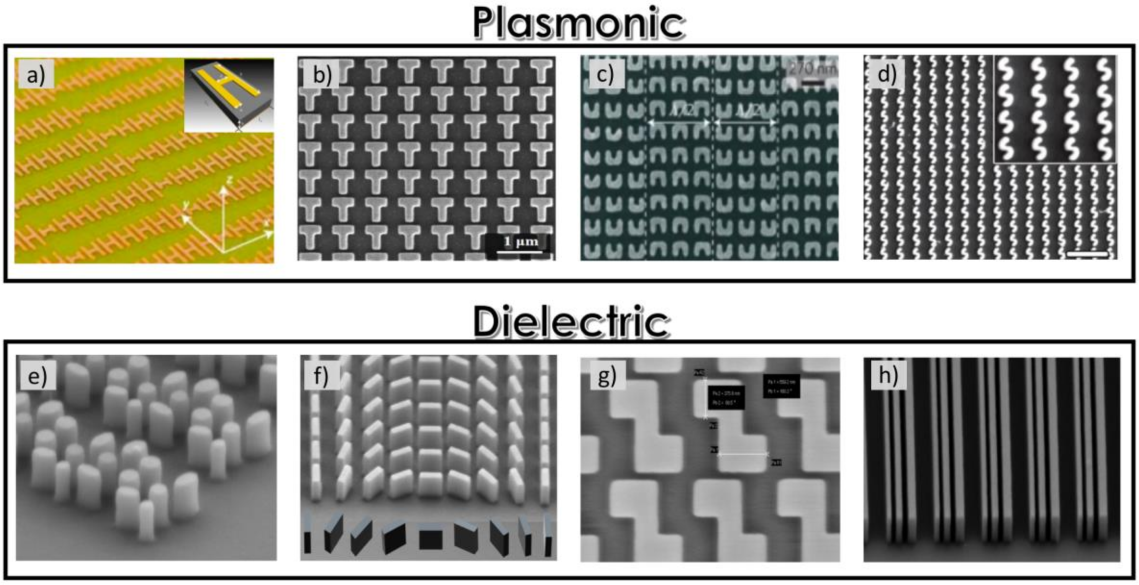

Figure 2.2: Different types of metasurfaces. Plasmonic structure in the top box and silicon-based dielectric metasurfaces in the second box. (a) H-shaped antenna array as a connection to link propagating waves to the surface waves [39] © 2012, Nature. (b) T-shaped metaatoms for polarization conversion [40] © 2017, Nature Materials. (c). U-shaped split-ring resonators with strong magnetic resonance [41] © 2015, Nature Photonics. (d) S-shaped metasurface to excite toroidal resonances [42] © 2021, Advanced Optical Materials. (e-h) Fabricated silicon-based metasurfaces (Shanei, et al., unpublished data). (e) circular and elliptical metaatoms to bend the light, (f) nano-fins as a phase gradient beam deflector patterned by geometrical phase approach, (g) chiral structure by periodic z-shaped metaatoms and (h) elongated bars as metagratings.

So, the direction of development switched to rendering dielectric metaatoms to improve the efficiency of the metasurfaces. Figure 2.2 illustrates some of the earliest works in plasmonic metasurfaces.

To support the extensive phase coverage required for beam shaping and highly efficient devices, the materials used for constructing dielectric metasurfaces need to have a high refractive index (n) and low extinction coefficient (k). Typical materials used for dielectric metasurfaces are shown in Figure 2.3, considering their refractive indices and operating wavelengths. Commonly used materials such as Si, GaN, GaAs, TiO_2 are briefly explained in the following parts.

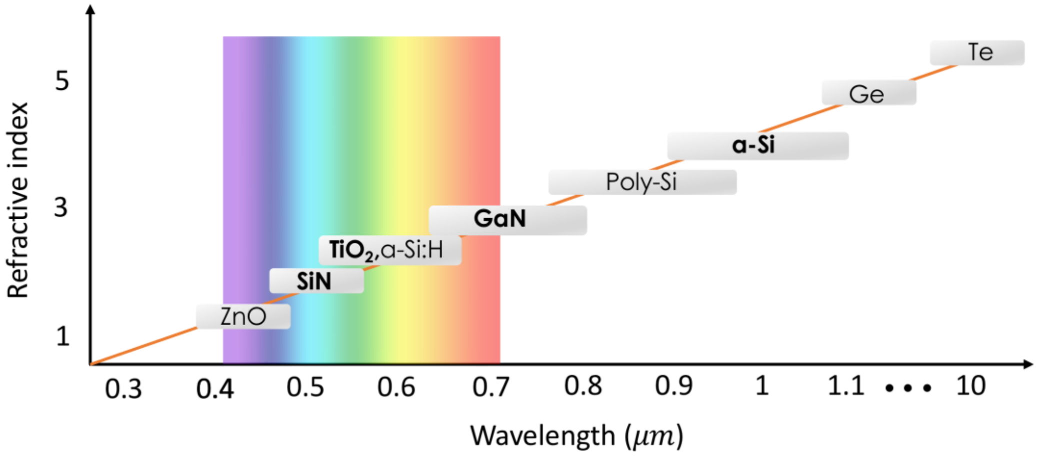

Figure 2.3: High-index dielectric materials used for metasurfaces. Silicon-based metaatoms are a useful option for IR and near-IR wavelengths because of low absorption and high refractive indices [43-45]. These kinds of metasurfaces can also be implemented as Huygens' metasurfaces with a low aspect ratio [46]. TiO_2-based metasurface with lower refractive index (at visible) in comparison to silicon (at infrared) usually consists of truncated waveguide resonators with propagating modes [31, 47-50]. GaN and GaAs have a favorable refractive index for making highly efficient metasurfaces in the red and near-IR [51-53]. SiN-based metasurfaces have lower efficiency than other dielectric metasurfaces, which can be used for long wavelengths in the visible spectrum [54-56].

Si-based metasurfaces

Fabrication of Si metasurfaces is compatible with CMOS technology and, later, a suitable material for integrating with other silicon-based optical devices. Due to the low extinction of silicon at near-infrared frequencies, they are good candidates as a constitutional element for highly efficient metasurfaces.

TiO_2-based metasurfaces

TiO_2 is optically transparent at visible wavelength with a small extinction coefficient, making it the best candidate to use in most metasurfaces, which work at green to red wavelengths. Since this material is chemically more stable than silicon, a hard mask should be used in the fabrication process of TiO_2 metasurfaces that add complexities to its fabrication process.

GaN and GaAs-based metasurfaces

GaN and GaAs can be suitable replacements for TiO_2 metasurfaces when the fabrication complexity determines the material and type of metasurfaces. The fabrication process of this material is compatible with LED and laser technologies and can be a low-cost option for metasurfaces. These materials also have much lower losses at visible wavelength than their silicon counterparts. These metasurfaces are suitable for integration with other photonics devices, such as vertical-cavity surface-emitting lasers (VCSELs) [57, 58].

SiN-based metasurfaces

SiN with a band gap of 2 eV is a good candidate for the building blocks of metasurfaces when thermal stability and some mechanical properties are important for the target application. This material is less transparent in comparison with TiO_2 and GaN materials. SiN metasurfaces have been suggested for space applications [59].

2.3. Design methodologies and configurations

In the current literature, methods to find a suitable building block for a metasurface are divided into two techniques: forward and inverse designs. Usually, forward or conventional techniques implement full-wave numerical analysis with topological parameter sweeps and optimization algorithms. However, this technique is usually useful for meta-devices with applications such as focusing (metalens) or bending (meta-deflector). It is time-consuming if the aim is to design a multifunctional, broadband, or tunable metasurface. Therefore, developing an accurate, fast, and efficient approach that finds a proper building block to enable a versatile metasurface is essential. Inverse design can be an excellent method to tackle the drawbacks of conventional forward techniques where the optical response of the metasurface serves as input and the structural geometry and feature sizes are the outputs [60-62]. Figure 2.4 summarizes the required steps for the forward design method.

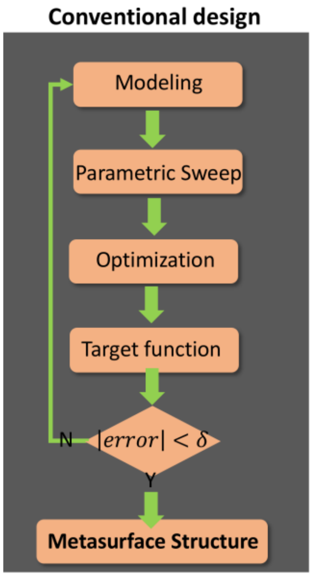

Figure 2.4: Forward technique to design the building block of the metasurface by using topological optimization data [63].

The next step after obtaining a library of proper metaatoms is their arrangement on a surface. Usually, the configuration of metasurfaces is determined by the function of required phase and/or amplitude profiles. A straightforward method to decorate a metasurface is discretizing a surface based on the metaatom lattice constant and then distributing the building block over the surface to generate the required phase and/or amplitude masks. Although this method works properly for static, single wavelength/function meta-devices, there is a demand for adding other degrees of freedom to have multi-wavelength/functions and tunable platforms. Figure 2.5 illustrates some techniques that are used to enhance the functionality of the metasurface, such as dividing the surface into different areas [64], interleaving metaatoms [65, 66], and using multi-layer [67, 68] or reconfigurable metasurfaces [69-71].

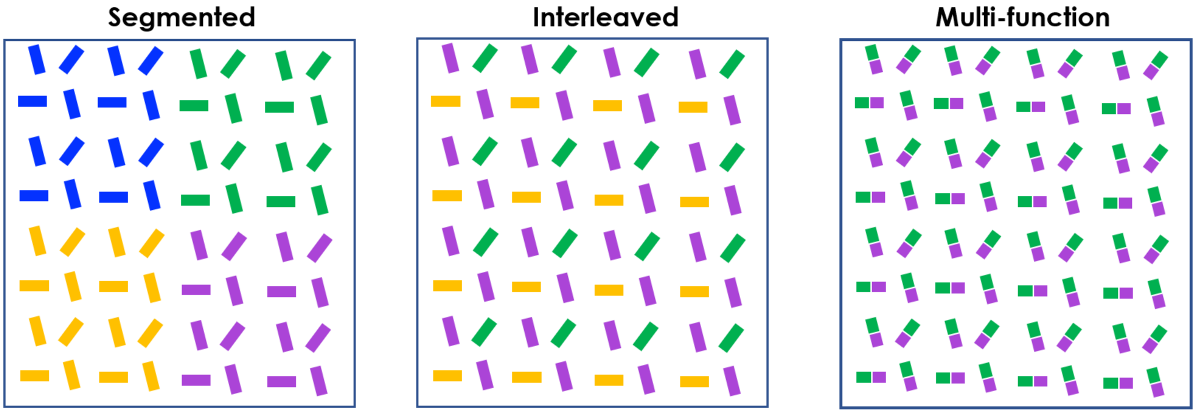

Figure 2.5: Examples of configuration techniques to enhance the functionality of metasurfaces by dividing metasurface into different segments (left box), multiplexing metaatoms into a unit cell (middle box) and multi-function metaatoms (right box).

2.4. Passive and active metasurfaces

While a passive metasurface generally presents a single function, an active type enables dynamic modifications of functions and performances based on different actuation mechanisms. For example, Figure 2.6 shows various adaptive devices such as passive, switchable, and tunable metalenses.

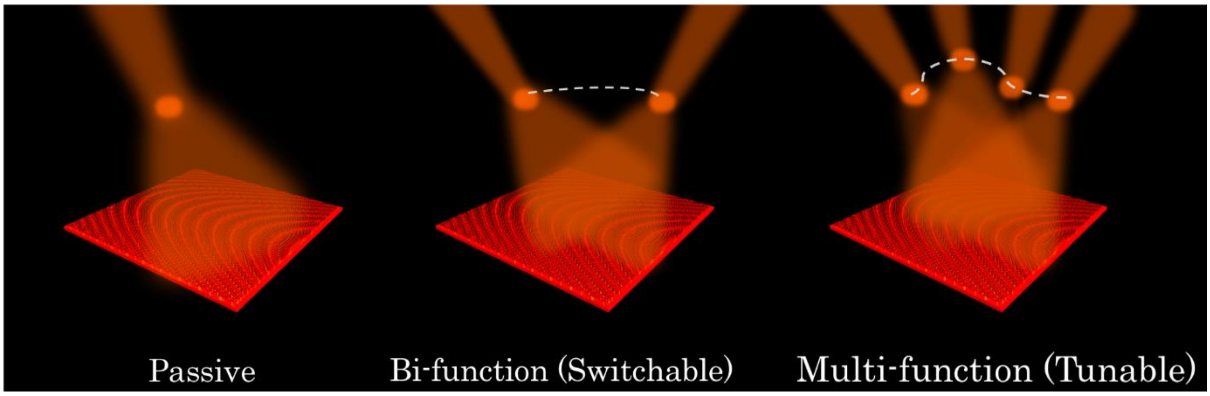

Figure 2.6: Examples of a passive meta-device on the left and two adaptive devices of switchable and tunable metasurface on the right side.

The potential of metasurfaces in the active tuning of performance makes them a versatile platform compared with conventional bulky systems. During the past decade, significant parts of research in metasurfaces have been dedicated to the development of active devices. Figure 2.7 shows statistics for the total number of papers for passive and active metasurfaces.

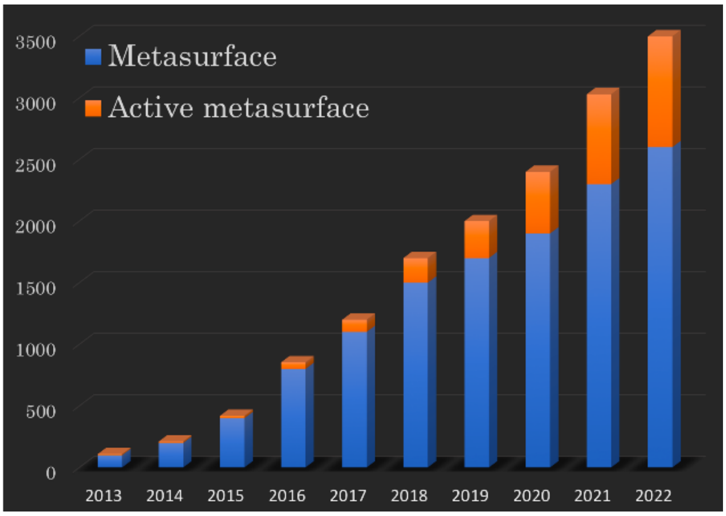

Figure 2.7: Comparison between the development of metasurface and its active types through the number of published papers extracted from the web of science (WOS) from 2013 to 2022.

To convert a passive metasurface into an active one, different methods can be implemented to design a metasurface, such as reconfiguring or rearranging the metaatoms or changing the surrounding environment of metasurface or using active phase-change materials (PCM). PCM based-metasurfaces are the most prevalent example of the active metasurface, which is related to implementing a tunable material such as liquid crystal, 2D materials, and semiconductors as an additional layer or building block of the metasurface. An external excitation can modulate the properties of these materials via electrical, optical, or thermal fields. Table 2.1 summarizes some of the articles in the literature on active metasurfaces based on tuning mechanism, speed, efficiency, working wavelength, and phase coverage [72, 73].

Method	Phase shift	Working wavelength	Efficiency	Speed range	Function	Drawbacks
Electrical tuning based on conducting oxide	300	NIR	<30%	GHz	Beam deflector Lens	Low efficiency Reflection mode
Electrical tuning base on 2D material	240	NIR	50%	GHz	Lens Absorber	Limited wavelength
Electrical tuning based on LC	360	Visible to NIR	36%	KHz	Color filtering SLM	Slow switching
Phase change material	70	Visible to NIR	75%	KHz	Bifocal lens Holography	Slow switching Non compatible
Mechanical Reconfigurable	300	Visible to THz	90%	MHz	Filters Lens	Difficult actuation installation
Flexible metasurface	360	Visible to NIR	90%	-	Color filter Lens	Sensitive Low speed
Nonlinear effect	360	NIR	<10%	Hz	Optical switch Frequency conversion	Low efficiency
Transition metal	90	Visible to NIR	35%	Hz	Holography Beam bending	Slow speed
Microfluidic based	-	Visible to NIR	55-70%	Hz	Color display	Low efficiency

Table 1: Review of recent papers in active metasurfaces based on tuning mechanism, phase coverage, working wavelength, efficiency, modulation speed, target function and limitations. The table is extracted from [72, 73].

Lastly, the chiral structures can selectively respond to light due to its polarization-dependent behavior. Chiral metasurfaces consist of inherently passive metaatoms which take the polarization state of light as a tuning knob to demonstrate a tunable performance [44, 74-78]. Figure 2.8 shows a chiral silicon metasurface that acts as a partial reflector and transmitter for right and left-handed circularly polarized light, respectively.

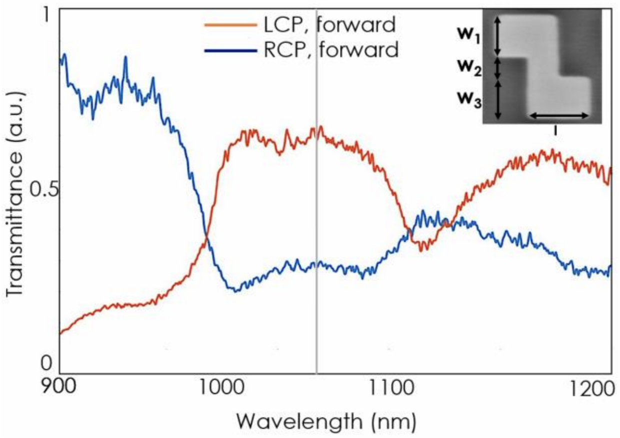

Figure 2.8: Simulation results of transmission spectra of periodic z-shaped metaatoms. At 1064 nm, the metaatom can actively partly transmit or reflect by switching the incident polarization. SEM image of fabricated subwavelength silicon metaatom is shown in the inset with a thickness of 500 nm, periodicity 800 nm of w_1 and $w_3 = 260$ nm, $w_2 = 150$ nm and $l = 500$ nm (Shanei, et al., unpublished data).

2.5. Applications and research frontier

After developing fundamental understanding of metasurfaces, researchers mostly focused on basic applications, such as focusing, bending, and other kinds of beam shaping, as illustrated in Figure 2.9. Beam shaping with phase gradient metasurfaces is the basis of different applications, such as imaging [79], spectroscopy [80], and particle manipulation [13, 81-84].

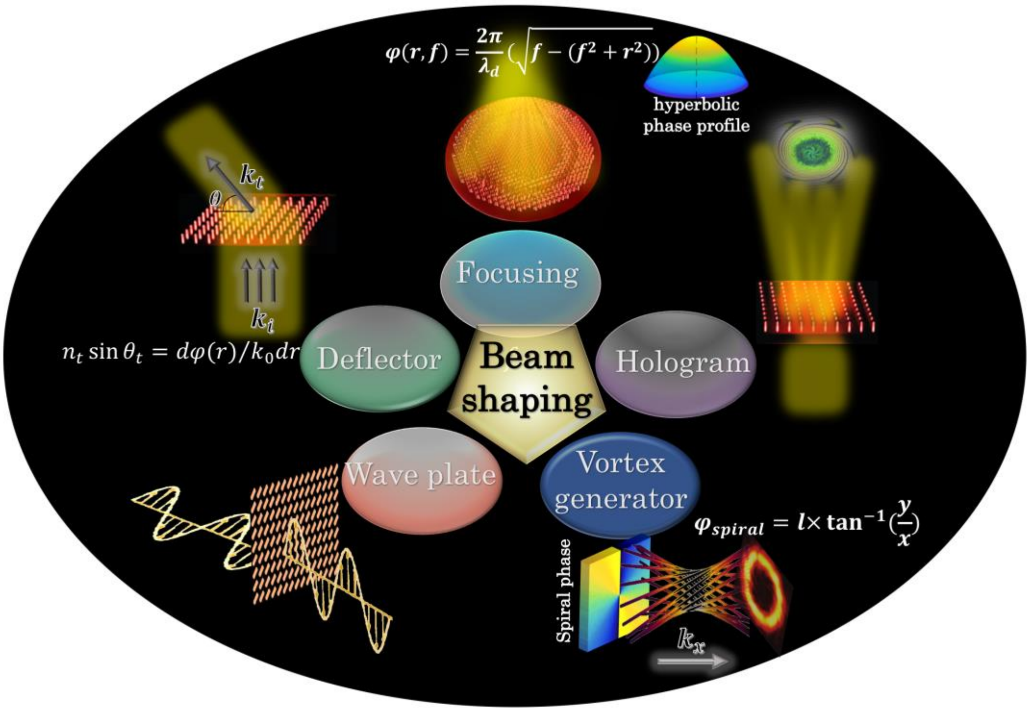

Figure 2.9: Illustration of different applications of optical metasurfaces based on wavefront shaping. Top: Spherical metalens with hyperbolic phase profile of $\varphi(r,f)$ produces a spot at focal length f. Left: Meta-deflector bends a normal incident beam at an angle of θ_t in a medium with a refractive index of n_t. Right: Holographic circular ring achieved by defining a phase mask derived from computer-generated holography calculations. Bottom left: Half-wave plate based on a periodic array of metaatoms oriented at 45° to the incident polarization. Bottom right: Vortex beam generator achieved by implementing a spiral phase profile $\varphi(x,y)$ with topological charge l.

The main focus of this thesis is to explore the use of optical forces and torques facilitated by metasurfaces through the precise manipulation of a beam's wavefront. Accordingly, the following sections briefly study selected examples that demonstrate how metasurfaces can effectively shape and tailor a beam's wavefront.

2.5.1 Beam focusing with metasurfaces

The phase modulation of a metasurface must span a complete 2π range to effectively reshape an incident wavefront into any desired profile. One key application of wavefront shaping with metasurfaces is focusing light to create metalenses, which have unlocked new possibilities in various fields, including optical tweezers. In recent years, various demonstrations have been presented by different groups [85] where the phase profile of Equation (2.7) has been used to focus a plane wave into a point:

$$\varphi(r_0) = -\frac{2\pi}{\lambda}\left(\sqrt{r_0^2 + f^2} - f\right). \tag{2.7}$$

Here f, λ and r_0 are the focal length, operating wavelength and radial coordinate, respectively. If the x and y-coordinate contribute to the radial position of r_0, the structure constructs a spherical lens with a single focal spot. When the arrangement of metaatoms is based on one coordinate in Equation (2.7), the scattered waves interfere constructively at a focal line resulting in a cylindrical lens.

2.5.2 Beam bending with metasurfaces

The advent of metasurfaces started with the generalization of Snell's law in 2011 [9], where an in-plane phase gradient of $\frac{d\varphi}{dy}$ is considered at the interface of two media with the refractive indices n_t and n_i in y-direction. In this case, by considering Fermat's principle, the variation of the phase gradient can be written as

$$n_t sin(\theta_t) - n_i sin(\theta_i) = \frac{1}{k_0}\frac{d\varphi}{dy}. \tag{2.8}$$

Here, by considering the first and second terms in Equation 2.8 as the wavevectors of the incident and transmitted beam in the y-direction, the generalized Snell's law can be simplified into

$$\Delta k = k_o - k_i = \frac{d\varphi}{dy}\hat{y}. \tag{2.9}$$

2.5.3 Angular momentum manipulation

An optical beam that carries an orbital angular momentum is usually constructed using spatial light modulators or bulky spiral plates. Vortex beam generating metasurfaces have been introduced as a compact replacement during the past few years. By creating the required phase profile using the metasurface, a plane wave can be converted to a Laguerre–Gaussian beam, possessing an angular momentum.

Figure 2.10 shows the spiral phase profile required for a simple vortex beam generator and the addition of the axicon and lens profile, which are needed for a perfect vortex beam metasurface. Perfect vortex beam metasurfaces can generate beams that propagate with annular intensities that remain fixed in size with propagation distance, as shown in the middle panel of Figure 2.10. The third panel in Figure 2.10 demonstrates the optical images of spiral metasurfaces with topological charges of 2, 4 and 8 together with a SEM image related to $l = 2$.

Topological charges can play an important role as a knob to tune the optical torque. A vortex metasurface can also facilitate the spinning of a trapped particle around the optical axis. This can be achieved by adding a focusing phase profile to the Laguerre–Gaussian beam generator. In this case, the radius of the bright field at the target plane can be changed by modifying the focal distance.

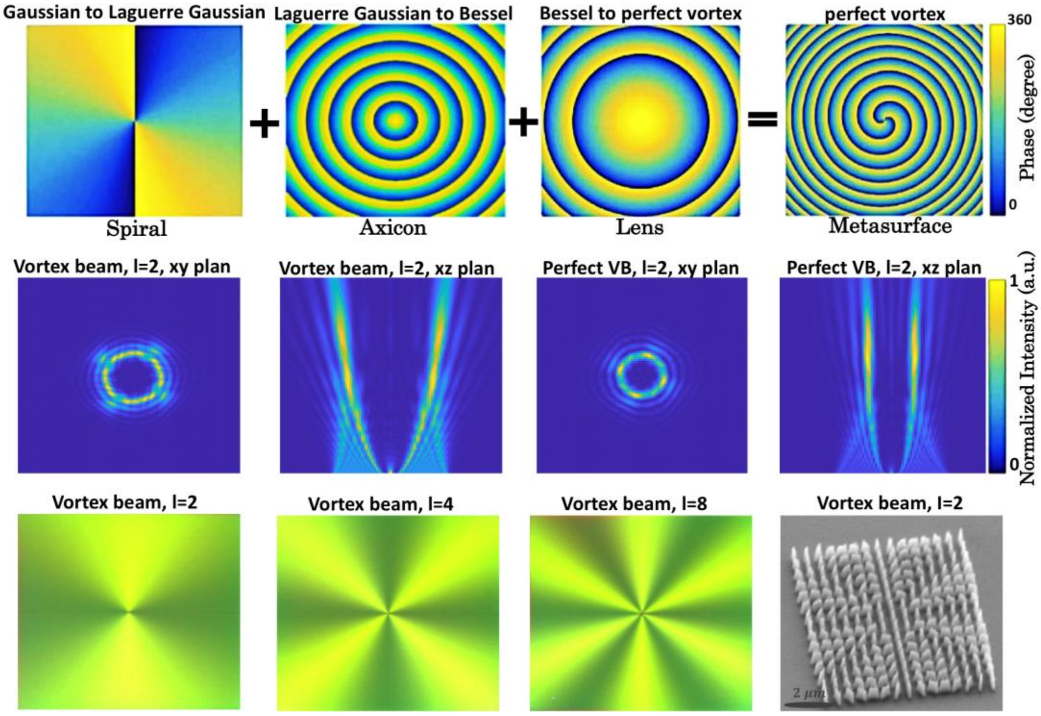

Figure 2.10: Top panel shows the spiral phase profile to construct a Laguerre Gaussian beam. The addition of an axicon phase profile and focusing can reach a perfect vortex beam generator metasurfaces. Vortex and perfect vortex beam with the topological charge of 2 at xy and xz-plane. The third panel demonstrates the optical images of a spiral metasurface with topological charges of 2, 4 and 8, together with a SEM image related to $l = 2$ (Shanei, et al., unpublished data).

2.5.4 Holographic metasurfaces

Like a metalens with engineered spatial phase distribution, a meta-hologram provides arbitrary intensity patterns even in three dimensions. The metasurfaces are a good candidate for introducing amplitude and phase masks for holographic optical tweezers. A simple phase-only holographic metasurface can be designed by considering the field distribution using Fraunhofer diffraction theory. To provide more flexibility in manipulating the particles, computer-generated holography (CGH) has been developed to define amplitude and phase masks which can later be implemented by the arrangement of metaatoms. Figure 2.11 shows the target phase and amplitude profiles used to feed the CGH algorithm. The CGH algorithm generates a phase profile to reconstruct the main amplitude and phase profile. Figure 2.11 shows two different reconstruction models (calculated by Qiang Jiang from the Beijing Institute of Technology) based on the amplitude and phase quality at the target planes. The optical images of fabricated metasurfaces for each model are shown in Figure 2.11.

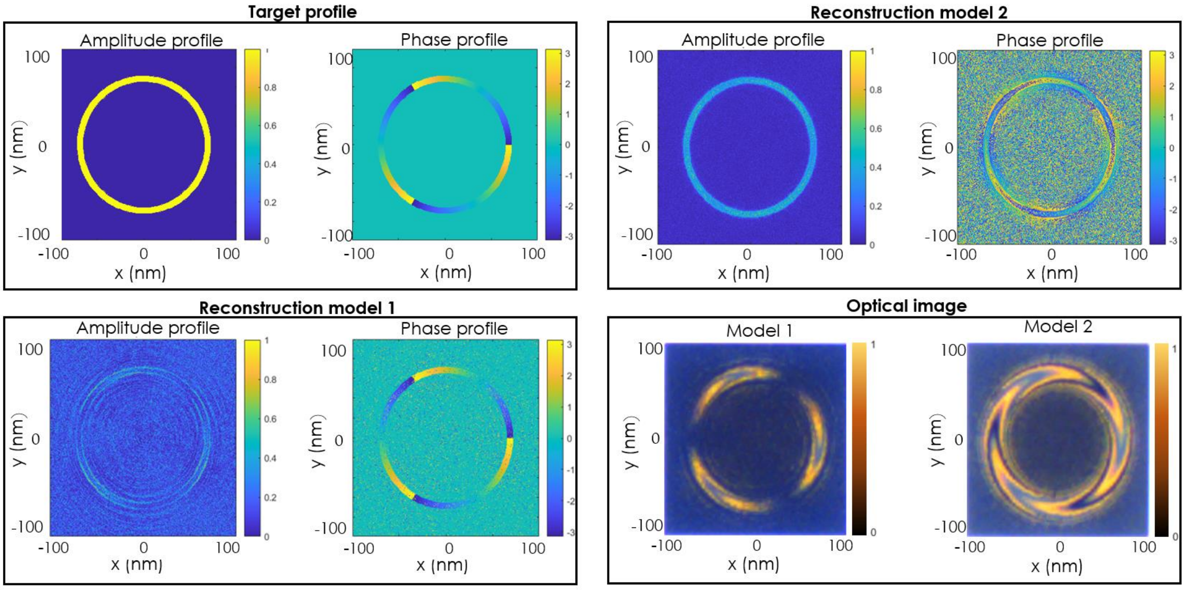

Figure 2.11: Target phase and amplitude profiles to construct with a 0 to 6π phase gradient along the circular path of the ring focus. Two reconstruction models related to the quality of amplitude and phase at the image plane. Model 1 has a uniform phase profile with some variations in the amplitude profile, and model 2 demonstrates a constant amplitude with a more distributed phase profile. Intensity contrast optical images captured at the image plane of metasurfaces for models 1 and 2 (Shanei, et al., unpublished data).

Chapter 3

Optical forces and torques

3.1 Introduction

Light-matter interaction has been a subject of study for centuries. Kepler first proposed that the tails of comets are due to dust particles interacting with sunlight [86]. He even theorized that sunlight could exert pressure strong enough to push away the particles, which eventually became known as radiation pressure. Two centuries later, Maxwell created his theory of electromagnetism. He supplied a theoretical basis that demonstrated that light is an electromagnetic wave that can exert pressure on bodies [87, 88]. Maxwell's equations suggested that electromagnetic radiation could exert a force on matter and developed the mechanisms of light interacting with particles for centuries. This concept eventually paved the way for new investigations into light-induced forces [89].

In 1905, Einstein introduced the concept of photons as discrete packets of energy, or quanta of light, each possessing a defined momentum [90]. This was a significant advancement in understanding light as both a wave and a particle, in line with Max Planck's quantum theory. In 1923, this idea was experimentally verified by the physicist Compton who showed that photons were capable of transferring momentum to electrons, an unexpected behavior for classical waves. This experiment is now known as the Compton effect. This discovery provided direct evidence of photon momentum and further validated the quantum nature of light [91, 92].

These studies on the momentum exchange between light and matter developed further in the 20th century till the 1970s, when Ashkin did a series of studies in the optical trapping of a dielectric particle with a focused laser light. This technique, known as optical tweezers, represented a major advancement in the ability to control microscopic objects using light [93, 94]. Optical tweezers take advantage of the gradient and scattering forces existent in light to create a stable trapping potential at the focus point within an optical beam, allowing for precise manipulation without physical contact. Over time, the versatility of optical tweezers has been expanded, enabling the trapping and manipulation of a wide range of materials, including biological cells, metallic nanoparticles, and even single atoms [95, 96]. Their ability to exert finely controlled forces has made optical tweezers important in various fields, such as biology, chemistry, and nanotechnology. For instance, they have been used to study the mechanical properties of DNA, measure molecular interactions, and explore the behavior of quantum dots [97-100]. See [101-104] for other applications of optical manipulation of micro and nano objects in targeted drug delivery, precision surgery and nanostructure assembly. As scientists explore new ways to measure and control light, the discoveries from the past century still play a key role in shaping how we use light in science and technology today. [105].

The principle of optical tweezers is rooted in the study of optical forces and torques, which is important in the advancement of this technology and its applications in technology. These forces and torques, arising from the transfer of linear and angular momentum of light, form the foundation for the precise manipulation of microscopic and nanoscale particles. A comprehensive understanding of optical forces and torques is crucial for optimizing the design and functionality of optical tweezers. For instance, by analyzing how these forces behave under various conditions, researchers can enhance the stability and precision of optical trapping, enabling delicate and complex manipulations even in quantum systems. This chapter begins with an overview of the optical forces and torques that a beam of light can generate. It then explores how gratings can produce reaction forces and alignment torques. The final section delves into the dynamic interactions of microscale grating-based vehicles and rotors operating in a low Reynolds number regime.

3.2 Optical forces

The understanding of optical forces can be divided into different regimes based on the size of the particle relative to the wavelength of light. When particles are much larger than the wavelength of light, the geometrical optics approximation (ray optics regime) is applicable [106]. This approximation simplifies the calculations by treating the light as rays that are either refracted or reflected by the particle. Conversely, for particles much smaller than the wavelength, the Rayleigh regime (dipole approximation) is used, where the particle can be considered as a point dipole in the electromagnetic field [107]. These approximations are valuable physical insights due to offering quick solutions to complex problems. However, when the particle size is comparable to the wavelength, neither the geometrical optics approximation nor the dipole approximation suffices. Instead, full wave-optical modeling is required to accurately calculate the optical forces. This approach involves solving Maxwell's equations in their full form to capture the complex nature of scattering, absorption, and interference effects in this intermediate regime [108]. For example, for spherical and homogeneous particles, Mie's theory provides precise numerical results across various sizes and refractive indices. The complexity increases significantly with non-spherical or inhomogeneous particles, which are commonly encountered in optical trapping experiments [107]. Numerical methods such as the Maxwell stress tensor (MST) by using the finite-difference time-domain (FDTD) method or the discrete dipole approximation (DDA) are employed to predict optical forces and torques [12, 109-111]. These methods allow for the detailed modeling of light interaction with particles of arbitrary shapes and compositions.

3.2.1 Rayleigh regime

To calculate optical forces in the Rayleigh regime, which applies when the particle size is much smaller than the wavelength of the incident light, the dipole approximation is employed. This approximation treats the particle as an induced dipole in the electromagnetic field of light. In the Rayleigh regime, a small particle subjected to an electromagnetic field will see an induced dipole moment. The particle then experiences a Lorentz force in response to its induced polarization. A quasi-static calculation can be employed through the Lorentz force to calculate the optical force acting on a small spherical object in the Rayleigh regime. When the induced dipole moment in the object has a linear dependency on the monochromatic incident electric field, the induced dipole moment can be defined as $p(r) = \alpha(\omega)E(r_0)$ with polarizability of α related to the electric field at r. Then, the time-averaged force can be written as:

$$\langle \mathbf{F} \rangle = \frac{\alpha'}{2}\sum_i \mathrm{Re}\{\mathrm{E}_i^*\nabla\mathrm{E}_i\} + \frac{\alpha''}{2}\sum_i \mathrm{Im}\{\mathrm{E}_i^*\nabla\mathrm{E}_i\}, \tag{3.1}$$

where * is the complex conjugate sign. The first term is related to the inhomogeneous electric field and the real part of the polarizability. The second term is associated with a non-conservative force proportional to the imaginary part of polarizability, see [112] for more details. It was shown that by substituting the complex amplitude of the electric field with the real amplitude of E_0, the expression in Equation (3.5) can be simplified to

$$\langle \mathbf{F} \rangle = \frac{\alpha'}{4} \nabla E_0^2 + \frac{\alpha''}{2} E_0^2 \nabla \Phi, \tag{3.2}$$

where $\Phi(r)$ is the phase of the electric field. This equation reveals that the variation of the phase gradient inside the electric field can also generate optical forces. In this case, the phase gradient can redirect the scattering force along the axial direction to the transverse plane. This redirected component adds a complementary knob in the optical manipulation of the particles [113].

3.2.2 Ray optics

When a laser beam is directed at a large object in comparison to the wavelength of the light, the interactions between the light and the object can be studied using the principles of ray optics. This approach simplifies the calculation of optical forces by treating the light as a collection of rays, each interacting with the object individually. Hence, in this model, the optical forces exerted on the object are determined by examining how each light ray is altered upon striking the object. When a light ray enters the object, it may be refracted according to Snell's Law, which describes how light bends as it passes from one medium to another based on the refractive indices of the two media. The initial momentum of a light ray is directly proportional to its Poynting vector, which represents the direction and magnitude of the energy flow of the electromagnetic field. As the light ray enters and exits the object, refraction changes its direction, and thus its momentum. This change in momentum is critical because, according to the conservation of momentum, any changes in the ray's momentum result in an equal and opposite reaction force on the object. By calculating the momentum change for each ray, the total optical force can be calculated by summing the momentum changes of all the rays interacting with the object and dividing by the time interval over which these changes occur.

This summation gives the net force exerted by the light on the object, which can result in pushing, pulling, or even rotating the object, depending on the distribution of the refracted rays.

3.2.3 Optical forces induced by a focused beam

Early studies on optical trapping focused on the radiation pressure of light, where force is exerted along the direction of light propagation. Optical confinement, however, relies on forces arising from variations in light intensity. This section explains these forces, which are fundamental to the operation of optical tweezers.

Figure 3.1 (a) shows a Gaussian light with two beam rays transmitted toward a particle located off-axis of the beam. As shown with arrows, the scattered rays propagate at different angles because of the refraction of the light rays. Hence, the scattered light acquires a different momentum than the incident light. Based on the conservation law of momentum, the driving force (F_a) is exerted on the particle to compensate for the changes of momentum during the scattering process. The other ray would also exert the optical force (F_b). Due to the Gaussian distribution of the incident beam, the optical force F_a is stronger than F_b, which moves the particle toward the center of the beam. Additionally, scattered rays create a force along the light beam's propagation direction, as shown in Figure 3.1 (c). Together, these forces enable precise control and manipulation of particles, forming the foundation of optical trapping technology.

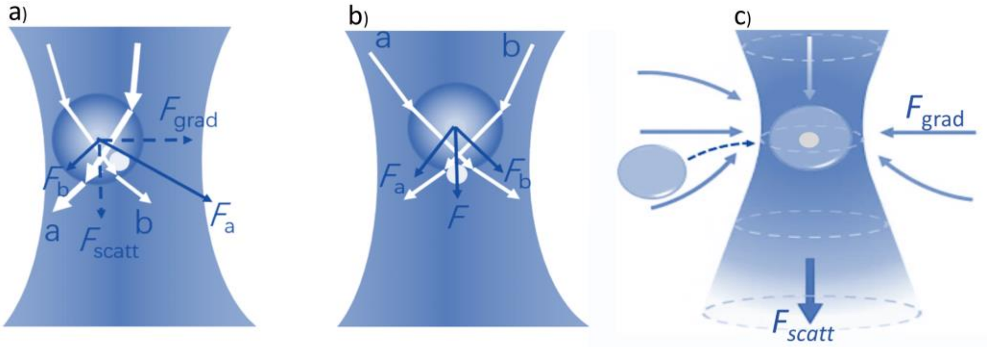

Figure 3.1: Schematic illustration of conventional optical tweezers for three-dimensional confinement of a particle. (a) Particle is located away from the focal point or center of a Gaussian beam and moved toward higher intensities at the center. (b) Particle is pushed to the center of the focal point, and (c) 3D-confinement of a particle at the center of a tightly focused beam.

In summary, the optical forces in a focused light beam can be divided into scattering and gradient forces. Scattering forces are common optical forces that can be observed when an incident plane wave impinges on a particle. In contrast, the gradient force arises from the non-uniform intensity distribution of the light beam. The gradient force is noticeable in tightly focused beams. In the case of a modestly focused beam, the intensity gradient can trap a particle in the transverse plane, while the scattering force pushes the particle along the propagation direction against a nearby interface. This two-dimensional trapping method is useful for manipulating absorptive plasmonic nanoparticles, for example.

3.2.4 Optical forces acting on a grating

When light interacts with a periodic structure with periodicity close to the wavelength of light like a grating, the interaction leads to the wavefront manipulation of incident light through diffraction. To understand the optical forces generated in such a system, consider a two-dimensional grating aligned in the coordinate system (x', y', z') with periodicity d along x'. The diffraction angle $\theta = \arcsin\left(\frac{\lambda_0}{dn}\right)$ is set by d, the vacuum wavelength λ_0, and the refractive index of the surrounding medium n.

In the case of a blazed grating or a metagrating, the strongest diffraction typically occurs in a specific direction, for instance, it is the +x' direction in this setup. As illustrated in Figure 3.2, the diffraction angle is measured from the z′-axis and is positive for the +1-diffraction order. In this picture, when a Gaussian beam, with dimensions larger than the grating, strikes it, various optical forces and torques can be created through light-grating interactions [114-116]. This section focuses on optical forces, while optical torques are explored in the subsequent section.

Radiation pressure force

Radiation pressure force acts along the direction of propagation (z'-axis) and arises from the momentum of photons that are scattered or absorbed. It becomes significant when a considerable fraction of the incident light is absorbed or reflected by the grating rather than diffracted at large angles.

Gradient force

The gradient force originates from non-uniform light intensity distributions, such as those in Gaussian beams. This force pulls the grating toward regions of higher light intensity, analogous to the trapping forces observed in section 3.1.3.

Reaction force in lateral direction

The reaction force results from the redirection of light by the grating. As the light diffracts at specific angles determined by the grating's periodicity, the change in the momentum of the incident photons generates a force on the grating. Due to the conservation of linear momentum, this force acts in the opposite direction to the net momentum of the diffracted light. For a grating, this often means the reaction force is directed opposite to the strongest diffraction direction [59, 117-119]. Figure 3.2 schematically illustrates a metagrating with three diffraction orders in transmission and reflection.

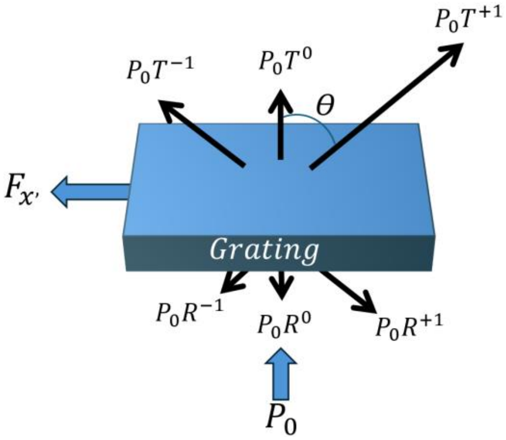

Figure 3.2: Optical lateral reaction force on a metagrating.

To study the reaction forces in a plane of grating, consider the incident power P_0 is given by the incident irradiance I_0 times the grating area A as $P_0 = I_0A$. The irradiance is in turn given by the time-averaged energy density $\langle w \rangle$, as $I_0 = c\langle w \rangle = \frac{\epsilon_0 c}{2} E_0^2$, where E_0 is the amplitude of the incident electric field.

The linear momentum p carried by a beam with power P per time unit is

$$\frac{\partial p}{\partial t} = \frac{P}{\hbar\omega}\hbar k = n\frac{P}{c_0} \tag{3.3}$$

where n is the refractive index of the surrounding medium, c_0 is the speed of light in a vacuum, k is the magnitude of the wave vector and ω is the angular frequency. Note that the photon momentum used here is according to Minkowski, not Abraham. The response of grating to P_0 is the diffraction of light into different orders i in transmission and reflection modes at diffraction angles θ_i.

For example, by projecting the diffracted momenta on the x′-axis, through multiplication with $\sin(\theta_i)$ and correcting for the change in wave-front area from the incident to the diffracted beams through multiplication with $|\cos(\theta_i)|$, the net reaction force in the lateral direction (x′-direction) can be obtained by summing over all diffraction orders and taking the negative. Additionally, to account for absorption, the absorbed power must be subtracted from the total power contributing to the lateral reaction force, as absorption contributes only to radiation pressure in the z′-direction. See the supplementary materials in **Paper II** for details.

3.3 Optical torques

Photons in an elliptically polarized light beam possess both intrinsic linear momentum and spin angular momentum (SAM). Linear momentum is related to the photon's energy and as discussed in previous sections, is dependent on the frequency of the light. In contrast, SAM, which is associated with the polarization state of the light, remains constant regardless of frequency. In addition to SAM, light can also carry orbital angular momentum (OAM), a form of momentum that arises from the spatial structure of the light beam rather than its polarization. OAM usually exists in beams with a helical phase front, such as Laguerre–Gaussian beams, where the phase of the light wavefront twists around the beam axis. This twisting imparts an additional angular momentum to the beam, which can be transferred to particles or objects, leading to rotational motion. The study of OAM has opened new avenues in optical manipulation, enabling the control of rotation and orientation at microscopic scales [120-123].

A key property of OAM is that the amount of angular momentum per photon is directly proportional to the beam's topological charge, which makes OAM a tunable and distinct characteristic of light. This property can be utilized in advanced optical trapping and rotational control applications [124, 125].

Although linearly polarized light does not intrinsically carry SAM, it can still induce an optical *alignment torque* on an object. This happens because the linear polarization state of the light can be modified upon scattering, leading to a change in the ellipticity of the incident light. As the light scatters, this changes in the polarization state means that the angular momentum of the scattered light differs from that of the incident light. According to the conservation of angular momentum, this difference results in a transfer of optical torque to the object, causing it to rotate. The ability to induce torque using linearly polarized light has been explored in various contexts, including the alignment of non-spherical particles, where the shape anisotropy of the particle plays a significant role in the interaction with the incident light [126]. The next section explores spin transport as light passes through an object, followed by an analysis of optical alignment torque in the context of a grating.

3.3.1 Optical torques generated by a laser beam

The mechanical observation of light-induced optical torques by leveraging an angular momentum of a beam was first demonstrated experimentally by Beth [127]. Later, researchers separately investigated mechanical motion induced by SAM or OAM [120, 121, 128]. The SAM can rotate the object around its axes based on the polarization of the incident beam. The OAM provides orbital rotation around the axes of the impinging light, such as a Laguerre–Gaussian beam carries OAM given by $\ell\hbar$ per photon where ℓ can be any integer [129]. Figure 3.3 shows a schematic of the spinning and orbiting of a particle for a circularly polarized and helical beam on the left and right sides.

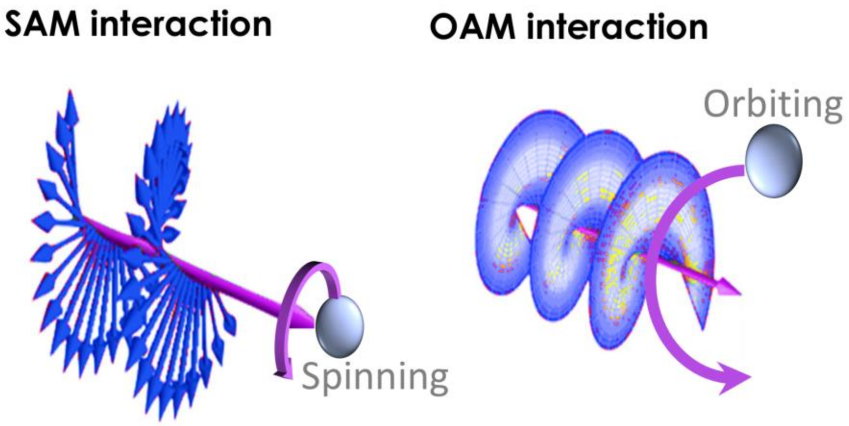

Figure 3.3: Schematic illustration of the spinning and orbiting of a particle through the polarization state of the light (SAM) and a structured vortex beam (OAM), respectively.

To calculate the spin transport from light through an object we can define the time-averaged spin density as:

$$\langle \mathrm{s} \rangle = \mathrm{Im}\,[\epsilon_0 \mathrm{E}^* \times \mathrm{E} + \mu_0 \mathrm{H}^* \times \mathrm{H}]/4\omega, \tag{3.4}$$

where E is the incident field in the x-y plane in a very general form of

$$\mathrm{E} = E_0 Re\left\{\begin{pmatrix} \sqrt{(1+Q)/2} \\ \sqrt{(1-Q)/2e^{i\emptyset}} \end{pmatrix} e^{i(kz-\omega t)}\right\}, -1 < Q < 1, 0 < \emptyset < 2\pi. \tag{3.5}$$

Considering Equations (3.8) and (3.9), $\mathrm{E} = \mathrm{E}_0$ and $\mathrm{H} = \frac{1}{\mu_0 c}\hat{\mathrm{z}} \times \mathrm{E}_0$ we have:

$$\langle \mathrm{s} \rangle = \mathrm{Im}\,[\epsilon_0 \mathrm{E}_0^* \times \mathrm{E}_0]/2\omega = \frac{\epsilon_0 E_0^2}{2\omega}\sqrt{(1+Q)(1-Q)}\sin{(\emptyset)}\hat{z} \tag{3.6}$$

For $Q = 0$ (circular pol), we then have that $\langle s \rangle = \pm\hbar$ number of photons per volume unit, with + for left handed circularly polarized (LCP) light ($\emptyset = \pi/2$) and for right handed circularly polarized (RCP) light ($\emptyset = 3\pi/2$).

Finally, in analogy with energy transport through a surface with a cross-section area A perpendicular to the propagation direction, the spin transport through that surface equals:

$$c\langle s\rangle A = \frac{IA}{\omega}\sqrt{(1+Q)(1-Q)}\sin(\emptyset), \tag{3.7}$$

where $IA = P$ is the power that hits the surface.

3.3.2 Alignment torque

When an object is excited by a beam of light, due to the conservation of angular momentum, the object experiences an optical torque equal to the difference between the incoming and outgoing spin angular momentum. By implementing the same principle, the grating shown in Figure 3.4 experiences a torque τ_A that compensates for the change in scattered spin:

$$c\langle \mathrm{s}_0\rangle A = c\langle \mathrm{s}_s\rangle A + \tau_A, \tag{3.8}$$

where $\langle \mathrm{s}_0\rangle$ and $\langle \mathrm{s}_\mathrm{s}\rangle$ the time-averaged spin density for the incident and scattered light. In the particular case of two-dimensional grating, where the beam is diffracted at an angle θ, each diffraction order will be characterized by a specific field transmission/reflection tensor. The field coefficients are then complex 2×2 diagonal tensors if we consider the field along x generates p-polarized while the field along y generates s-polarized diffraction. Therefore, an incident field polarized along x or y will keep its polarization after transmission/reflection. The i^{th} transmission or reflection tensor can then be written like this:

$$\mathrm{t}_i, \mathrm{r}_i = \begin{pmatrix} \mathrm{p}_i & 0 \\ 0 & s_i e^{i\psi_i} \end{pmatrix} \tag{3.9}$$

where p_i and s_i are real numbers (amplitudes) and ψ_i is the relative phase shift between the i^{th} s and p-polarized components imposed by the grating as shown in Figure 3.4.

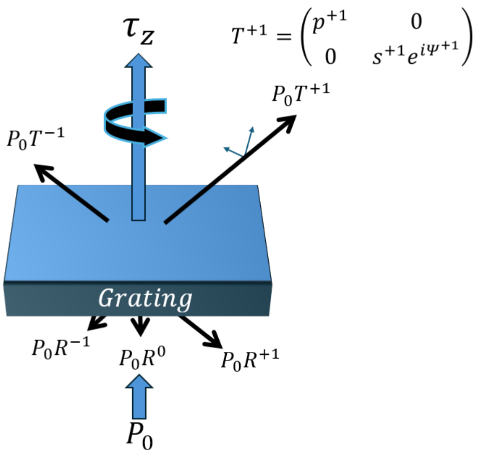

Figure 3.4: Optical alignment torque on a grating.

The grating deflects the main part of the beam at an angle θ by the surface of A. Since the spin torque vector of the bent wave is parallel to its propagation direction, we need to project it on the z-axis to apply the angular momentum conservation rule. The $\hat{z}$-component of the torque can by following the same procedure for the linear momentum transfer and forces in the xy-plane:

$$\tau_{\hat{z}} = cA\langle s_0\rangle - cA\sum_i \langle s^i\rangle \cos(\theta_i)\,|\cos(\theta_i)|, \qquad (3.10)$$

where the first $\cos(\theta_i)$ factors project out the actual $\hat{z}$-components of the diffracted torque and the second one is for correcting for the change in diffracted wave-front area. In xy-plane the spin density of a plane wave is directed parallel to the propagation direction and is $\langle \mathrm{s}^{\mathrm{t}_i}\rangle = \mathrm{Im}\left[\epsilon_0 E^{t_i^*} \times E^{t_i}\right]/2\omega$ for transmission. By writing out the full expression for the torque in terms of power, and using p_i and s_i for the p-and s-polarized diffraction coefficients, for x-polarized incidence the optical torque can be written as:

$$\tau_{\hat{z}} = -\frac{1}{\omega}(P_0 - P_{abs})\sin(2\varphi)\sum_i \left[p_i s_i \sin(\psi_i)\cos(\theta_i)\,|\cos(\theta_i)|\right] \qquad (3.11)$$

In the case of linear polarization, the alignment torque strives to orient the grating parallel to the incident polarization due to the $\sin(2\varphi)$ factor. The magnitude of the alignment torque is the maximum for $\varphi = \pm 45°$ and $\pm 135°$ and it vanishes when the grating is either aligned with or perpendicular to the polarization.

Finally, it's important to note that the alignment torque becomes zero when $\psi_i = 0$, meaning there is no phase difference between the transmitted or reflected fields that are polarized parallel and perpendicular to the grating lines. This outcome is expected since, in the absence of a phase difference, the transmitted and reflected fields remain linearly polarized, resulting in no spin angular momentum. Interestingly, to generate an alignment torque that tends to orient the grating, the sin (ψ_i) must be negative for transmission and positive for reflection to obtain an alignment torque that strives to orient the grating.

For circularly polarized lights such as LCP the total torque is:

$$\tau_{\hat{z}} = -\frac{1}{\omega}\left\{P_0 - (P_0 - P_{abs})\sum_i \left[p_i s_i \cos(\psi_i)\cos(\theta_i)|\cos(\theta_i)|\right]\right\} \tag{3.12}$$

Here, the total torque has two parts, the intrinsic spin torque and alignment torques. The spin torque obtained for LCP incidence is, in contrast, independent of grating orientation. If all diffraction is parallel to the plane of the grating, the torque is given by the incident spin. In other cases, diffraction adds or subtracts torque depending on the different phase factors. These appear as cos (ψ) in contrast to the alignment torque case. To summarize this part, Figure 3.5 shows the result of Maxwell stress tensor (MST) simulations for optical forces and torque as a function rotation angle. It can be seen that the maxima and minima in spectra follow the same trend as discussed in Equations. (3.6) and (3.16) for optical forces and torques.

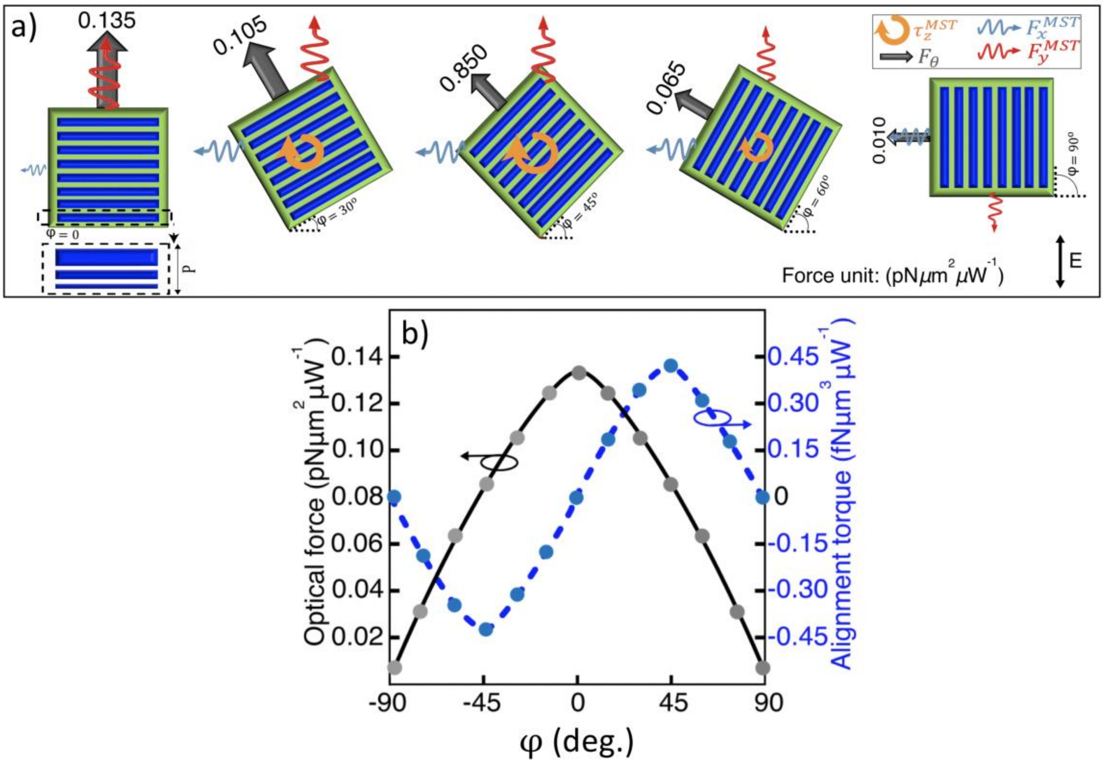

Figure 3.5, MST simulation of optical forces and alignment torques: (a) Direction of reaction force and alignment torque on gratings, normalized to the incident light intensity. (b) Optical force and torque as a function of the orientation angle of gratings.

3.4 Dynamics and interactions of rotors

The concept of the low Reynolds number, elaborated by physicist E.M. Purcell in 1976, considers the unique conditions under which small organisms operate in fluid environments where viscous forces dominate over inertial forces [14]. The Reynolds number is a dimensionless quantity used to predict flow patterns in different fluid flow situations, calculated as $Re = \rho v L/\eta$, where ρ is the fluid density, v is the velocity, L is a characteristic length, and η is the fluid dynamic viscosity. At low Reynolds numbers ($Re \ll 1$), the dominance of viscous forces results in a range of phenomena impacting the behavior of microorganisms. For example, the fluid flow at a low Reynolds number is smooth and orderly, known as laminar flow, without turbulence.

Operating optical actuations to drive micro and nano-scale rotors at low Reynolds numbers poses significant challenges due to the dominance of viscous drag. In this regime, when the rotor is much thinner than it is wide, the drag torque scales with the cube of the rotor's radius r. For example, for a rotating disk, the rotation drag coefficient is $\gamma_r = \frac{32}{3}\eta r^3$ [130, 131]. In the attached **Paper III**, the feasibility of driving grating-based rotors with diameters up to 100 µm is demonstrated, along with detailed analyses of their drag coefficient as a function of radius. In addition to the challenges of driving objects at low Reynolds numbers, understanding the interactions between rotors is essential for the development of microscale devices and synthetic nanoscale machines. Two primary interactions between rotors are identified: 1) Conventional interaction known as hydrodynamic coupling [132, 133]. 2) An unconventional interaction driven by transverse gradient forces between rotors.

In this section, a brief overview of hydrodynamic coupling will be presented, detailing how the interaction between spinning rotors occurs in a fluid environment. This coupling is fundamental in microscale systems, where the motion of one rotor can induce fluid flow that influences the behavior of nearby rotors. Following this, this section introduces the unconventional interaction observed between grating-based rotors, which is driven by transverse gradient forces. Unlike hydrodynamic coupling, this interaction is rooted in the optical forces generated by the structured light fields interacting with the gratings. This novel mechanism can offer new possibilities for manipulating rotors at the micro- and nanoscale, useful in active artificial matter systems, and the precise control of rotational dynamics in advanced micro- and nanomachinery.

3.4.1 Hydrodynamic coupling

Hydrodynamic coupling is a fundamental concept in fluid dynamics, particularly relevant when multiple rotors or objects interact through the fluid that surrounds them [134-137]. This coupling occurs when the motion of one spinning object influences the fluid flow, thereby affecting the behavior of nearby passive or active objects. To illustrate a simple example, Figure 3.6 (a) shows a single sphere spinning around its center without translating. The flow field generated by such a sphere displays rotational symmetry, as shown in the CFD simulation of Figure 3.6 (a). If an object, such as the cylinder shown in Figure 3.6 (b), is positioned near the sphere, it will experience stress within this flow field. This stress, which also affects the rotor itself, is influenced by several factors, such as the angular velocity of the spinning rotor and its radius. These variables are crucial in determining the fluid’s response. Figure 3.6 (c) illustrates the normalized shear stress on the cylinder, calculated by integrating over its surface.

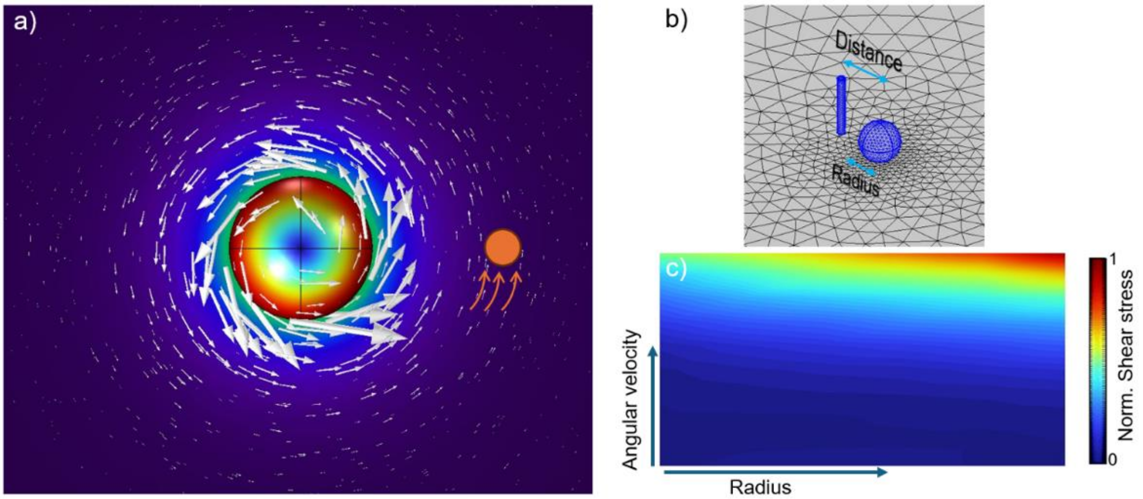

Figure 3.6: (a) CFD simulation of fluidic flow created by a spinning sphere. (b) An object close to the sphere and (c) the total stress on the object as a function of the radius and angular velocity of the sphere.

Rotors spinning in the same direction, orbital motion:

Now, if the object is replaced by another rotating sphere, the flow generated by one rotor induces a velocity at the location of the second rotor. If the rotors rotate in the same direction, the induced velocities are such that each rotor experiences a tangential force due to the other rotor's flow field. These tangential forces do not cancel out but instead create a torque that causes each rotor to move in a circular path around the other. The result is an orbital motion where the two rotors rotate around their common center of mass [138]. The balance of forces and torques from the interacting flow fields leads to a stable orbital motion, as long as the rotors maintain their relative positions and rotational speeds.

Rotors spinning in opposite directions, locomotion:

When two rotors spin in opposite directions, their rotational flow fields also oppose each other, creating a net force in the same direction. As a result, the rotors translate together as a pair instead of rotating around each other, functioning like a microscale swimmer with locomotion. The direction of the translational motion can be controlled by adjusting the torques on the rotors. By changing the relative strengths and directions of the torques, the direction of movement can be reversed or steered, providing a mechanism for controlled locomotion [139, 140].

3.4.2 Interaction between grating-based rotors

The dynamic interaction between rotating rotors submersed in fluid has been the subject of intensive research directed at providing fundamental insights into the interplay between different microscale forces. All previous studies have found that when two untethered but interacting rotors spin in the same direction, the result is an orbital motion in the same direction as the spinning motion. But, when two or more grating-based rotors are trapped together in a laser beam, they collectively orbit in the opposite direction to their spinning motion, which contrasts with rotors coupled through hydrodynamic or mechanical interactions, as shown in Figures 3.7 (a) and (b). This anomalous behavior originates in a transverse optical gradient force that dominates hydrodynamic and mechanical interactions. To understand the anomalous orbital motion of rotors in a loosely focused light, it is essential to study the optical forces acting upon them.

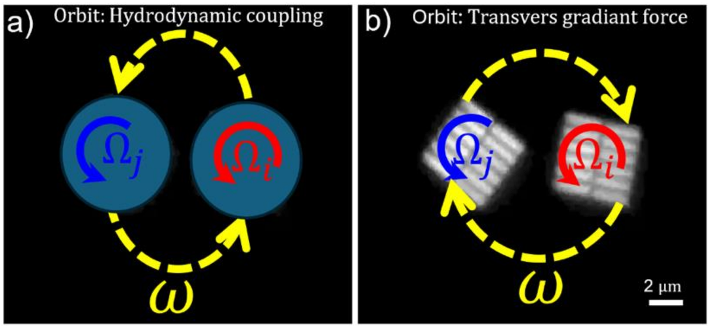

Figure 3.7, Differences between the interaction in submerged micro-scale rotors and grating-based rotors: (a) Hydrodynamic coupling between two exemplary conventional rotors with counterclockwise (CCW) spinning and orbiting and (b) two grating-based rotors with CCW spinning and CW orbiting.

In systems of grating-based rotors each rotor features a pair of gratings that deflect light in opposite directions, enabling the particles to rotate even under loosely focused illumination

(Paper II). Moreover, due to Gaussian intensity, there is a classical optical gradient force, F_{grad} which acts to pull a rotor towards the center of the beam as it is spinning around its axis. As it reaches the center of the beam, stable spinning without translation can be observed since the vectorial sum of the two reaction forces F_1 and F_2 on the rotor's center of mass equals zero, as depicted in Figure 3.8 (a). In a different setup, as illustrated in Figure 3.8 (b), a pillar obstructs the center of the beam. In this situation, the rotor section closer to the center receives more photons, leading to an uneven distribution of forces. This results in a net force acting on the rotor's center of mass. So, the rotor experiences two distinct force components: the transverse gradient force, which is always directed perpendicular to the conventional intensity gradient force, and another component that varies with the rotor's orientation but does not lead to a net displacement of its center of mass. Consequently, the rotor orbits around the pillar while spinning around its axis. In the third scenario, shown in Figure 3.8 (c), two identical rotors are placed within a Gaussian beam. Since they cannot both occupy the exact center of the beam, they position themselves symmetrically with their edges near the center. This arrangement results in unbalanced reaction forces and introduces a net transverse gradient force acting on each rotor's center of mass. An example of this behavior is illustrated in Figure 4.11. For more details on the derivation of the transverse gradient optical force, refer to the supplementary note in **Paper II**.

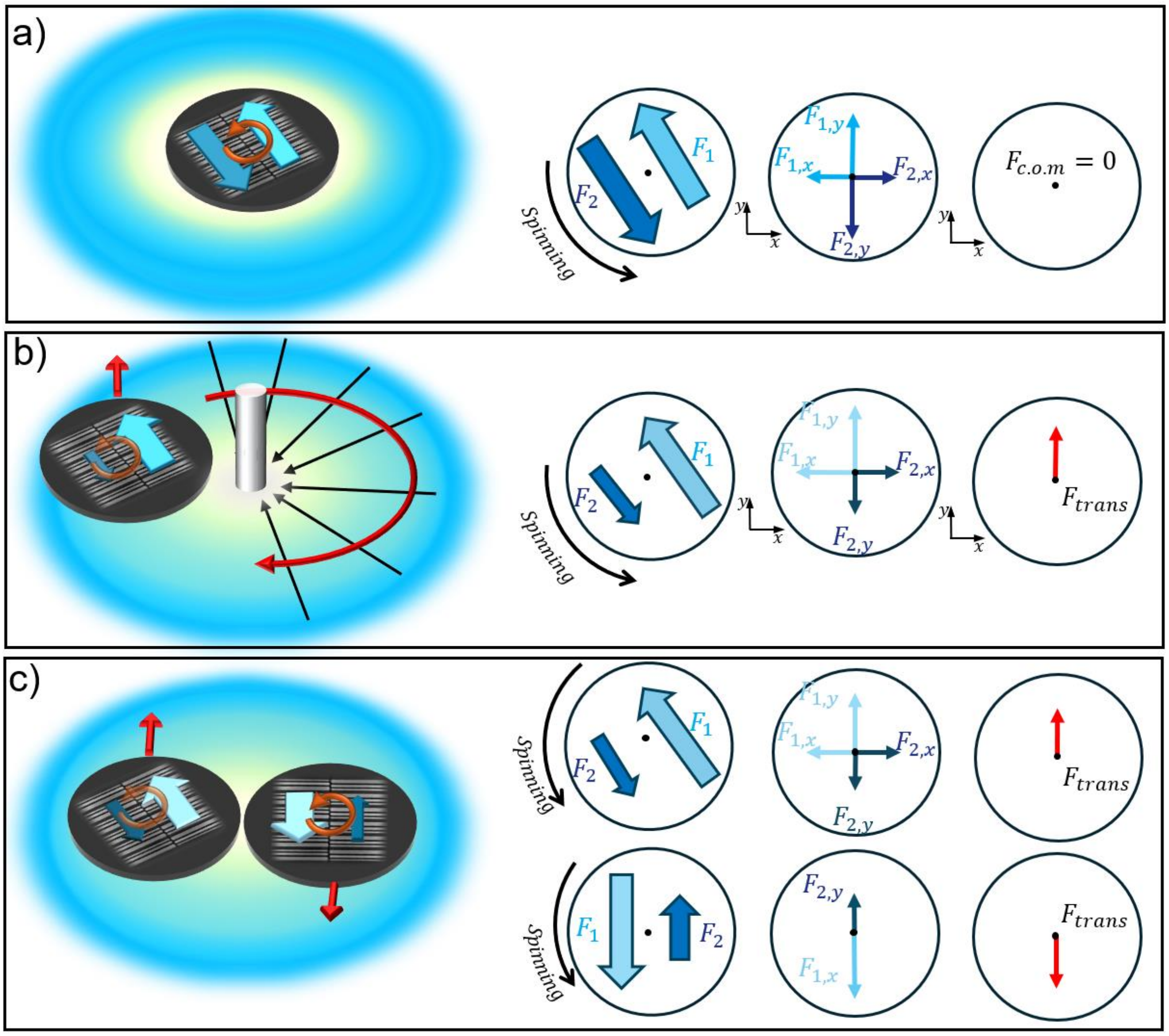

Figure 3.8, Transverse gradient force: (a) A spinning rotor at the center of a Gaussian beam, exhibiting stability due to the intensity gradient force. (b) A rotor positioned off-center within the beam experiences a transverse gradient force (red arrow) that acts perpendicular to the intensity gradient force (black arrows). (c) Two identical rotors are positioned symmetrically around the beam center, generating transverse gradient forces that cause them to orbit in a direction opposite to their spinning motion.

Chapter 4

Optical manipulation through metasurfaces

This chapter explores various actuation mechanisms for manipulating micro- and nano-objects, emphasizing the use of optical fields as external excitation sources. These mechanisms are divided into two main categories: light-assisted manipulation and direct optical manipulation. Light-assisted manipulation encompasses actuation mechanisms such as photochemical, photothermal, photomechanical, and optoelectronic light-triggered biohybrid, while direct optical manipulation relies solely on light-matter momentum interactions, without involving any secondary processes.

The chapter proceeds with detailed examples of direct optical manipulation assisted by metasurfaces. The first section highlights the transport of small beads using light beams shaped by cylindrical metalens, as demonstrated in (**Paper I**). Additional examples of particle manipulation using metasurfaces are available in Review [82, 84], where the metasurface functions as a passive structure, shaping the wavefront of incoming light to achieve precise control. The second section shifts focus to the manipulation of microscale objects integrated with metasurfaces, as described in (**Papers II** and **III**). In this case, the embedded metasurfaces not only alter the momentum of the incident light but also experience forces themselves, enabling the objects to function as metarotors and metavehicles. Furthermore, hydrodynamic particle manipulations driven by the metarotors are demonstrated, showcasing the dynamic capabilities of such systems. The chapter concludes with another application of active metasurfaces, demonstrated through the functionality of a movable lens system.

4.1 Field-driven manipulation

The essential part of manipulating a particle is the actuation energy source that controls the performance of the manipulation mechanism. Although self-driven micro-objects can receive their required triggering energy from the environment, an external source is often required to provide a user-controlled or automated manipulation of objects [141]. The spatial position of an object can be manipulated by various energy sources, including bio-hybrid actuation, electrical field, acoustic wave, light radiation, and magnetic field, depending on the material and its surrounding environment. In addition, multi-source excitations have been utilized with more degrees of freedom to govern an accurate, stable, and flexible actuation. Figure 4.1 illustrates various types of particle manipulations based on actuation mechanisms. See reviews [141-145] for more details.

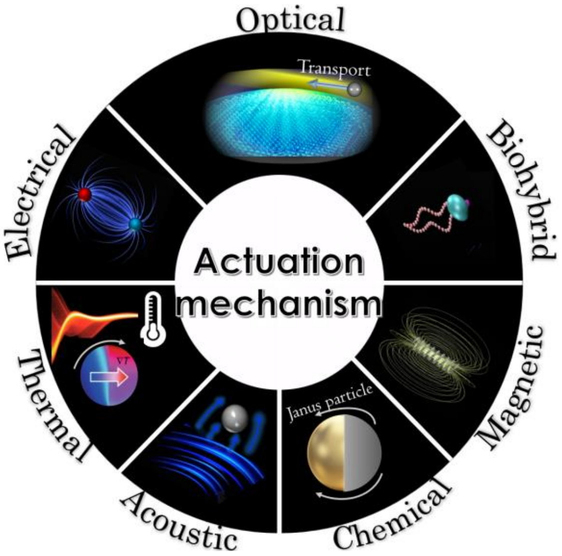

Figure 4.1, Various types of actuation mechanisms to manipulate micro and nano-objects. Biohybrid sources are the most biocompatible energy source activated by the conjugation of living entities as cargo to the target objects. However, while this source is suitable for swarm control of objects, its application is limited due to the low accuracy [146-149]. Magnetic field is a useful actuator for medical applications that can easily penetrate the tissue. This kind of actuator provides the possibilities for transporting, tumbling, spinning, and morphing the shape of a magnetic structure. However, using a magnetic field as a driving force presents some practical challenges, such as complex large hardware equipment, difficulties in film coating, and other treatments of the substrate, particularly nano-scale manipulation [150-152]. Chemical actuators are a popular research area extensively studied to control single or even swarms of micro-objects. This type of actuation may overlap with biohybrid mechanisms where living entities are used to activate a chemical reaction. In one of the first experiments of chemically driven particles, high concentrations of toxic hydrogen peroxide were used to activate a series of reactions [153, 154]. Other types of sources such as electrical [155], thermal [156] and acoustic fields [157, 158]

are less applicable in comparison with the other introduced actuators due to low accuracy, resolution and depth of penetration.

Figure 4.2 shows the growing number of publications on manipulating and controlling micro- and nano-scale objects using the terms microswimmer or micro and nanorobot. It is important to note that current literature refers to micro- and nano-objects with various terms, including robot, motor, rotor, swimmer, and vehicle.

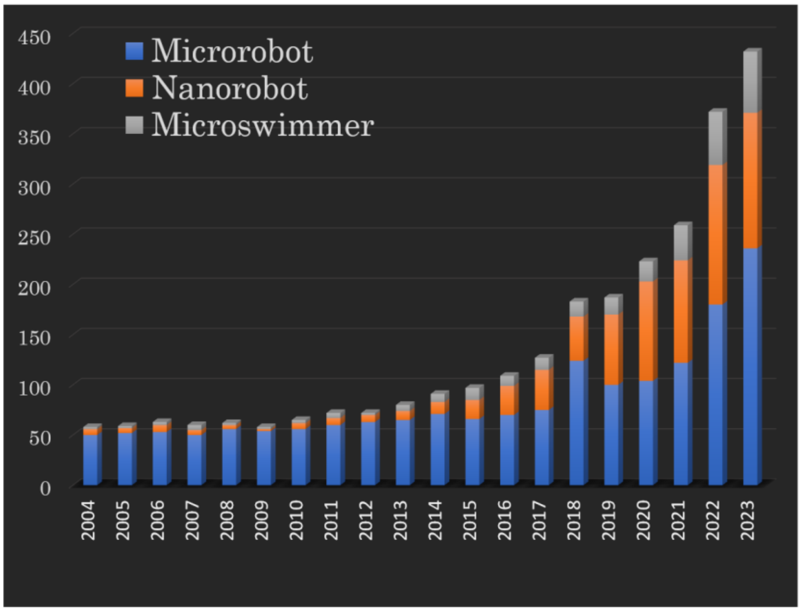

Figure 4.2: Number of publications containing the terms microrobot, nanorobot and micro-swimmer. The data is extracted from the web of science (WOS) from 2004 to 2023.

Among various actuation mechanisms, light stands out as an important energy source due to its high level of control over particle manipulation. It enables rapid, precise, and tunable real-time manipulation of objects [159].

As previously discussed, light-powered manipulation can be categorized into two main groups based on the driving mechanisms: indirect (light-assisted) and direct. In light-assisted actuation, light serves as a primary energy source that triggers a secondary mechanism to control the swimmer. This category encompasses various techniques, each defined by its specific actuation mechanism. Below, I briefly introduce some of the most prominent and widely used light-assisted methods for manipulating objects.

- Photochemical manipulations: Photochemical actuators convert optical energy into kinetic energy through chemical reactions. These reactions are initiated by the absorption of optical waves using two main mechanisms: photochromic and photocatalytic effects. For example, Janus particles and elongated structures, such as rod-shaped particles can be manipulated using this method. To control these objects, an unbalanced gradient on opposite sides of the structure is required. This gradient can either arise from the different composition of materials or uneven reactions inside the core and surrounding body [142].

- Photothermal manipulations: Photothermal manipulation relies on absorbing materials to convert optical energy into a thermal distribution around the target object [156, 160]. The diffused heat usually decays in the outward direction, forming a gradual temperature gradient that provides the required energy for propulsion. On the other hand, it is also possible to accumulate particles by thermocapillary flows that stream toward the structures. Another example of photothermal manipulation is based on constructing an intermediary agent, such as a bubble at the interface, to transport objects [161]. In this technique, a programmable and tunable temperature gradient can be induced by engineering the spatial positions of lossy structures and using birefringence elements, respectively.
- Photomechanical manipulations: Photomechanical actuation mechanisms depend on the interactions between light and/or mechanically photo-responsive materials such as liquid crystals [162], hydrogels [163] and shape memory polymers [164]. The structural shape of these materials relies on the alignment of the molecular phases. For example, a liquid crystal can switch the orientation of its molecular phase from order to disorder when excited by an external optical field. This transition can modify the spacing between the molecules, which forms a mechanical motion for soft material. More details have been reviewed in [165].
- Optoelectronic manipulations: Optoelectronic-based tweezers are the most tunable and user-friendly approach among the introduced optically assisted manipulation. This technique was invented in 2005 by Chiou and his group [166]. Then, it attracted attention due to its high efficiency and reliable manipulation of objects. Usually, the required structured light in this system is an LED equipped with a digital micromirror device (DMD). The impinging light can locally modulate the impedance of a photoconductive substrate, such as hydrogenated amorphous silicon, to induce a varying electric field over the surface. This non-uniform field generates dielectrophoresis (DEP) forces in the scale of nano-newtons which control the position of the target object even with a size larger than 100 micrometers [167]. Various examples of the technique have been studied in the recently published papers of [168, 169].

- Light-controlled biohybrid manipulation: Light-controlled biohybrid structures combine biological components, such as cells or biomolecules, with engineered structures to create versatile and responsive microscale systems. By utilizing light as a stimulus, these structures can move, perform targeted tasks, or interact with their environment. For example, bacteria-powered microbots can be integrated with light-responsive elements, allowing the direction and speed of bacterial propulsion to be regulated by light [149, 170].

In contrast, direct optical manipulation relies solely on momentum exchange during light-matter interactions, without involving any secondary processes. This approach provides precise and highly flexible control over micro-objects, garnering significant interest from the bioscience community [97, 171-173].

4.2 Optical manipulation by stationary metasurfaces

Two examples of trapping with the cylindrical and spherical metalens are shown in Figure 4.3 for two and three-dimensional trapping of 2 µm polystyrene (PS) beads, respectively. These metalenses are defined by a PB phase approach that has been used to realize the target phase of Equation (2.7) with a-Si metaatom as building block with a refractive index of 3.8 located on the top of the glass.

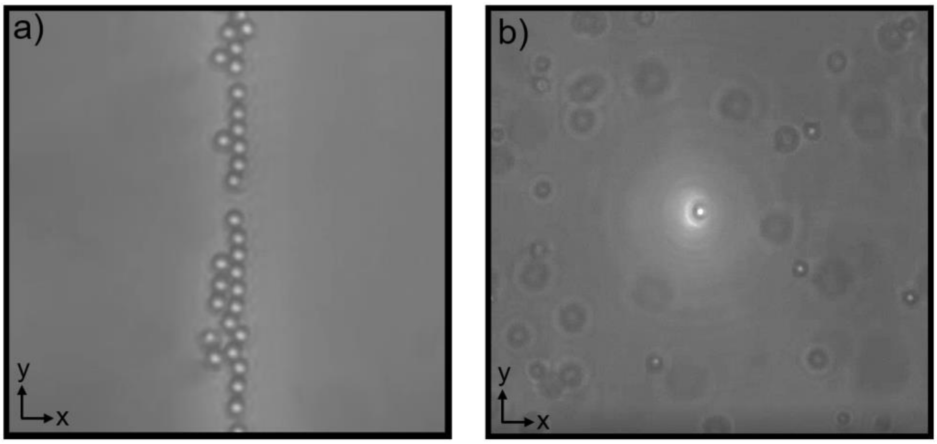

Figure 4.3: Optical trapping of 2 µm polystyrene (PS) beads. Two and three-dimensional trapping using cylindrical and spherical metalens in the left and right boxes. The metasurfaces were excited by a left-handed circularly polarized light at 1064 nm with the intensity of 5.5 and 3 $\mu W \cdot \mu m^{-2}$ for the cylindrical and spherical lenses, respectively.

In Figure 4.3 (a), introducing a phase gradient profile in the y-direction, such as $\varphi(y)$ from Equation 2.8 enables the direct printing of a linear phase gradient along the focal line of the metalens. This phase gradient redirects a part of the scattering force from the axial direction into the transverse plane, resulting in phase-dependent optical forces. These forces can transport trapped particles, as detailed in **Paper I** and illustrated in the snapshots presented in Figure 4.4.

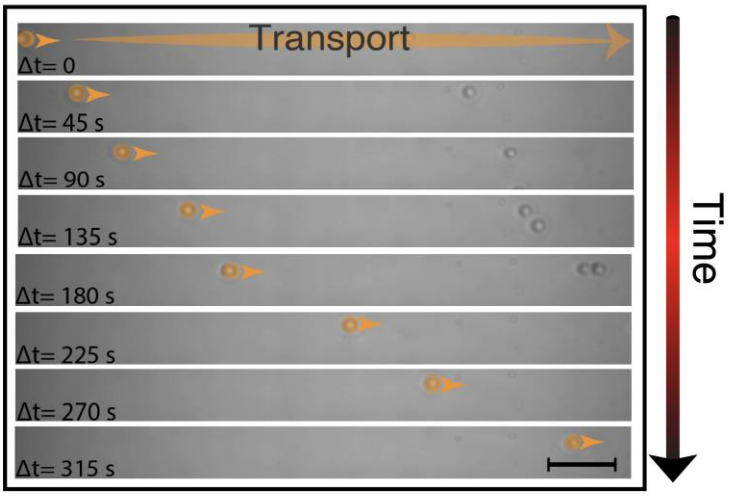

Figure 4.4: Transport of particles by passive metasurface. Snapshots of track of a labeled particle as propelled within the line trap with the average speed of v = 2.5 μm/s for I = 4 $\mu W \cdot \mu m^{-2}$ left-handed circularly polarized light at 1064 nm.

Due to the printed phase gradient, a transverse displacement occurred in the focal line, as shown in the simulation results of Figure 4.5. It can be observed that as the phase gradient rate increases, the line also moves toward the metasurface. The displacements cause a reduction in the efficiency of metalens at the target trapping plane.

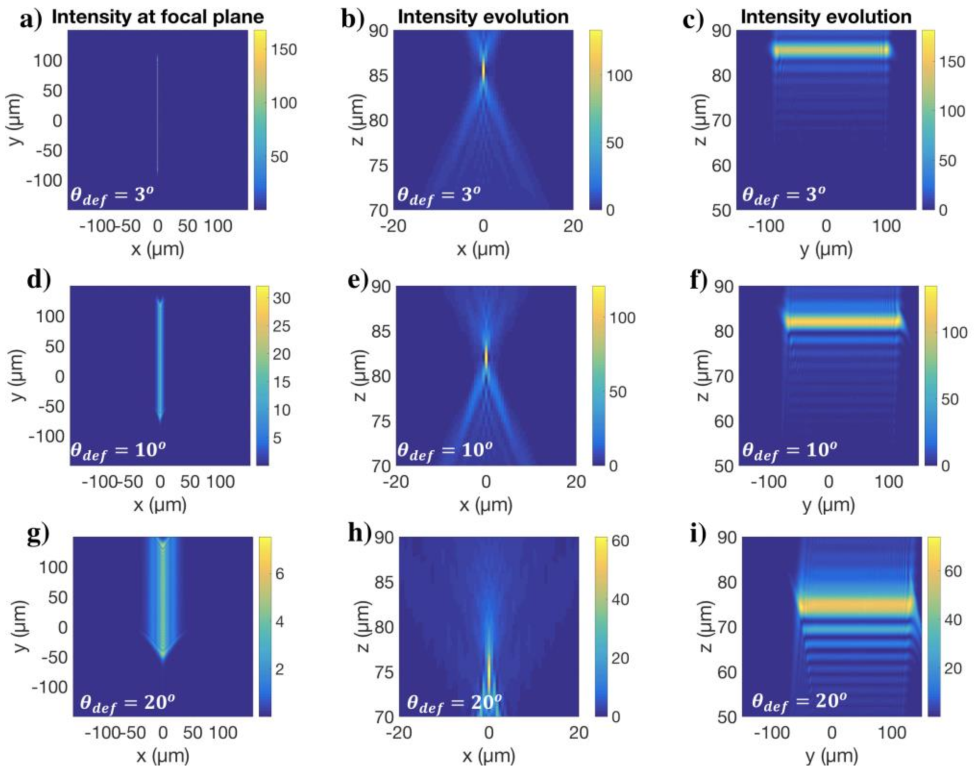

Figure 4.5: Far-field distribution of field above metasurface. Far-field distribution calculated by Fourier transform calculation of the phase and amplitude mask just after a cylindrical metalens with the focal distance of 85 µm and a beam deflector at different planes for the deflection angles of (a-c) 3°, (d-f) 10° and (g-i) 20°.

4.3 Optical manipulation of movable active metasurfaces

As observed, a metasurface can shape the wavefront of incident light, thereby altering its momentum. According to the principle of momentum conservation, the metasurface simultaneously experiences an equal and opposite momentum exchange. However, due to their large size and high friction, conventional metasurfaces typically do not actively interact with optical sources under normal conditions. In contrast, for immersion metasurfaces, if the reciprocal force generated from the momentum exchange exceeds the viscous drag, they can respond mechanically to the incident light [119, 174, 175].

4.3.1 Translation of metaparticles

As discussed in **Chapter 3**, two types of beam deflectors based on metasurfaces are commonly used: phase gradient metasurfaces and metagratings. Phase gradient metasurfaces use a supercell composed of a few numbers of unit cells that collectively span a 2π phase shift, while metagratings are designed to emulate the performance of a conventional blazed grating. Figures 4.6 (a) and (b) show SEM images of these two beam deflectors, designed to achieve deflection angles of 11° and 64° in SiO_2, as confirmed by the far-field FDTD simulations in Figure 4.6 (c). Metagrating-based beam deflectors typically support higher deflection angles and efficiencies due to their smaller lattice constants compared to the supercell size in phase gradient deflectors. Additionally, Figure 4.6 (d) illustrates a metavehicle capable of mechanical translation by converting changes in linear momentum into lateral optical forces, as demonstrated in the snapshots of Figure 4.6 (e).

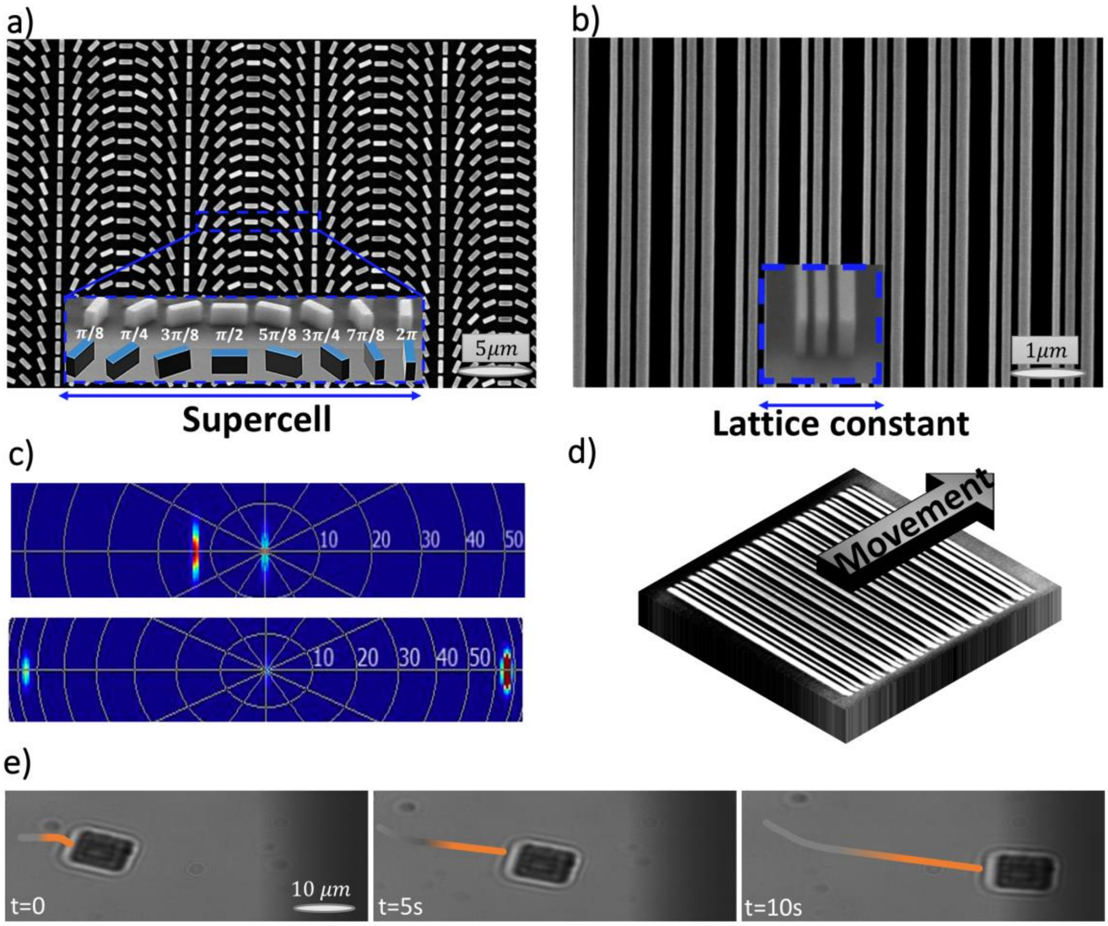

Figure 4.6: Beam deflectors based on (a) phase gradient and (b) Metagrating metasurfaces with (c) the deflection angles of 11° and 64° calculated by FDTD simulations in the far-field for 1064 nm laser source with left-handed circularly and linear polarized light. (d) A metavehicle consists of the metagratings shown in (b). (e) Snapshots of translation of the metavehicle (illustrated in (d)) with an average speed of 4 μm/s. The metavehicle is excited at 1064 nm with linearly polarized light and $I = 1\ \mu W/\mu m^2$.

To highlight the importance of grating parameters on the generation of lateral optical forces through asymmetric diffraction, Figure 4.7 compares the experimental outcomes with those from the previous study [119]. The experimental fitness function of $F_{exp} = \frac{F_{optical}}{F_{radiation\ pressure}}$ is defined for comparing vehicles, where $F_{optical} = \gamma v$ is the optical force, γ is the drag coefficient, υ is the linear speed. The radiation pressure is $\frac{n\,A\,I}{c}$, where c is the speed of light, *n* is the refractive index of water, *I* is the incident intensity and *A* is the metasurface area. Figure 4.7 (a) shows the relationship between metavehicle velocity as function of the incident intensity, with the slope representing $\frac{v}{I}$. Given the similar size, shape, and materials, we assume the drag coefficient remains constant when compared to previous work [119]. This yields $\frac{F_{exp}}{F_{exp\ prior\ art}} \approx 2$, indicating enhanced efficiency in the conversion of light momentum to the linear motion of the metavehicle.

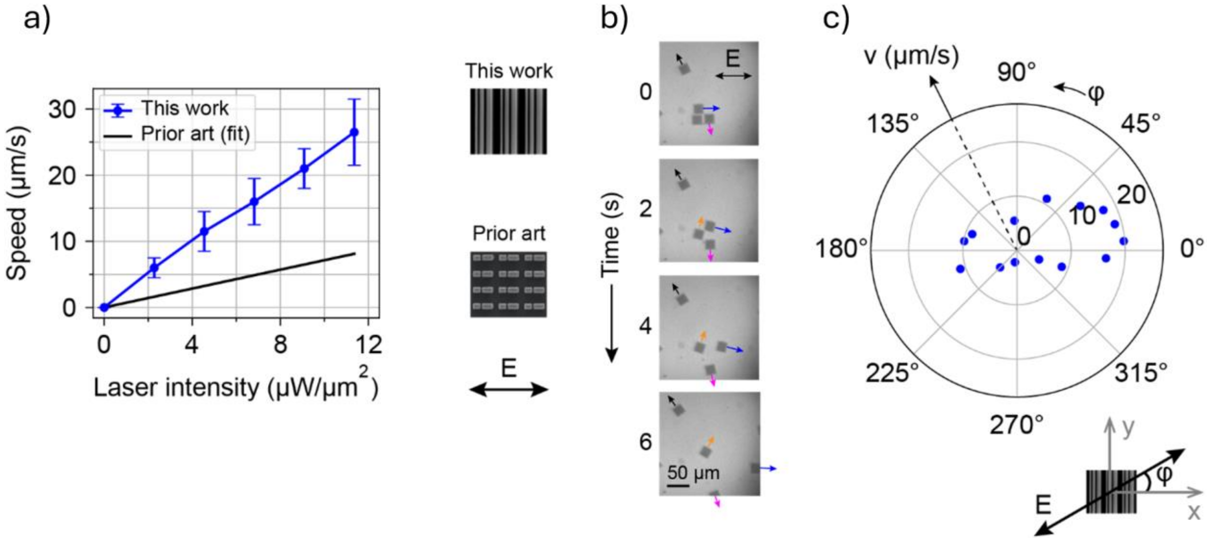

Figure 4.7: (a) Metavehicle speed at different incident laser intensities shown against the prior work [119]. Metagrating unit cell consists of three Si ridges of widths $W_{1,2,3}$ = 60 nm, 140 nm, 220 nm, height H = 370 nm, periodicity P = 826 nm, and the same gap g = 76 nm (facet-to-facet distance) between the ridges inside the cell. It is worth highlighting that these parameters are different from the grating used in **Papers II** and **III**. (b) Snapshots of the metasurface traveling in water in different directions. (c) Metavehicle speeds at different polarization angles excited at 1064 nm with linearly polarized light and I = 10 μW/μm^2 (unpublished data).

These gratings are specifically designed for x-polarized light, which leads to different movement speeds for metavehicle depending on their orientation relative to the incident polarization (Figures 4.7 (b) and (c)). As expected, when the polarization of the incident light is aligned with the grating ridges, the metavehicle achieves its maximum speed. Conversely, when aligned orthogonally, the vehicle exhibits the slowest movement.

4.3.2 Rotation of metaparticles

In addition to translating metasurface with linear polarization, they can be steered using circular polarization. Under circularly polarized illumination, the metavehicle experiences a torque that follows the handedness of the incoming light. Due to symmetry, the angular velocity of vehicle is independent of orientation of grating. In addition to transferring spin from the incident light, the circularly polarized wave also induces partial deflection. Hence, the combined transfer of angular and linear momentum results in orbital motion and is shown in Figures 4.8 (a)-(d).

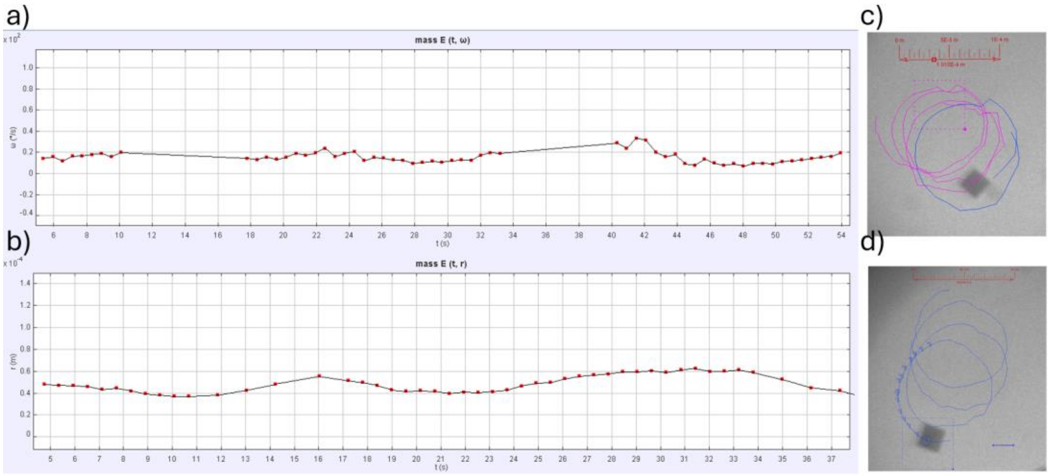

Figure 4.8: Metaparticle dynamics in a circularly polarized light. (a) Evolution of the angular velocity under a LCP light with I ≈ 6 μW/μm^2 with an average angular velocity around 18 °/s. (b) Orbital rotation radius with an average of 50 μm (c-d) Snapshots display the trajectory illustrating orbital motion. Displacement in the orbital path is due to slight misalignments in the optical setup (unpublished data).

Moreover, the distribution of linear momentum can also be utilized to rotate a metavehicle. Various methods have been employed to rotate an object using a linearly polarized plane wave, including the implementation of chiral or birefringent structures, breaking the symmetry of the objects, guiding the light through a curved path and creating uneven light-matter interactions across different sections of a rotor, as illustrated in Figure 4.9. This figure illustrates that when spatial dependency is added by placing different grating orientations, the interaction of the incident light and the rotor can generate an optical torque. For instance, the rotor shown in Figures 4.9 (a)-(c) can rotate with a linearly polarized light because of different directions of optical reaction forces at each section of gratings. These optically flat rotors with substantial moments of the arm exceeding tens of microns able to transfer unprecedented optical torques. See **Paper III** for details in instantaneous and average optical torques of rotor in Figure 4.9 (c).

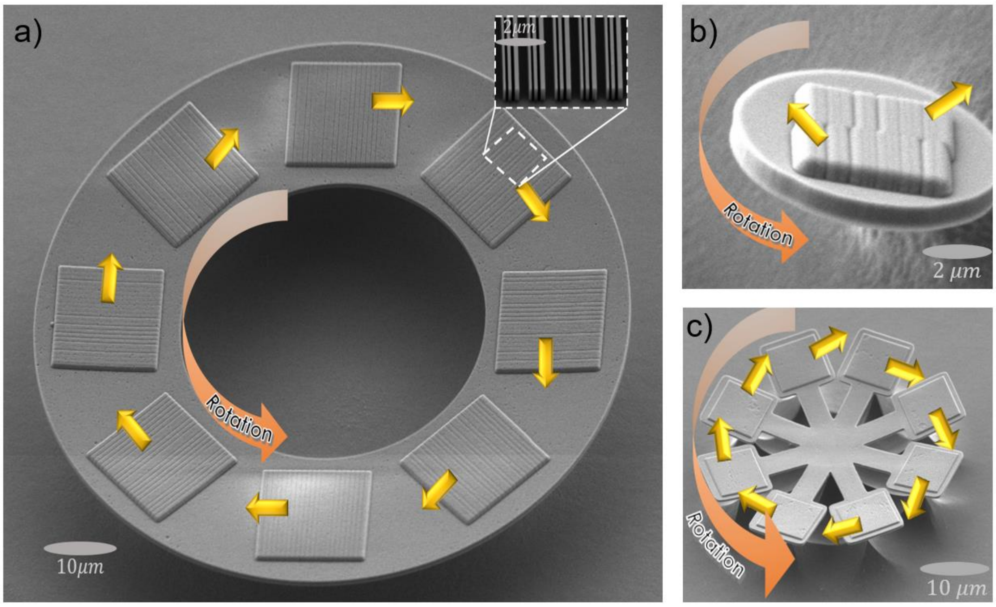

Figure 4.9: SEM image of grating-based rotors with embedded gratings that deflect light and rotate in the direction shown with yellow and orange arrows, respectively. (a) Doughnut-shaped particle with an outer diameter of 100 µm equipped with squared gratings with a size of 15 µm. (b) Circular rotor with a diameter of 8 µm consists of two grating sections used for **Paper II**. (c) Star-shaped rotor with a size of 60 µm and 8 µm squared gratings at each arm. The designs of the larger rotors in (a) and (c) account for fabrication constraints, particularly during the detachment step.

The compact size of the gratings, combined with their efficient light-bending at significant angles of approximately 64°, enables the rotation of large rotors exceeding 100 µm in diameter. To our knowledge, there are no prior reports of optical manipulation for rotors of this size. The snapshots in Figure 4.10 depict the simultaneous rotation of three rotors, measuring 100 µm and 50 µm.

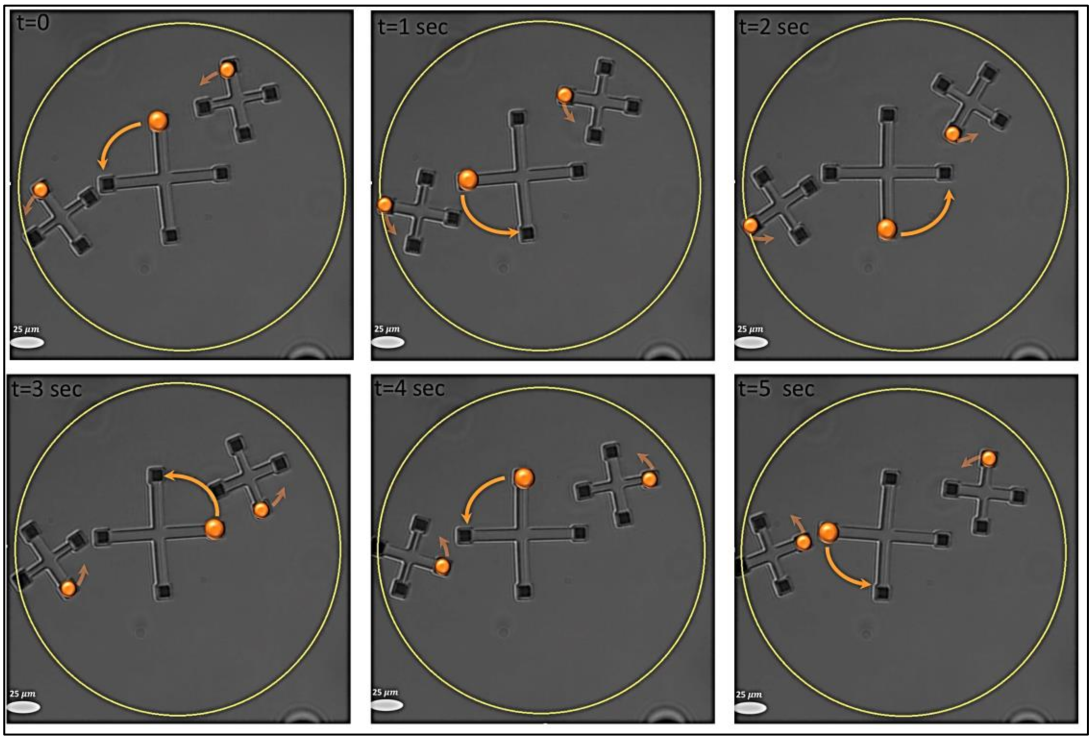

Figure 4.10: Spinning of rotors. Snapshots of the rotation of three rotors. The rotors were excited by a linearly polarized Gaussian beam with a wavelength of 1064 nm, with I ≈ 100 µW/µm^2. The larger rotor at the center of the beam rotates at a higher rate (90 °/s) than the smaller rotors at the lower intensities of the beam (54 °/s).

Considering the discussion in **Chapter** 3, in the interaction of a grating-based rotor a transverse gradient force creates an unconventional orbital motion. However, this unconventional behavior has been extensively studied in **Paper II** for a pair of 8 µm circular rotors. Figure 4.11 shows another picture of this force on larger rotors with different shapes with respect to what is studied in **Paper II**. In Figure 4.11 a counter clockwise spinning 50 µm rotor orbits clockwise around another 100 µm spinning rotor. In this case, the larger rotor occupied the center of beam, makes the gratings on the other rotor receive different intensities and consequently, a net force on its center of mass as shown in Figure 4.11.

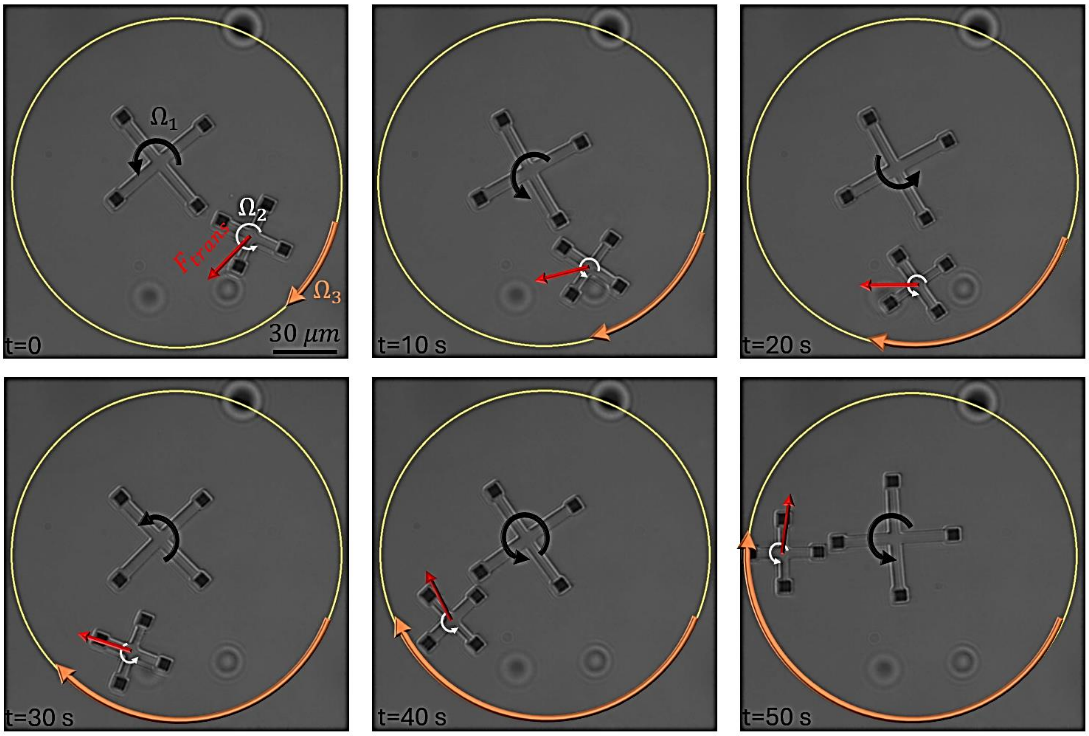

Figure 4.11: Spin and orbital motion of rotors. Snapshots of spinning rotor with 100 µm size and angular velocity $\Omega_1 = 90$ °/s located in the center of a linearly polarized Gaussian beam with a wavelength of 1064 nm and I ≈ 100 µW/µm^2. A smaller rotor, 50 µm in size, orbits around the larger rotor with a spinning velocity of $\Omega_2 \approx 51$ °/s and an orbital angular velocity of $\Omega_3 \approx 25$ °/s. The direction of the transverse gradient force is indicated by red arrows in each snapshot.

In the examples presented so far, the rotors and vehicles are positioned inside a chamber assembled by two cover glasses with a depth of approximately 110 µm. Additionally, in previous examples, the rotors were pushed to the bottom of the chamber by a laser beam directed from the top, as illustrated in Figure 4.12 (a). However, it is also possible to lift the rotors by utilizing the scattering force from a laser beam directed from the bottom of the chamber, as schematically shown in Figure 4.12 (b). Moreover, the other possibility is sending light from both directions to control the interaction of the rotor and the bottom surface (Figure 4.12 (c)). Figure 4.12 (d) summarizes the measurement of rotation velocity for different combinations of laser power from upside and downside. The measurement shows when the rotors are exited from the upside, a nonlinear dependency exists between the rotation velocity and incident power. It is worth mentioning, the reason for this supralinear variation in velocity can be explained through the photothermal heating rotor and the decreasing of water viscosity surrounding the rotor. When the rotors are excited from both sides (50% / 50%), the relationship gets more linear. A hypothesis can be related to the changes of distribution of temperature when the gap between the rotor and bottom surface increases. More analysis is needed in this case to explore the exact reason for having linear or nonlinear relationships. The increments in the gap distances between the rotor and bottom side also affect the rotation drag coefficient and consequently, reach higher velocity for each power. In Figure 4.12 (d), the purple circles represent the measurement results for two different rotors when the light illuminates the rotors exclusively from below. In this configuration, the rotors are lifted by the upward-directed beam once the incident power reaches 600 mW. Details of the measurement optical setup are presented in Figure 5.15.

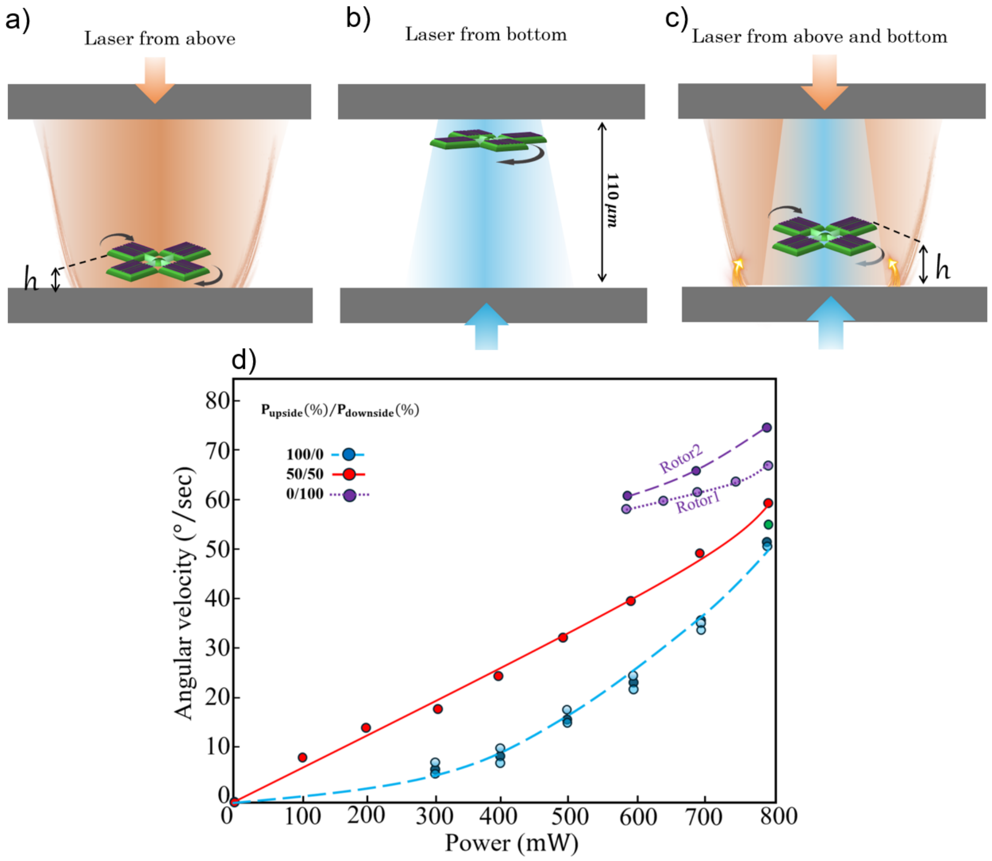

Figure 4.12: Rotor excited by laser from (a) above, (b) bottom and (c) both sides of chamber. (d) Angular velocity of 30 µm rotors as a function of power and the ratio between upside and downside laser beam (Shanei, et al., unpublished data).

4.3.3 Manipulation of particles by rotors

Hydrodynamic coupling occurs when the motion of one rotor affects the fluid flow, influencing nearby rotors and particles as shown in Figures 4.13 (a)-(c). Figure 4.13 (a) illustrates the manipulation of 7-µm PS beads using a 60 µm spinning rotor excited by a Gaussian beam with an intensity of I ≈25 µW·µm^{-2}. The rotor spins at angular velocity of 40 °/s, while the orbital velocities of particles vary from 18 °/s to 4 °/s.

In Figure 4.13 (b), the experiment analyzed the behavior of 1-µm PS beads in the vicinity of a rotor spinning at approximately 1500°/s excited by a light beam intensity of 90 µW·µm^{-2}. The experiment shows the beads were pulled radially towards the rotor due to a convective flow caused by a thermal gradient generated by the rotor. As the beads approached the rotor's edge, they gained an azimuthal velocity of around 146°/s, consistent with the rotor's spinning direction. The lack of bead movement when the rotor was outside the beam center indicated that optical gradient forces had minimal effect. Instead, the convective flow was primarily driven by localized photothermal heating of the rotor itself. Fluid dynamics simulations closely matched the observed azimuthal speeds and confirmed that the flow diminished beyond the rotor’s edge. (See **Paper II** for details).

In a setup with two rotors spinning in the same direction, as shown in Figure 14.13 (c), they create a symmetric flow field that induces stable orbital motion. Conversely, when the rotors spin in opposite directions, they generate a net translational flow field, resulting in translation of the rotors and surrounding particles through the fluid [176]. These behaviors highlight the versatility of hydrodynamic manipulation in controlling particle motion and flow dynamics.

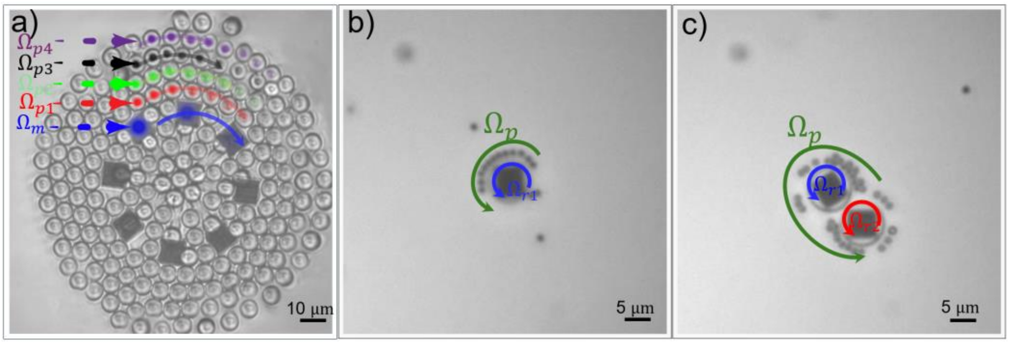

Figure 4.13: Optical manipulation through spinning rotors. (a) A 60-µm rotor excited by a Gaussian beam with an intensity of I ≈25 µW·µm^{-2} spinning with angular velocity of 40 °/s. The orbital angular velocity of particles at each row are 18 °/s, 12 °/s, 6 °/s, 4 °/s. (b) A 8 µm rotor excited by a beam with intensity I ≈ 90 µW·µm^{-2} and with angular velocity of 1500 °/s and 146 °/s for surrounding particles. (c) Co-spinning rotors with angular velocity around 720 °/s for rotors and 45 °/s for particles excited by 75 µW·µm^{-2}

To study the created fluidic flow through the rotation of the rotor and to evaluate the mechanical capability of the rotor shown in Figure 4.13 (a) with 60 µm diameter, a finite element fluid dynamics simulation is performed at room temperature in water. The fluidic flow results are summarized in Figure 4.14 (see **Chapter 5** for more details). A key parameter in these simulations is the distance between the rotor and the bottom surface of the chamber. This surface imposes a no-slip boundary condition on the induced flows, increasing rotational drag compared to a freely rotating rotor. In this simulation we have a 282 nm gap between rotor and the bottom of the chamber. (see appended **Paper III** for details in estimation of the gap). The results show that fluid velocity diminishes rapidly with distance, particularly in the radial direction, where the decay length is only a small fraction of the rotor radius. This behavior is primarily attributed to the rotor flat profile and the no-slip boundary condition at the chamber's bottom.

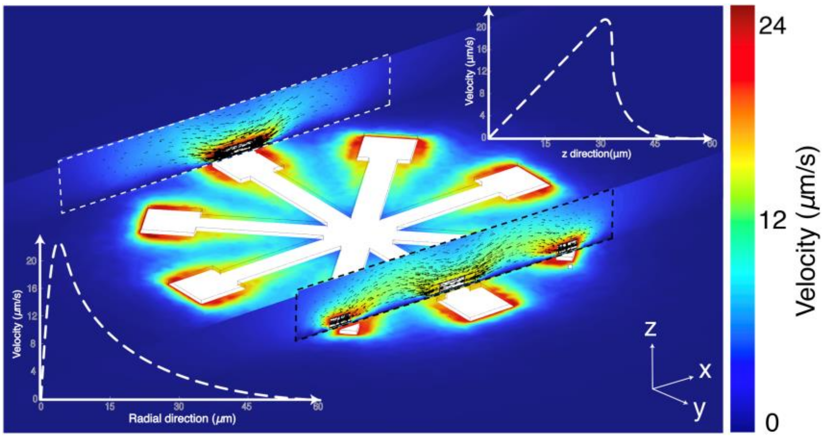

Figure 4.14: Simulated flows around a rotating rotor. Flow profiles around the rotor. The upper and lower crossed section panels show vertical flow vector profiles at the inner and outer periphery of a grating. The insects show the simulated average fluid velocity magnitude variation along the radial direction just above the rotor (z = 1.1 µm) and in the normal direction at r = 30 µm. Rotor rotates with an angular speed of 50 $^{\circ}$/s at d = 282 nm.

4.3. Trapping of particles by free immersion metalens

Water immersion objectives are crucial components in microscopy and optical manipulation of particles. Submerging a lens in liquids with higher refractive indices than free space can enhance the resolution and numerical aperture by a factor equivalent to the refractive index of the employed liquid. This section introduces a new approach to do optical trapping with the movable metalenses. These planar immersion swimmer lenses could align themselves with the center of the incident Gaussian beam profile. Acting as a supplementary platform, the metalenses enhance the numerical aperture and reduce the beam size of the primary conventional objective lens. This increase in numerical aperture makes our configuration well-suited for optical particle trapping. This kind of free-immersion lens can open promising possibilities for more efficient optical manipulation.

To design the metalenses shown in Figure 4.15 (a), a dynamic phase approach has been used to manipulate the Gaussian incident beam. The building block of our metalens comprises a-Si cylinders (n = 3.79) arranged in a square lattice with a periodicity of 340 nm on a fused silica (n = 1.45) substrate submerged in the water (n = 1.33). Figure 4.15 (b) shows the extracted phase shift and amplitude of cylinders as the radius for P = 340 nm and h = 490 nm at $\lambda = 1064$ nm. Figures 4.15 (c) and (d) demonstrate the optical and SEM images of designed metalens.

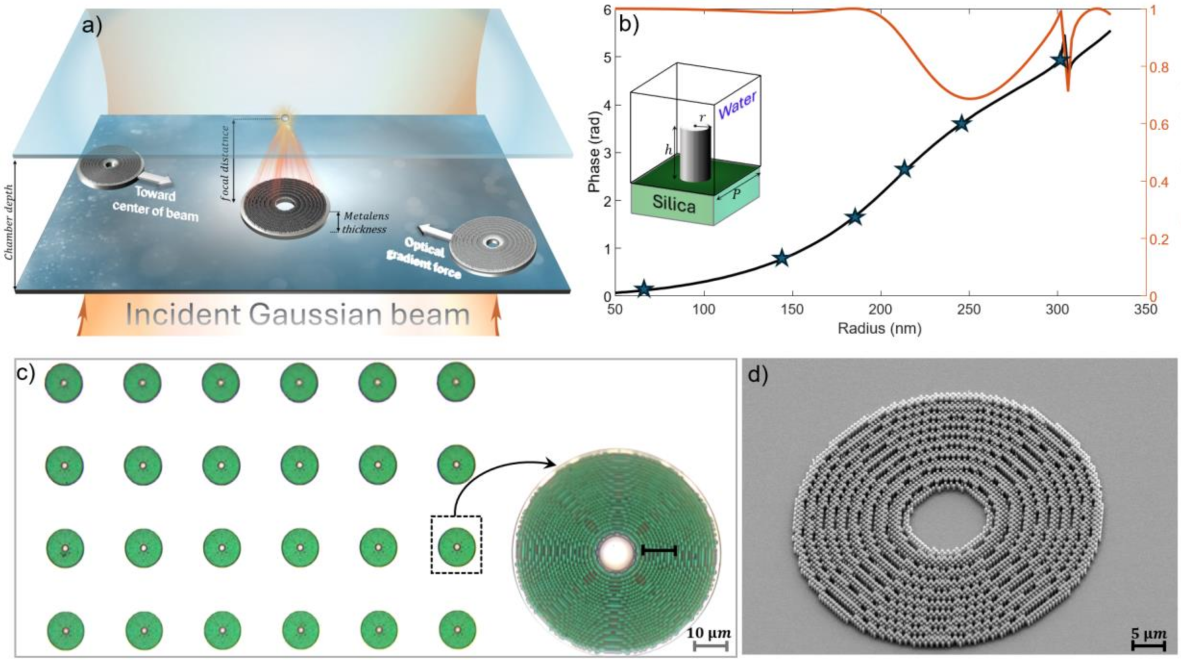

Figure 4.15: (a) Schematic of immersion metalenses. (b) Phase and amplitude of transmitted electric field through metaatoms as the function of the radius of cylinders located on the silica and submerged in water. (c) Optical images of a series of fabricated metalenses. (d) SEM images of a metalens (Shanei, et al., unpublished data).

To simulate the performance of a metalens submerged in water, the complex near-field profile of the metalens was captured by assigning the transmitted amplitude and phase of metaatoms, the far-field profile can be calculated using the Fresnel diffraction integral. Here, a Gaussian intensity profile incident on the metalens with the inner and outer radii of r_i = 5 µm and r_o = 25 µm are consider. Figures 4.16 (a-b) and (d-e) illustrate both the simulation and experimental results of the intensity profiles of the propagating beam in the xz-and xy-planes after it passes through the metalens. The results show a focal point of f = 30 µm with a numerical aperture of 0.86 in water. In Figure 4.16 (c), the intensity profiles along the focal point in the xy-plane revealing a full width at half maximum (FWHM) of approximately 5 µm. This measurement exceeds the diffraction limit, due to the unmodulated light passing through the center of the lens.

As a proof of concept and to demonstrate the possibility of the trapping with movable metalens, a closed cylindrical chamber cell has been prepared with approximately 9 mm diameter and 30 µm depth, which is adjusted to coincide with the metalens focal distance. The chamber contained a dilute solution of metalenses dispersed in deionized water containing 0.8-µm PS beads. Figure 4.16 (f) shows a snapshot of an immersion metalens at the bottom and the inset demonstrates a 2D trapped PS bead at the focal plane located at the top side of chamber.

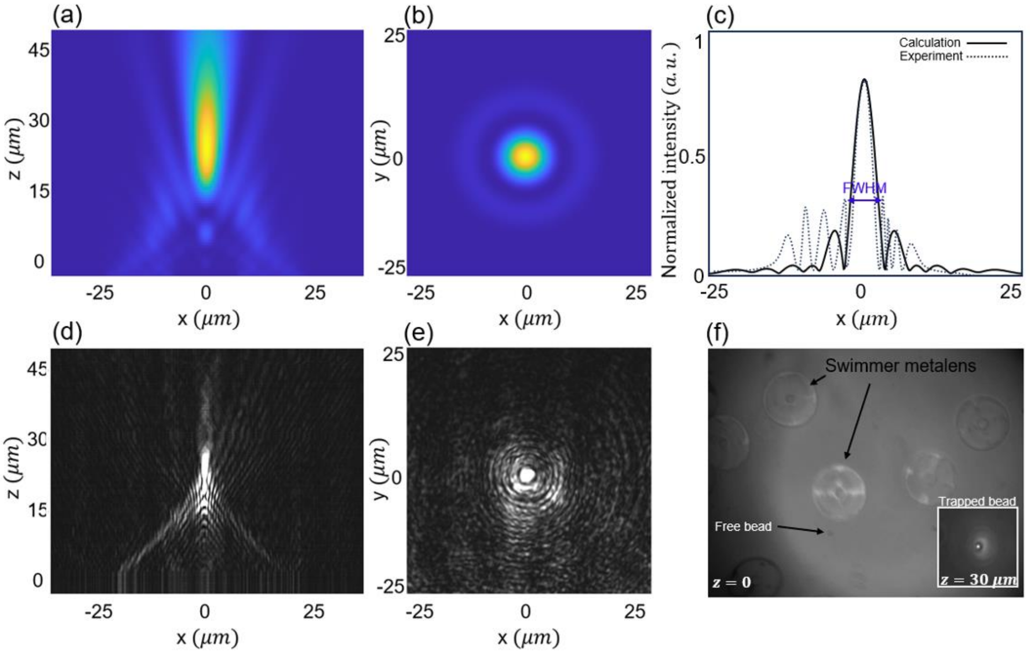

Figure 4.16: Calculated intensity distributions in (a) xz- and (b) xy-planes. (c) Calculated and measured intensity profiles at the focal plane. Measured intensity distributions in (d) xz- (e) xy-planes. (f) Snapshot from swimmer metalens showing the trapping of a PS bead in the inset at z = 30 µm (Shanei, et al., unpublished data).

Chapter 5

Research methods

This chapter provides an overview of the research methodologies employed in this thesis. These methodologies are complementary to the studies presented in **Papers I**, **II**, and **III** and their supplementary materials. The chapter is divided into three main sections of calculations, fabrication and optical measurements.

The calculations section describes the computational approaches used to model and analyze metasurfaces. These include finite-difference time-domain (FDTD) simulations, finite element method (FEM) simulations, and far-field calculations to evaluate the scattering behavior of the metasurfaces. The second section covers the micro and nanofabrication processes employed to make metasurfaces. The last part of this chapter focuses on the experimental optical setups used to validate theoretical predictions and characterize the fabricated samples.

5.1. Numerical simulations

5.1.1. Finite-difference time-domain (FDTD) simulations

In optics and photonics, numerical calculations are essential for optimizing and analyzing metasurfaces, offering benefits such as metaatom optimization and performance analysis of the metasurface. Various methods have been employed for these calculations. While many electromagnetic simulations solve Maxwell's equations in the frequency domain, the FDTD method calculates the progression of electromagnetic field values at discrete time steps. Further details on the advantages of this technique are provided in [177].

In this study, to optimize a building block of metasurface, its geometric shape and material composition are first defined in the FDTD simulator. Typically, periodic boundary conditions

(PBC) are applied in the plane parallel to the metasurface, while a perfectly matched layer (PML) is used as an absorbing boundary in the direction of light propagation.

In this thesis, electrodynamics simulations were conducted using the FDTD method with Ansys Lumerical. The following sections briefly explore examples of FDTD applications, including the optimization of a metalens building block, the performance analysis of a beam deflector, and the study of the Maxwell stress tensor.

FDTD simulations for polarization conversion efficiency (PCE)

When designing metasurfaces based on the PB phase approach, as described in **Paper I**, it is crucial to simulate the polarization conversion efficiency (PCE) of individual unit cells, which serve as the building blocks of the metasurface. The PCE measures how effectively the metasurface converts incident light of one polarization (e.g., left circularly polarized light) into a different polarization (e.g., right circularly polarized light) after interacting with the unit cell. These unit cells are designed to impart a specific phase shift to the incident light by rotating its polarization state. To obtain this information, FDTD simulations are conducted on a single unit cell, with PBC and a PML in both the in-plane and out-of-plane directions, respectively. Figure 5.1 shows the PCE for a unit cell with a periodicity of 500 nm, which contains a-Si with a height of 490 nm, and has length *l* and width *w*. The dashed line indicates the operating wavelength used in **Paper I**.

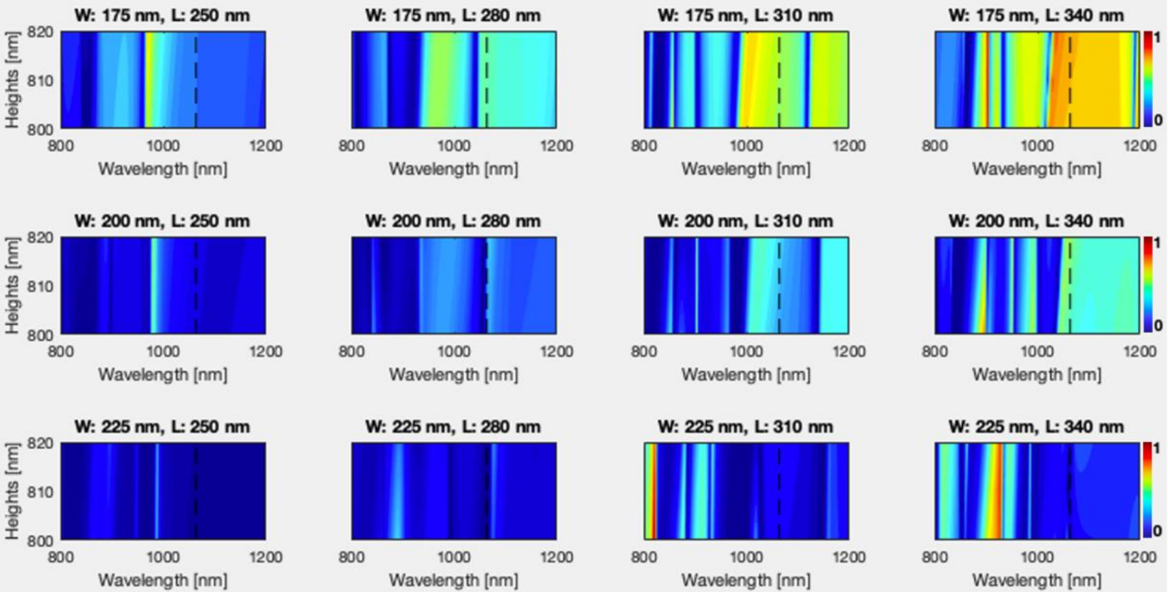

Figure 5.1: Examples of polarization conversion efficiencies for silicon nanofins located on the top of SiO_2 with n=1.45 and surrounded by water with n=1.33, as a function of width, length, height, and wavelength. The color map represents the PCE.

FDTD simulations for beam bending of the metagratings

The design of the beam deflectors, discussed in **Papers II** and **III**, was done through the optimization of a metagrating using FDTD simulations. The optimization process focused on identifying five key parameters: the metagrating's height, three distinct ridge widths, and the gap between the ridges, all aimed at maximizing the transverse momentum.

The FDTD simulations also provide information about the radiation pattern, which shows the distribution of electromagnetic field intensity as a function of direction in space. This pattern offers insight into how the energy of the bent beam is radiated or directed after interacting with the metagrating. To achieve this, the near-field data obtained from the monitors were processed to extract the far-field radiation pattern, enabling the calculation of the number of diffracted orders and their efficiencies. Details regarding the diffraction efficiencies and their dependence on incident polarization are presented in **Papers II** and **III**.

FDTD simulations based on Maxwell stress tensor

In this thesis, electromagnetic simulations for calculating the optical force and torque were performed by Dr. Vasilii Mylinkov using Ansys Lumerical FDTD software in a 3D domain, employing PML boundary conditions. To analyze the optical forces and torques exerted on an object, the Maxwell stress tensor denoted as T_{ij} quantifies the stress and momentum transfer due to scattered electromagnetic fields. This tensor is expressed as $\epsilon E_i E_j^* + \mu H_i H_j^* - \frac{1}{2}\delta_{ij}(\epsilon|E|^2 + \mu|H|^2)$, where ϵ and μ represent the permittivity and permeability of the background medium, respectively. E_i and H_i are the complex amplitudes of the electric and magnetic fields' scalar components.

5.1.2. Finite element method (FEM) simulations

Computational fluid dynamics (CFD) simulations

To analyze the laminar flow and viscous drag acting on rotors, CFD simulations were conducted in COMSOL Multiphysics using the FEM technique. This section focuses on comparing CFD simulations with analytical calculations of laminar flow dynamics around a rotating sphere. This comparison is used to validate the accuracy and reliability of the CFD simulations used in **Papers II** and **III**. Additionally, an approach for extracting the viscous torque exerted on a rotating object using CFD simulations is explored. The results are then compared with analytical calculations to confirm the simulation methodology.

The laminar flow dynamics around a rotating 100 nm sphere at a frequency of 1 kHz within a cylindrical chamber were analyzed using the Navier-Stokes equation:

$$\rho\left(\frac{\partial \mathbf{v}}{\partial t} + (\mathbf{v}\cdot\nabla)\mathbf{v}\right) = -\nabla p + \mu\nabla^2\mathbf{v} \tag{5.1}$$

where ρ is the density, v is the velocity vector, t is time, p is pressure, and μ is dynamic viscosity. The analysis was conducted under low Reynolds number conditions and for an incompressible fluid.

The simulation domain consists of a cylindrical chamber with dimensions of 2 µm in diameter and 750 nm in height (along the z-axis). The sphere is initially positioned at a specified gap distance from the bottom of the chamber, and during the simulation, the gap parameter is systematically varied. The fluid in the simulation is modeled as water at room temperature, with a dynamic viscosity of 0.001 Pa.s and a density of 1000 kg/m³.

Boundary conditions include a no-slip condition applied to the sphere's surface as well as the top and bottom surfaces of the chamber. Considering the incompressibility condition $\nabla . \mathrm{v} = 0$, which essentially reflects the conservation of mass and ensures no significant changes in density within the fluid. In simple terms, it means that the volume of a fluid element does not change as it moves, which implies that the fluid's density remains constant. It simplifies the mathematical description of fluid flow. Additionally, at low Reynolds numbers, where $(v.\nabla)v = 0$, the inertial terms become less significant compared to the viscous terms in the momentum equation. The following section presents a step-by-step simulation technique for extracting the viscous torque and rotational drag coefficient from the CFD simulations.

Figures 5.2 (a) and 5.2 (b) depict the outcomes of simulated fluidic velocity resulting from the rotation of particles positioned at the bottom of the chamber and located 50 nm above the bottom. The velocity patterns are visually presented in Figures 5.2 (c) and 5.2 (d) under the condition that the gap between the bottom and the sphere is 50 nm.

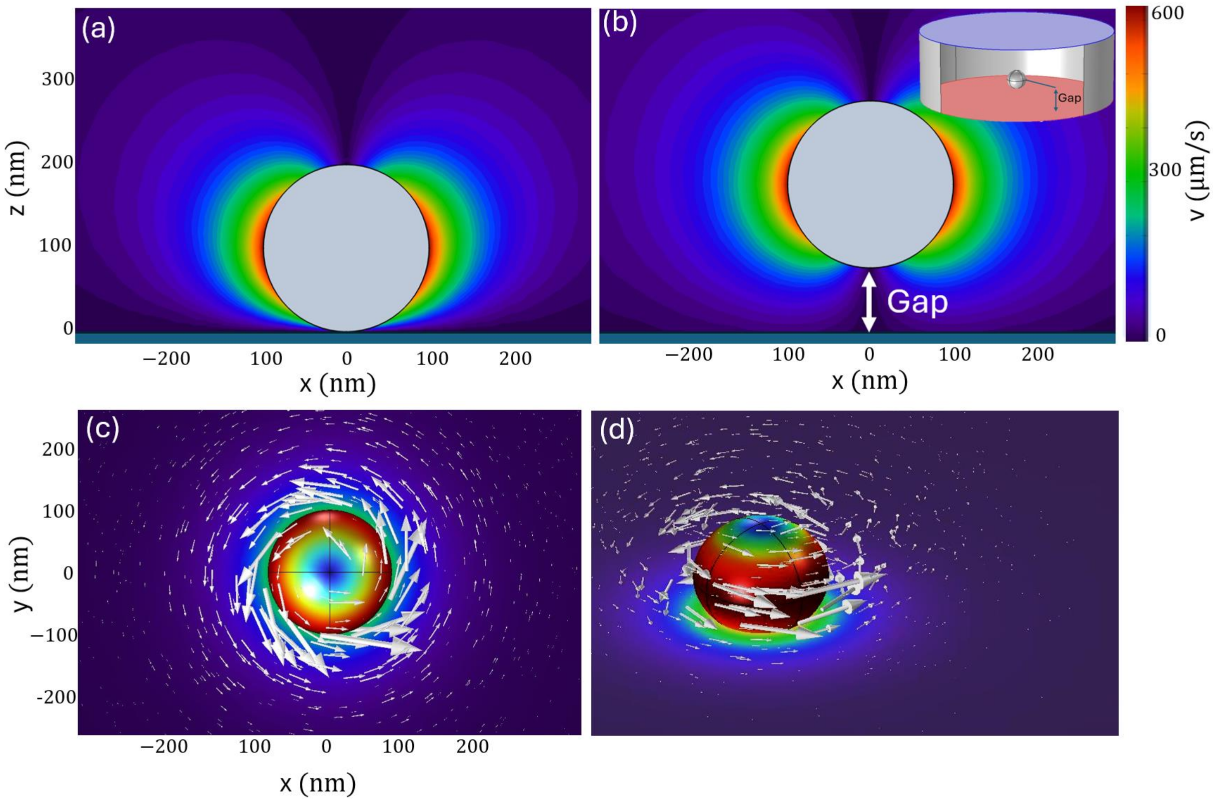

Figure 5.2: Fluidic velocity of water induced by the rotating sphere at (a) ground level and (b) with a gap of 50 nm as shown in the inset of (b). Velocity patterns from the (c) top and (d) side view when the gap is 50 nm.

Through the velocity field, the shear rate ($\dot{\gamma}$) can be estimated, which measures how fast adjacent layers of fluid move relative to each other within a flow. This is a key parameter in determining the internal forces and movement of secondary objects influenced by the fluid’s motion, as discussed in **Chapter** 3. The shear rate is defined as the rate of change of velocity with respect to the distance perpendicular to the direction of flow. In a simple case, where the velocity is in one direction (e.g., along the y-axis), the shear rate is given by $\dot{\gamma} = \frac{du}{dy}$, where du is the change in velocity in the direction of flow (e.g., here only along the y-axis).

For more complex flows, the shear rate may involve derivatives with respect to multiple spatial dimensions and is typically measured in reciprocal seconds (s^{-1}). The inset in Figure 5.3 shows the distribution of the shear rate on the surface of the examined sphere and at the bottom of the chamber.

The next step is the calculation of shear stress, which represents the force per unit area parallel to a surface, resulting from the internal friction in the Newtonian fluid as it flows. A Newtonian fluid is a type of fluid whose flow behavior is described by Newton's law of viscosity. According to this law, the shear stress (τ) in a Newtonian fluid is proportional to the shear rate ($\dot{\gamma}$) and dynamic viscosity (μ).

Then, the viscous torque M is calculated by the integral of shear stress over the sphere's surface times the corresponding radius should be considered. To verify the simulation results, the analytical Faxén approximation was used as a benchmark. Figure 5.3 compares the calculated Faxén torque with the CFD simulation results for a 100 nm sphere, as a function of the gap size. Both the analytical and simulated torques are normalized relative to the torque of a freely rotating sphere. The comparison shows a good agreement between two approaches.

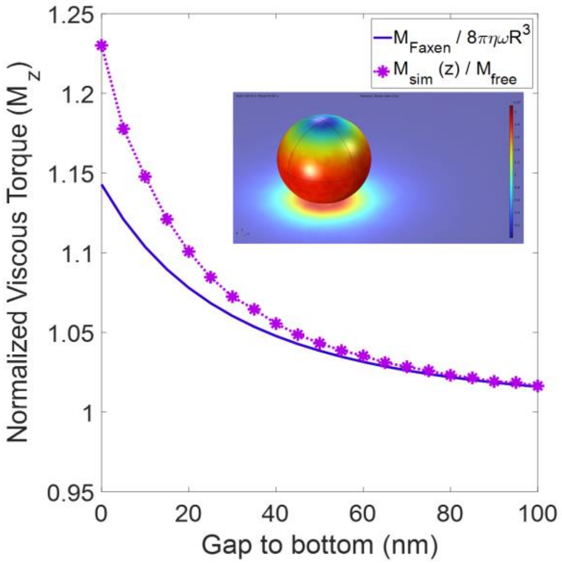

Figure 5.3: Calculated viscous torque using Faxen approximation in blue and the simulation viscous torque in purple. The inset shows the shear rate distribution on the surface of a 100 nm sphere.

Finally, from viscous torque M and the angular velocity ω the rotational drag coefficient can be estimated as:

$$M = \gamma_R \cdot \omega, \tag{5.2}$$

where γ_R is a coefficient that characterizes the interaction between a rotary object and the surrounding fluid. The value of γ_R depends on several factors, including the shape of the object, the properties of the fluid, and other parameters that affect the viscous torque on the rotating object.

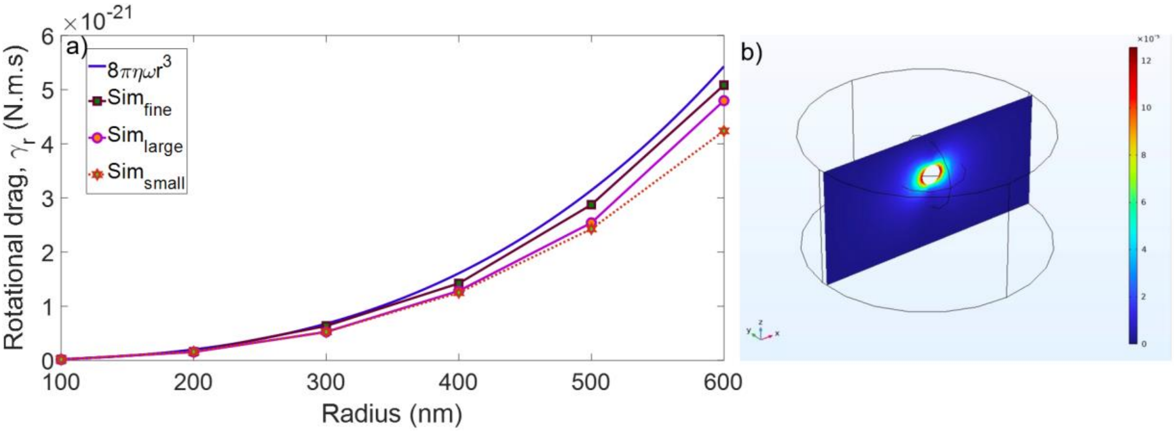

Figure 5.4: (a) Analytical calculation and simulations of a rotating sphere as a function of the radius of the sphere showing the importance of meshing size and chamber dimension in the accuracy of simulated results. (b) Velocity profile around a rotating sphere.

To evaluate the impact of mesh size and the dimensions of the simulation domain, Figure 5.4 (a) presents a comparison between the analytical and simulated drag coefficients for a rotating sphere placed at the center of the chamber, as depicted in Figure 5.4 (b), with rotation frequency of 1 kHz. The results indicate that reducing the mesh size and enlarging the chamber improves the agreement between the simulation and the analytical solution.

In conclusion, this study on laminar flow around a rotating sphere within a cylindrical chamber provides valuable insights into the sphere’s dynamic behavior. The simulation highlights the sensitivity of fluid flow to rotor size. Estimating the rotational drag coefficient further clarifies the sphere’s interaction with the surrounding fluid during rotation. The close match between CFD simulations and the Faxen approximation, particularly at larger gaps, confirms the reliability of the simulation method. Future work could involve comparing the exact solution of the Navier-Stokes equations with CFD simulations, especially when the sphere is placed near a surface with no-slip boundary conditions.

Heat transfer simulations

The rotor gratings are constructed from amorphous silicon, a material with very low absorption at 1064 nm. However, during rotor-driving experiments, photothermal heating and the resulting convection flow were observed, particularly in interactions with test beads. As a result, the silicon gratings are modeled as heat sources with a heat density of (σ_{abs}I)/V, where from σ_{abs} is absorption cross-sections of a gratings unit cell obtained through FEM calculations (COMSOL Multiphysics), I is incident irradiance, and V is volume of the structure. The absorption cross-section, σ_{abs}, is determined for unit cells submerged in water with in-plane dimensions of 0.817 × 2.5 µm for **Paper II**, and 0.817 × 8.17 µm for **Paper III**. With this heat density, the dissipation of heat within the grating and its surrounding medium can be estimated. After the calculation of the heat density, it is possible to estimate the heat dissipation within the grating and the surrounding medium.

Two main heat transfer mechanisms of conduction and convection are considered. Conduction is the process of thermal energy transition via collisions between neighboring atoms/molecules. Convection is the transfer of heat by the physical movement of a fluid (such as air or liquid) over a surface. There are two types of convection: natural (or free) convection and forced convection. Natural convection occurs due to the buoyancy-driven movement of fluid caused by temperature differences in the fluid, while forced convection involves the movement of fluid by external means such as fans or pumps.

In our simulations, we considered natural convection around the rotor. The convective heat transfer rate is described by Newton's law of cooling, $Q_{conv} = hA\ (T_s - T_\infty)$, where h is the convective heat transfer coefficient, A is the surface area, T_s is the surface temperature, and T_∞ is the ambient temperature. The value of h depends on the properties of the fluid, the nature of the flow, and the geometry of the surface. For typical conditions, we assumed an average convective heat transfer coefficient to estimate the heat loss due to convection.

The heat transfer simulation was performed using COMSOL Multiphysics, which allowed us to couple the heat conduction and convection equations. The model accounted for the heat generated within the silicon gratings, the conductive heat transfer within the silicon material, and the convective heat transfer to the surrounding environment. By solving the coupled heat transfer equations, we obtained the temperature distribution in and around the silicon gratings. The boundary conditions were set to maintain all outer boundaries at room temperature, ensuring that the heat transfer analysis accurately reflects the physical conditions. This comprehensive simulation approach enabled us to predict the thermal behavior of the silicon gratings and optimize their design for efficient heat management in practical applications. In simulations, the refractive index of silicon was taken as 3.8 + 0.0064i at 1064 nm with a thermal conductivity of 1.8 W/m·K and a density of 2329 kg/m^3. All outer boundaries with dimensions of 1 mm × 1 mm × 100 μm were maintained at room temperature.

5.1.3 Far-field calculations

The diffraction of waves can be calculated by scalar and vector diffraction solutions. Scalar diffraction theory can give accurate results for how the wave moves when certain conditions are met, such as the wave traveling in a uniform and homogeneous medium. The Rayleigh-Sommerfeld diffraction (RSD) integral calculates scalar wave propagation. In the far-field approximation, the Rayleigh-Sommerfeld integral simplifies and can be expressed in terms of the Fourier transform of the aperture's field distribution. Figure 5.5 shows the far-field projection of a phase gradient metalens (**Paper I**) when illuminated by a Gaussian beam profile

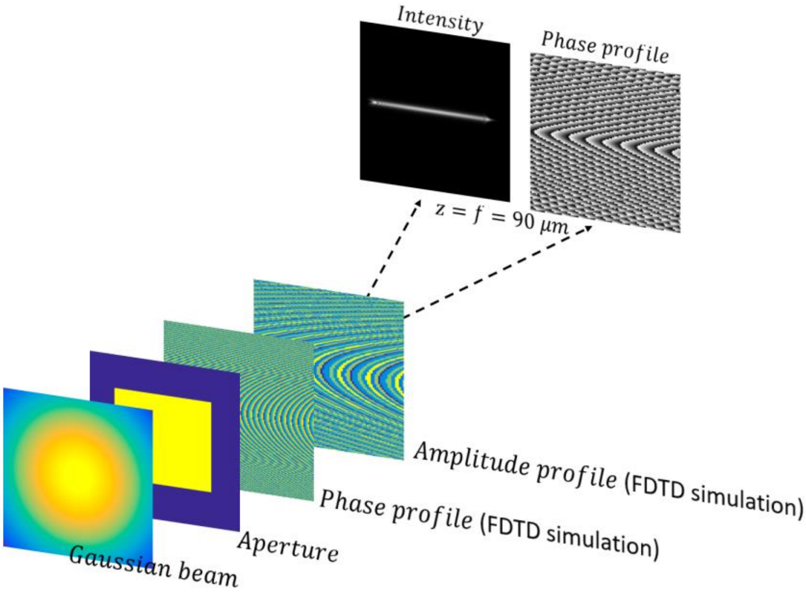

Figure 5.5: Implementing a Fourier transform to calculate a far-field projection of a Gaussian beam after traveling through an aperture with the size of a metasurface and filtering with the amplitude and phase masks obtained through FDTD simulations.

5.2. Micro and nanofabrication

Micro and nanofabrication are the basis of manufacturing for most of the modern miniaturized systems used in our daily lives, such as computer chips and detectors, mobile phones, medical instruments, and more. The fabrication techniques involve a sequence of additive and subtractive processes, which are implemented to shape a substrate into complex structures with precise, engineered materials. These techniques are divided into two main approaches. The first is the top-down approach, where a bulk material is broken down into micro or nano-scale elements through physical or chemical processes, such as etching, lithography, or deposition. This method involves removing or patterning the material at a larger scale to produce smaller structures. The second approach is bottom-up, which involves assembling structures atom by atom or molecule by molecule. This technique is commonly used to fabricate structures with a high degree of precision and control over material composition.

In the context of this report, the top-down nanofabrication method was employed, utilizing both negative and positive electron-sensitive resists to pattern the substrate. These resists play an important role in defining the structures by selectively resisting or allowing exposure to electron beams, enabling the fabrication of subwavelength features. The following parts provide a brief overview of the key process steps used in top-down fabrication methods.

Deposition:

In nanofabrication, various methods are used to deposit thin films, which are broadly categorized into chemical vapor deposition (CVD) and physical vapor deposition (PVD). In CVD, a heated substrate reacts with a mixture of gases, either thermally or using plasma, for deposition. This process relies on chemical reactions that deposit the desired materials onto the substrate in a controlled manner. Two important variants of CVD are low-pressure CVD (LPCVD) and plasma-enhanced CVD (PECVD). LPCVD operates under reduced pressure to enhance the uniformity of the film deposition, offering excellent step coverage and high-quality films that conform well to complex surfaces. PECVD, on the other hand, uses plasma to enable chemical reactions at lower temperatures, making it ideal for substrates sensitive to heat and allowing for faster deposition rates with better control over film properties such as density and stress.

Figure 5.6 (a) and (b) show the spectra of the refractive indices and extinction coefficients of a 490 nm LPCVD a-Si layer used for the fabrication of the metasurfaces in this thesis. The data presented in Figure 5.6 (a) was used in **Paper I**, while Figure 5.6 (b) was employed for **Papers**

II and **III**. The data indicates that the a-Si deposited in **Papers II** and **III** exhibits slightly higher absorption around 1064 nm.

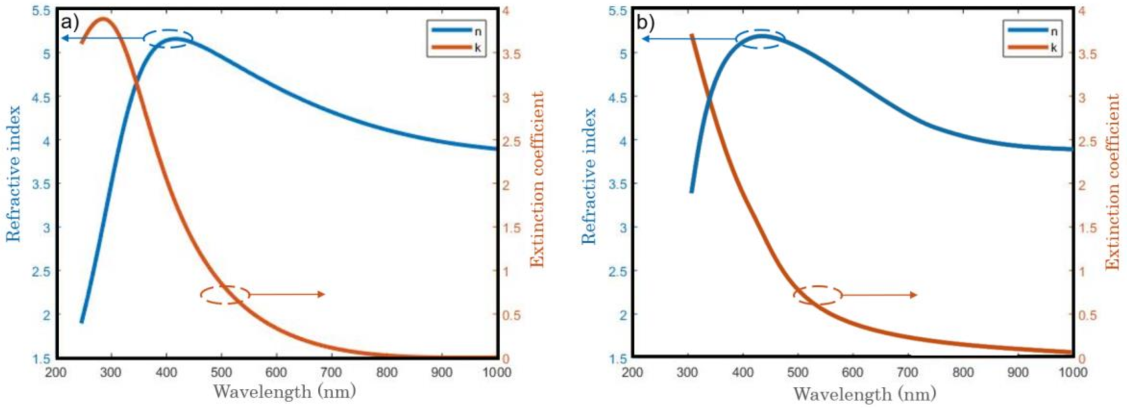

Figure 5.6: Real and imaginary parts of the dielectric function of the deposited 490 nm LPCVD a-Si. (a) at 555 ℃ measured by Woollam M2000 deposited in the Uppsala University cleanroom and (b) 540 ℃ deposited in the DTU cleanroom measured by J.A. Woollam RC2.

The two primary PVD techniques employed in this thesis are thermal/electron beam evaporation and sputtering. In thermal/electron beam evaporation, the solid material is heated either by an electron beam or induction until it evaporates and deposits onto the substrate. In sputtering, atoms are ejected through the collision of plasma ions with solid targets, allowing for uniform thin-film deposition. In this thesis, thermal/electron beam evaporation was generally used to deposit hard masks, such as nickel and chromium, onto resist layers, while sputtering was used to create a conductive layer for preventing charge accumulation during SEM imaging.

Electron beam lithography:

In top-down nanofabrication, lithography is crucial in transferring patterns to the resist. In electron beam lithography (EBL), a scanning tightly focused beam of electrons is used to pattern a surface of a resist-covered substrate with a minimum feature size around 5 nm to 10 nm. By submerging the exposed area into a proper developer, a negative or positive image will be observed on the covered substrate following the tone of the e-beam resist. After development, the final structure can be achieved by either etching the substrate or depositing the target material.

Etching:

Etching is an important step in nanofabrication to transfer a pattern into a substrate covered by a mask. The masking materials that protect the underlying substrate are divided into two categories. The first one is soft etching masks, which are the photo and electron resists patterned during lithography. The second consists of hard materials that are more durable masks, such as silicon oxide and metals. In nanofabrication, the etching processes are divided into wet and dry techniques that utilize liquid chemicals and gases as etchant material. In wet etching, the sample is submerged in a liquid while the accelerated ionized molecules of an etching gas are implemented to complete the dry etching process.

In this thesis, the inductively coupled plasma reactive ion etching (ICP-RIE) method is used to transfer the pattern of metasurfaces into the substrate. The ICP-RIE technique is a combination of chemical and physical etching that provides the possibility of isotropic and anisotropic material removal. An example of isotropic and anisotropic etching is shown in Figures 5.7 (a) and 5.7 (b).

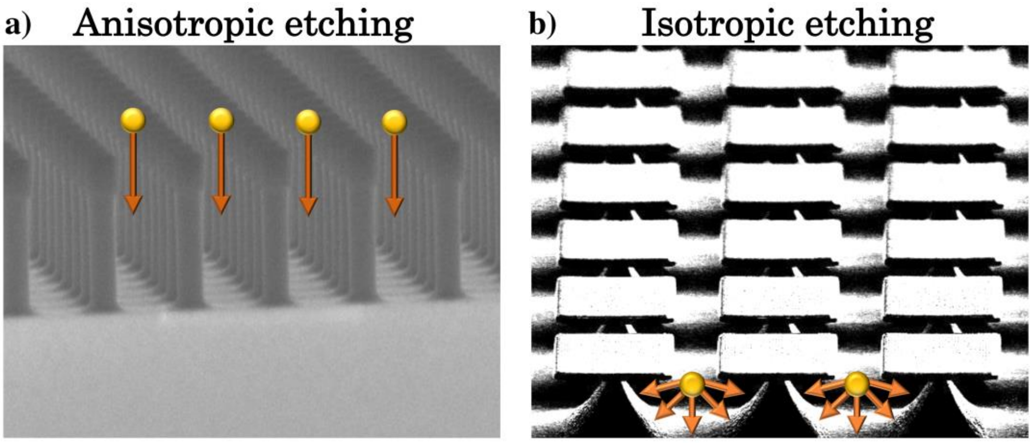

Figure 5.7: (a) Anisotropic etching to fabricate a high aspect ratio a-Si nano bars with a thickness of 980 nm using SF_6 at cryogenic temperature. (b) Isotropic etching of a-Si to release a 20 μm SiO_2 particle with embedded metasurface.

Figure 5.8 presents SEM images illustrating both unsuccessful and successful outcomes from the optimization of nanofabrication processes. These images correspond to three distinct nanostructures: nanofins (Figures 5.8 (a-c)), asymmetric dimers (Figures 5.8 (d-f)), and gratings (Figures 5.8 (g-i)).

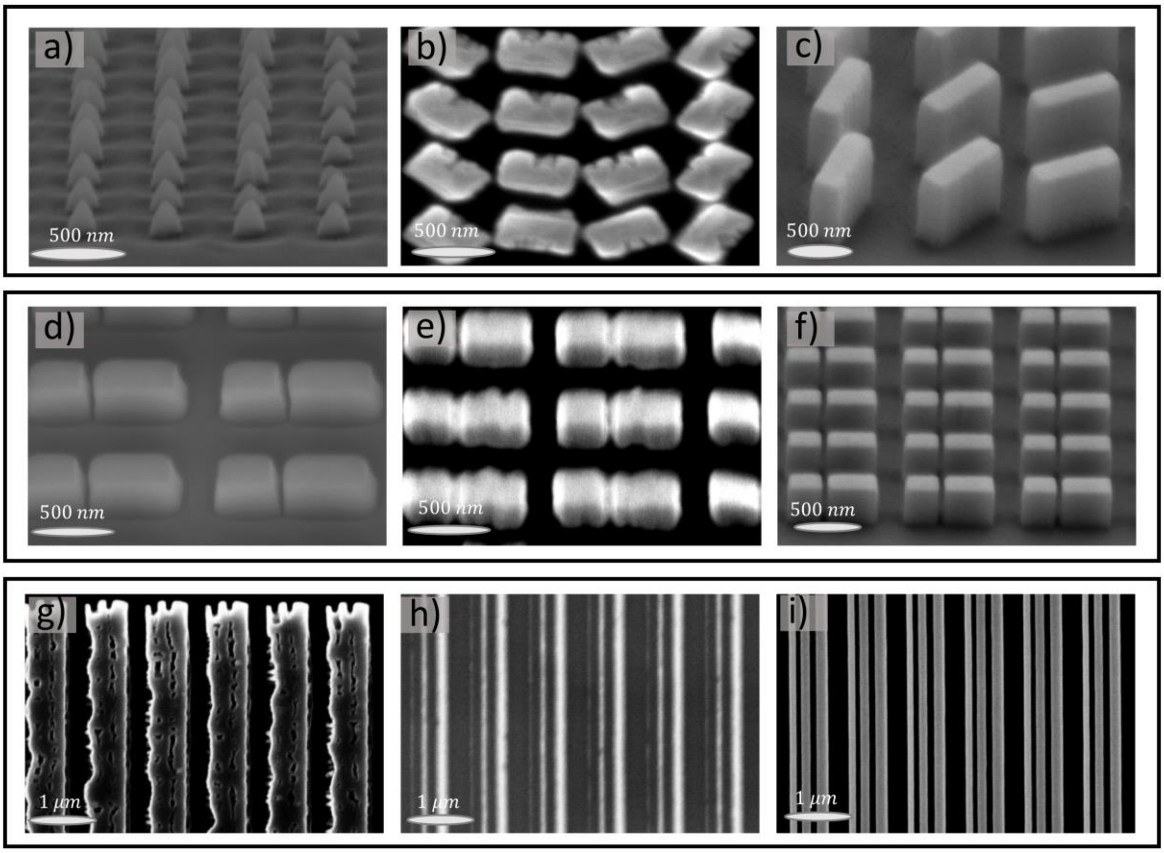

Figure 5.8 Failed attempts and final results in the fabrication of silicon-based metasurfaces. (a)-(c) Metasurfaces with a rectangular cross-section: (a) A low ratio of forward to inductively coupled plasma power results in a pyramidal cross-section. (b) Low working pressure inside the etching machine and dirties in chamber causes high-energy ion sparks, creating notches in the nanofins. (c) Successfully fabricated nanofins with vertical sidewalls and rectangular cross-sections. (d)-(f) Asymmetric dimers: (d) Uneven gap sizes and tapering sidewalls between dimers at the top and bottom, caused by insufficient forward etching power. (e) Edge roughness caused by the same issue described in (b). (f) Final structure featuring a uniform 50 nm gap between dimers. (g)-(i) Optimization of the EBL dose for grating fabrication to create three parallel solid ridges: (g) Underexposed dose, (h) overexposed dose, and (i) optimized dose achieving the desired 100 nm gap size between grating elements.

Figure 5.9 illustrates the schematics of various steps in the fabrication process of metasurfaces, as referenced in Figure 5.8 and **Paper I**, for both positive and negative resists.

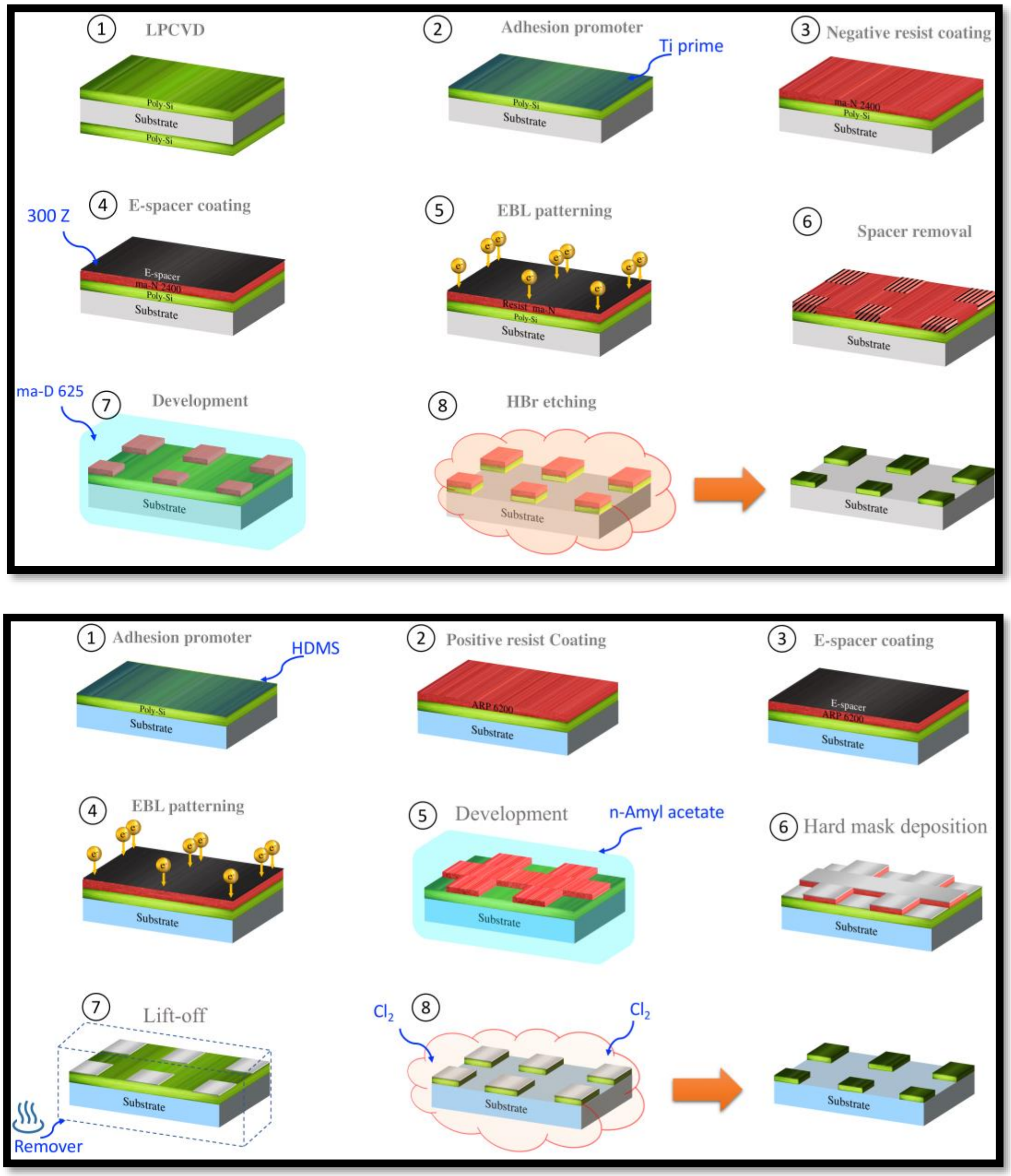

Figure 5.9: Summary of two nanoabrication techniques using negative and positive resist in the top and bottom boxes. To enhance the adhesion between the substrate and coated resist, it is suggested to use some promoters such as Ti prime and Hexamethyldisilazane (HMDS) for the negative and positive resist coating, respectively. Due to the charge accumulation in the dielectric substrate, such as SiO_2, during EBL, it is required to enhance the conductivity of the sample by coating a conductive polymer or deposition of a thin layer of metal. During the EBL and development processes, the required pattern is transferred to the resist, and then, the etching process defines the final metasurface. The negative resist in the etching process can also be used as a soft mask that can protect the covered layer (silicon). Hence, this process does not need any hard mask deposition and lift-off process.

Figure 5.10 summarizes the fabrication procedure used for **paper III**. The fabrication process in **paper II** is similar to Figure 5.10 with a different shape for metaparticles. To fabricate gratings a positive resist has been coated followed by the process shown in Figures 5.9 bottom box and 5.10.

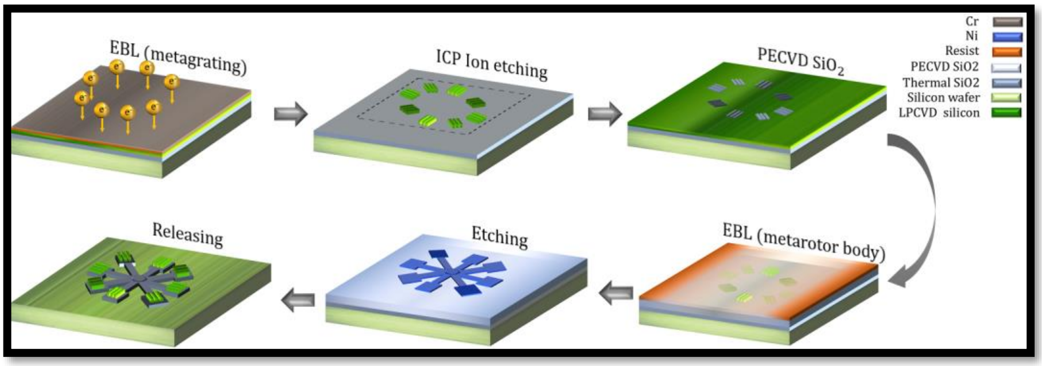

Figure 5.10: Fabrication process for metaparticles. Fabrication of gratings in first row, which involves patterning a resist using electron beam lithography (EBL) and the pattern is transferred to silicon through inductively coupled plasma (ICP) etching, see Figure 5.9 for details. Fabrication of particles with embedded metasurface (e.g. crossed-shaped rotors) in the second row, which includes a second layer exposure, etching, and finally detaching the metaparticle from its substrate.

Finally, Figure 5.11 (a-g) demonstrates the fabricated particles by the procedure of Figure 5.10.

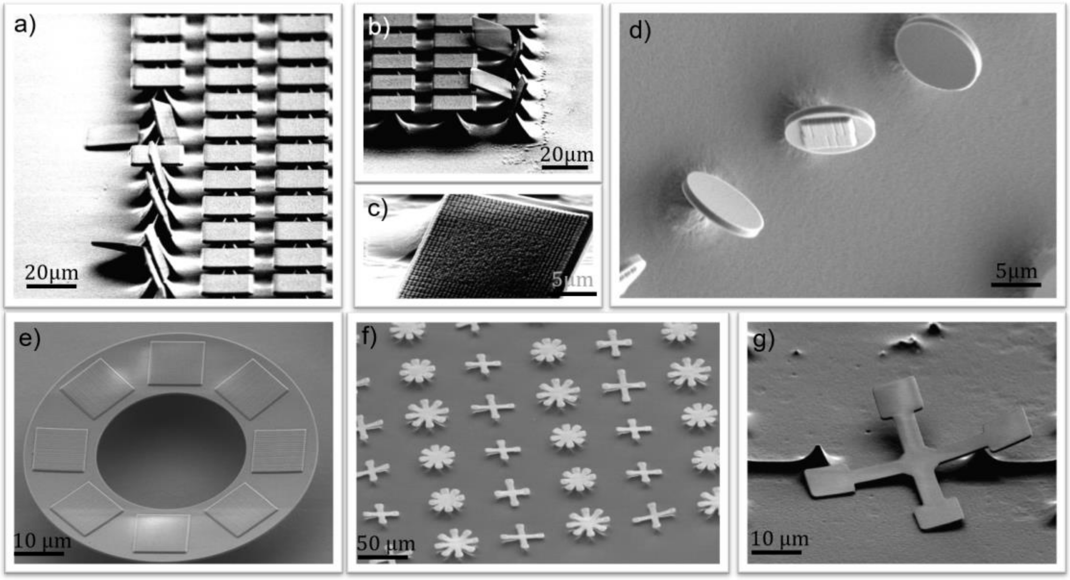

Figure 5.11: (a)-(c) Metaparticles featuring deflectors at the edges and a metalens at the center. (d) Rotor with embedded gratings and a circular body. (e) Donut-shaped rotor equipped with gratings (100 μm in diameter). (f) Cross-shaped rotor. (g) Passively cross-shaped SiO$_2$ structure without gratings.

All metaparticles shown in Figure 5.11, as well as those described in **Papers II** and **III**, were coated with SiO_2 to protect the grating during the final detachment step. However, fabricating metaparticles with bare metaatoms required additional considerations.

The following part outlines a new fabrication process for metaparticles without covering silicon metasurfaces. For example, this can be important for making free immersion metalenses with bare silicon to minimize additional interfaces, such as the SiO_2 protective layer. To do that, a proper masking material was required to replace SiO_2, which could be easily removed after the detachment of metaparticles. For this purpose, aluminum was chosen as the mask layer due to its compatibility with standard etching processes. However, the use of aluminum introduced challenges, as aluminum is highly reactive with most developers, particularly basic developers like MF CD-26, which could result in undesirable etching during fabrication procedures. To solve this, a sacrificial layer of PMMA was applied over the aluminum to protect it from reacting with the MF CD-26 during the development of LOR 3A and S1805 resists after the second layer exposure process. This protective PMMA layer allowed for the development and processing of the structure without affecting the aluminum mask. Once the lenses were fully realized, the aluminum mask was successfully removed by immersing the metalenses in an aluminum etchant, which dissolved the aluminum without impacting on the structural integrity of the silicon lenses, as illustrated in step 30 of Figure 5.12. Figure 5.12 details the fabrication steps used to produce the free immersion metalenses without additional protective layers.

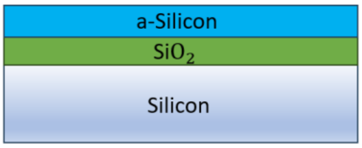

1. Growth of oxidized 400 nm SiO$_2$
2. LPCVD 490 nm a-Silicon

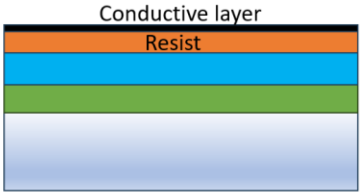

3. Coating AR-P 6200.13 1:1, 150 nm
4. Thermal Evaporation 25 nm Cr

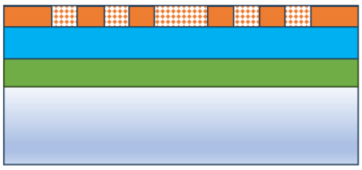

5. EBL exposure, Dose 310 µC/cm^2
6. Cr wet etching

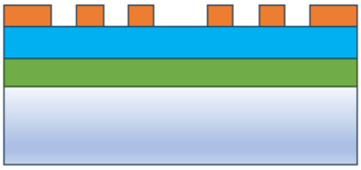

7. Development, Amyl acetate, 90 s
8. O$_2$plasma ash, 40 W, 10 s

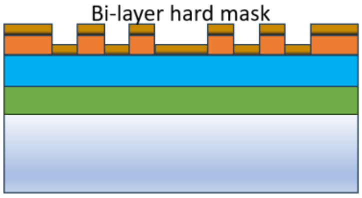

9. Hard mask evaporation, 5 nm Cr
10. Hard mask evaporation, 55 nm Ni

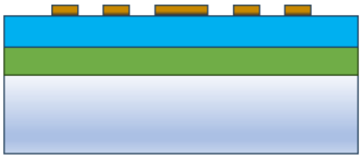

11. Lift off - Remover 1165 @ 80 °C
12. O$_2$plasma ash, 50 W, 30 s

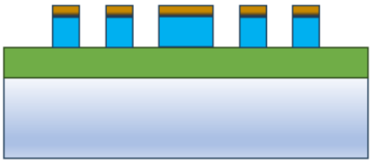

13. Si Dry etch ICP with Cl$_2$ & HBr
14. O$_2$ plasma ash, 50 W, 30 s

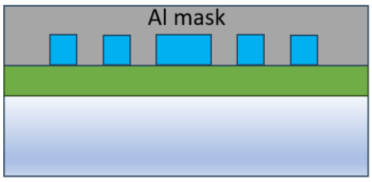

15. Cr and Ni wet etch
16. Sputtering Al, 610 nm

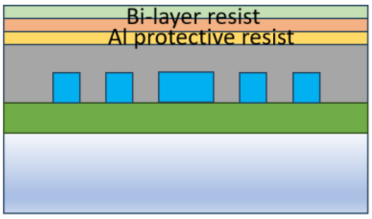

17. Coating PMMA A2, 100 nm
18. Coting photoresist LOR 3A & S1805

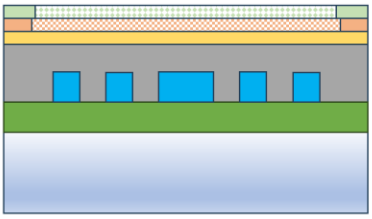

19. Laser writing photolithography
20. Development, MF CD-26

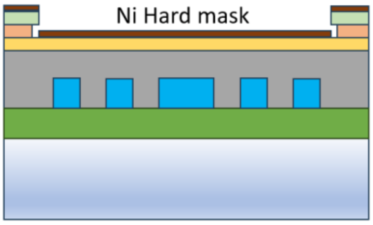

21. O$_2$ plasma ash, 40 W, 10 s
22. Hard mask evaporation, 60 nm Ni

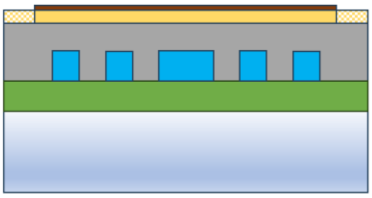

23. Lift off - Remover 1165
24. O$_2$ plasma ash, 50 W, 5 min

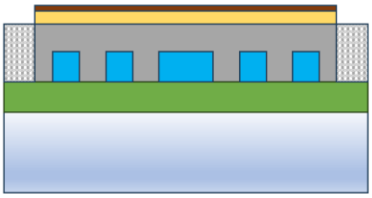

25. Al wet etch at 40 °C

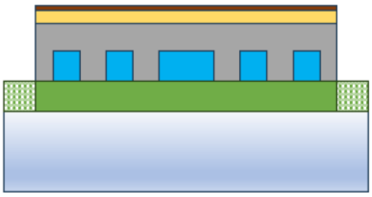

26. SiO$_2$ dry etch ICP with CHF$_3$

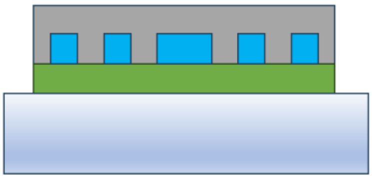

27. Ni wet etch
28. O$_2$ and Piranha etch

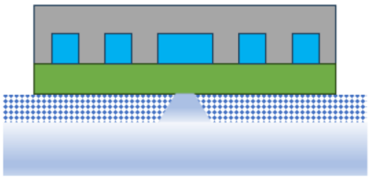

29. Si ICP etch SF$_6$

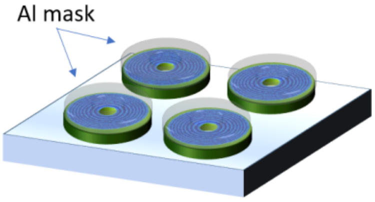

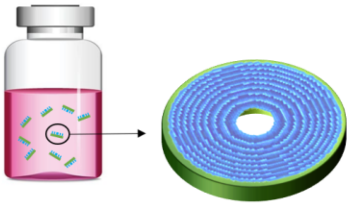

30. Al wet etch

Figure 5.12: Fabrication process flow of an immersion metalens (Shanei, et al., unpublished data). Growth of 400 nm oxidized SiO2 (step 1) and deposition of 490 nm a-Si on the Si wafer (step 2). Ellipsometry characterization of the resulting a-Si layer gave a complex refractive index of n a-Si = 3.82 + i0.0061. Spin coating of e-resist (ARP6200.13) onto the a-Si. The resist is baked at 160°C (step 3). Evaporation of Cr (an alternative could be spin coating a conductive polymer) to prevent charge accumulation during exposure (step 4). Electron beam exposure at 310 µC/cm2 (10 nA) (step 5), and wet etching of 25 nm Cr (step 6). Development of resist by Amyl acetate for 90 sec (step 7). An O2 ashig to remove residual of exposed resist. This step provides a sharper profile (step 8). To facilitate further structural definition, a hard mask of 3 nm Cr (step 9) and 55 nm Ni (step 10) are deposited on the resist followed by lift off with Microposit Remover 1165 at 80 °C (step 11) and another O2 plasma etching (step 12). The metalens patterns are then transferred to the a-Si layer through Cl2 reactive ion etching step (50 SCCM Cl2 at 10 mTorr and 45/90 W of power on the inductively coupled plasma (ICW) and the forward power (FW) electrodes, respectively. An additional HBr ICP etching can be done to make a more vertical sidewall for cylinders after the Cl_2 step (step 13) and a An O_2 ashig (step 14). The remaining hard mask is then removed through Ni etchant for around 30 min (step 15). Sputtering 610nm Al (step 16) and spin coating 100 nm PMMA resist as the protection layer (step 17). Spin coating double layers photo resist (step 18) and photolithography to make the body of metalens (step 19). Development of resist for 55 sec (step 20). Ashing (step 21) and the evaporation of Ni. Due to the existence of PMMA, there is no need to have a Cr in this step (step 22). Lifting off (step 23) and a 5 min ashing to remove the uncover parts of PMMA to open an aperture to Al (step 24). Wet etching of Al at 40 ℃ to reach to the SiO_2 (step 25) followed by CHF_3 ICP etching of SiO_2 to open a gate toward the Si wafer (step 26). Cleaning the residual of mask (step 27) cleaning the sample (step 28). Anisotropic ICP etch to etch Si and dig under the SiO_2 and releasing of the metalenses (step 29). Removing the protective Al layer (step 30), (Shanei, et al., unpublished data).

5.3. Optical characterization

Measurements of polarization conversion efficiency:

Efficiency is an important merit to consider in phase gradient metasurfaces as a competitor with bulky optical elements. In the PB metasurfaces that act as a half-waveplate, one-handedness of the polarization switches to the other and acquires the required phase shifts. Therefore, the ability of each unit cell to convert the handedness of the incident light is defined as polarization conversion efficiency (PCE). To experimentally measure the PCE of a metasurface, a periodic array of metaatoms oriented at 45° was placed between two crossed linear polarizers. This measurement is identical to sending an RCP (LCP) and monitoring LCP (RCP) after PB patterns. For example, Figure 5.13 (a) shows differences in efficiency for visible light in PB patterns with different lengths, fixed widths, and periodicities. Figure 5.14 (b) focuses on the IR regimes plotting the measured transmittance spectra a PB pattern for the co and cross of the light beam. The transmittance is calculated by measurements of I_{co} and I_{cross}, which are the intensities of the transmitted beam from the metasurface for the same and orthogonal polarization states before and after the metasurface. Figure 5.13 (c) demonstrates the optical setup used to measure the PCE. These measurements are used to find the optimized metaatom in **Paper I**.

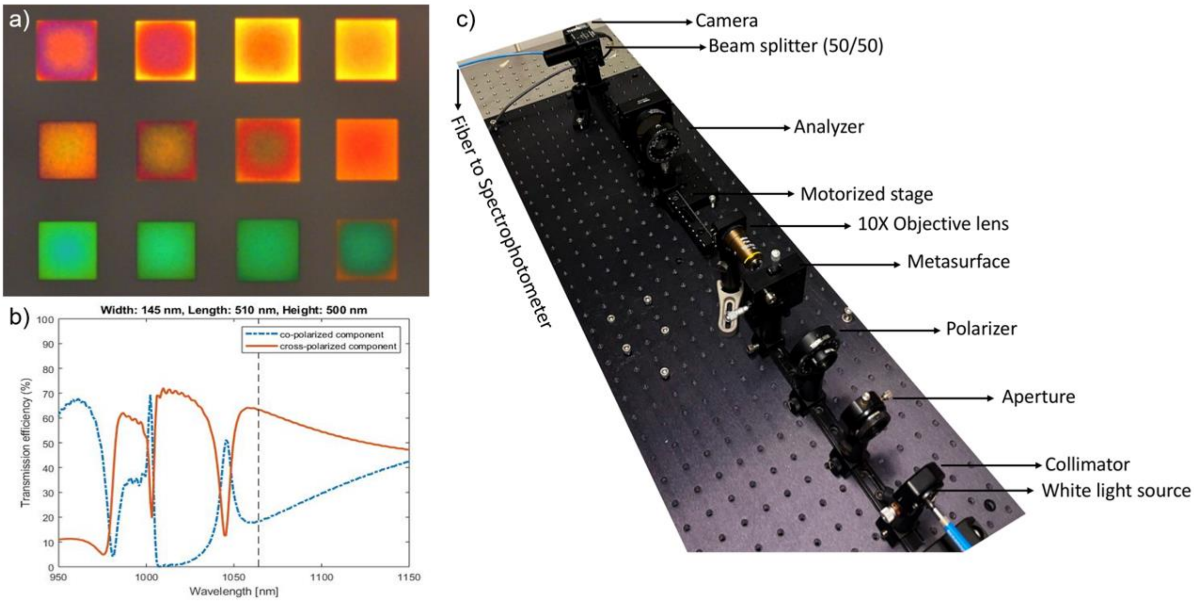

Figure 5.13: (a) Intensity contrast image taken by considering orthogonal polarizations for white light before and after PB patterns. (b) Co and Cross polarized efficiency for a PB pattern measured with (c) an optical setup used for the polarization conversion efficiency measurements.

Fourier microscopy:

Fourier microscopy is a powerful technique used to analyze the angular distribution of light, allowing for the extraction of diffraction efficiency of gratings. In this method, the objective lens of the microscope captures light scattered or transmitted through the grating and projects it onto the back focal plane, which corresponds to the Fourier plane. Here, the spatial distribution of the light intensity directly maps to the different diffraction angles. By imaging this Fourier plane, one can measure the intensity of light in each diffraction order, enabling the calculation of diffraction efficiency. The optical setup used to measure the efficiencies of transmitted diffracted orders is shown in **Paper II**.

Optical setup for particle trapping by free immersion metalens:

The optical setup used for trapping two-dimensional trapping of 1-µm PS beads (microParticles GmbH) is shown in Figure 5.14. The light impinges on the sample from the bottom. The particles and metalens are sedimented after a while due to gravity.

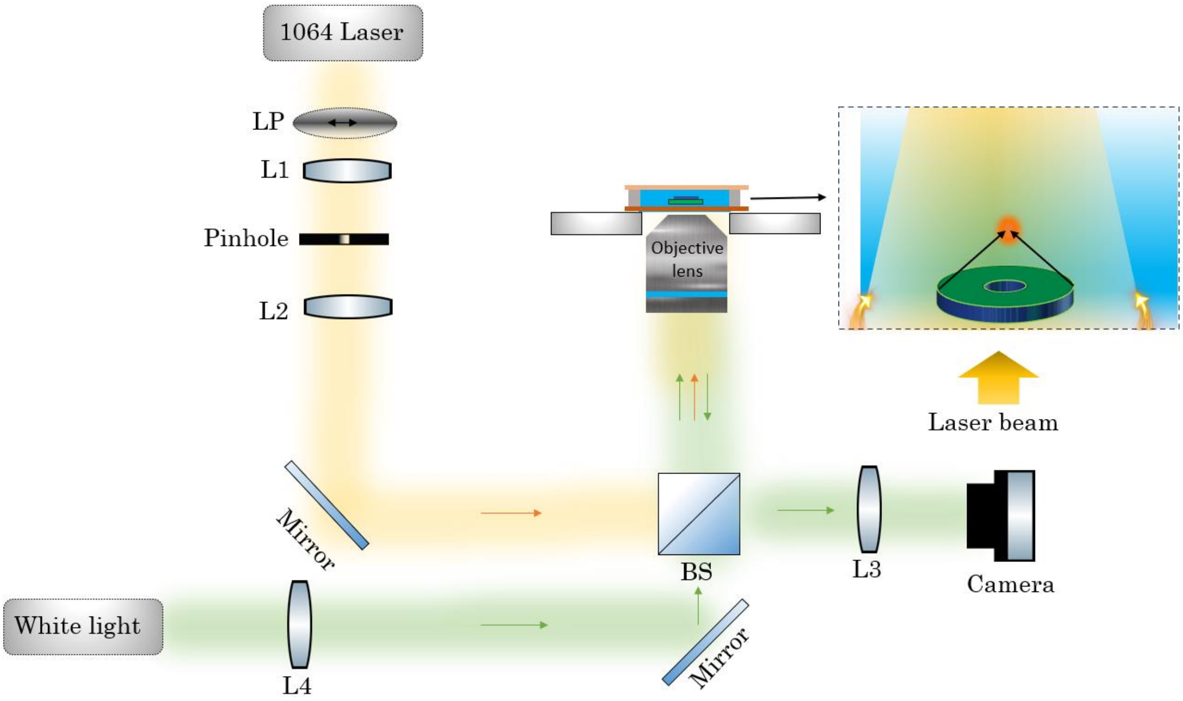

Figure 5.14: Optical setup for conducting trapping with free immersion metalens experiments. A linearly polarized 1064-nm laser with a diameter of 1 mm is employed and directed toward the bottom of the sample lens. The beam is collimated and de-magnified by L1 and L2. The transmitted beam is then focused onto the sample chamber through an objective lens. The sample and trapping beads are observed in reflection mode, illuminated by white light.

Optical setup for driving metarotors:

The optical setup used rotating rotors at two sides of the chamber is illustrated in Figure 5.15. This setup is designed for a counterpropagating beam impinging on the chamber from the bottom and above.

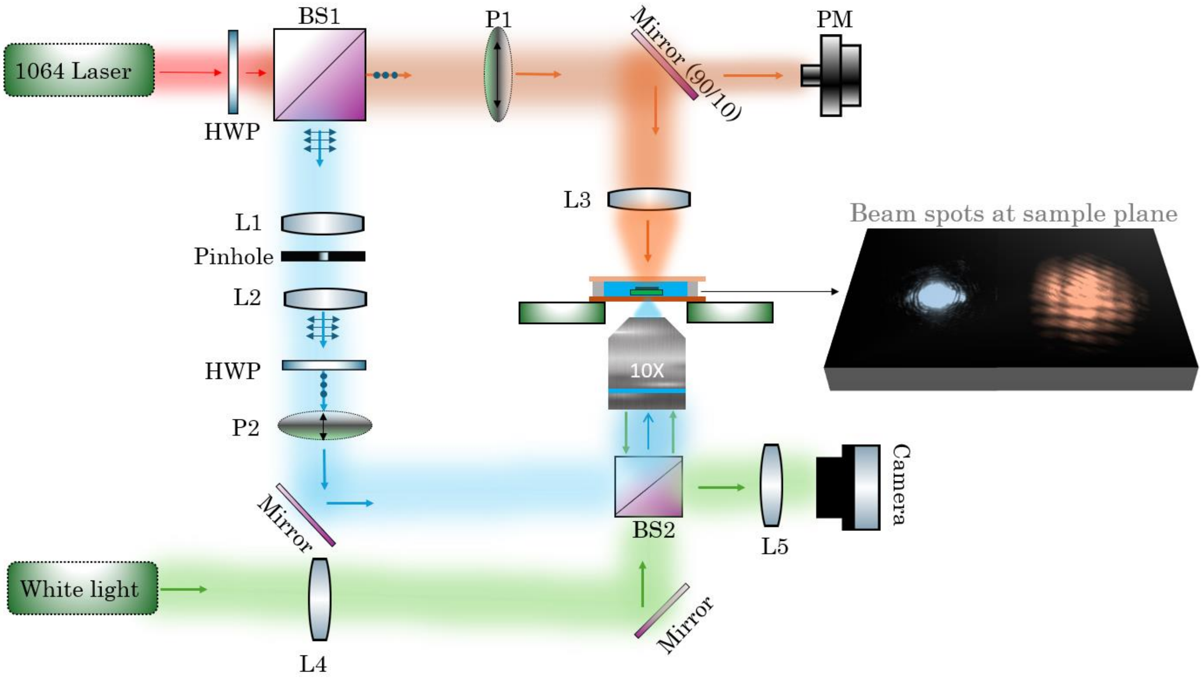

Figure 5.15: Optical setup for conducting optical rotation experiments at the bottom and top side of the chamber. A linearly polarized 1064 nm laser is divided through a polarization-sensitive beam splitter. The ratio of the power of the laser beam is controlled by an HWP. The beam size from the bottom and above are 60 µm and 90 µm, respectively. The white illumination light is also directed from the bottom of the sample and the rotation of rotors is captured in reflection mode by a CCD camera.

Chapter 6

Concluding remarks

Looking back, my PhD journey wasn’t a straightforward line. While some may follow a clear, narrow path, mine was shaped by a series of interconnected experiences that contributed to my growth and understanding of the subject. Each step had meaning, and collectively, they enriched my knowledge. One of the most fulfilling aspects of my work was the time spent in the cleanroom, engaging in nanofabrication. I enjoyed the hands-on challenge of optimizing the fabrication processes for metasurfaces, gratings, and other structures. However, my interest didn’t stop there. Running numerical simulations to design structures, model outcomes, and predict their behavior was equally fascinating. Additionally, performing optical measurements and characterizing the fabricated structures added further complexity to my work. This combination of fabrication, experimentation, and numerical simulation kept my research dynamic and engaging. Each aspect brought new challenges and opportunities for learning.

This thesis reflected the journey, challenges, and discoveries I encountered during my PhD. It began with a brief introduction to flat optics in **Chapter 2**. In this chapter, the fundamental principles of metasurfaces were discussed, and they were categorized based on various factors such as working wavelength, material composition, design methodologies, and more. Additionally, some examples of fabricated metasurfaces were presented to demonstrate their potential for beam shaping.

Chapter 3 was dedicated to exploring the optical forces and torques arising from the transfer of linear and angular momentum of light. It began with an overview of the optical forces and torques that a beam of light could generate, illustrating how metagratings produced reaction forces and alignment torques. Following this, I studied the dynamic interactions of metagrating-based swimmers operating in a low Reynolds number regime.

Chapter 4 focused on how metasurfaces assisted in the optical manipulation of objects. It started with a brief overview of various actuation mechanisms for manipulating micro and nano objects and proceeded to provide examples of optical manipulation using passive and active metasurfaces.

Finally, **Chapter 5** provided an overview of the research methodologies employed in the thesis. It detailed the numerical simulation techniques used and described the experimental optical setups that were essential for characterizing the fabricated samples.

Paper I

Light-driven transport of microparticles with phase-gradient metasurfaces

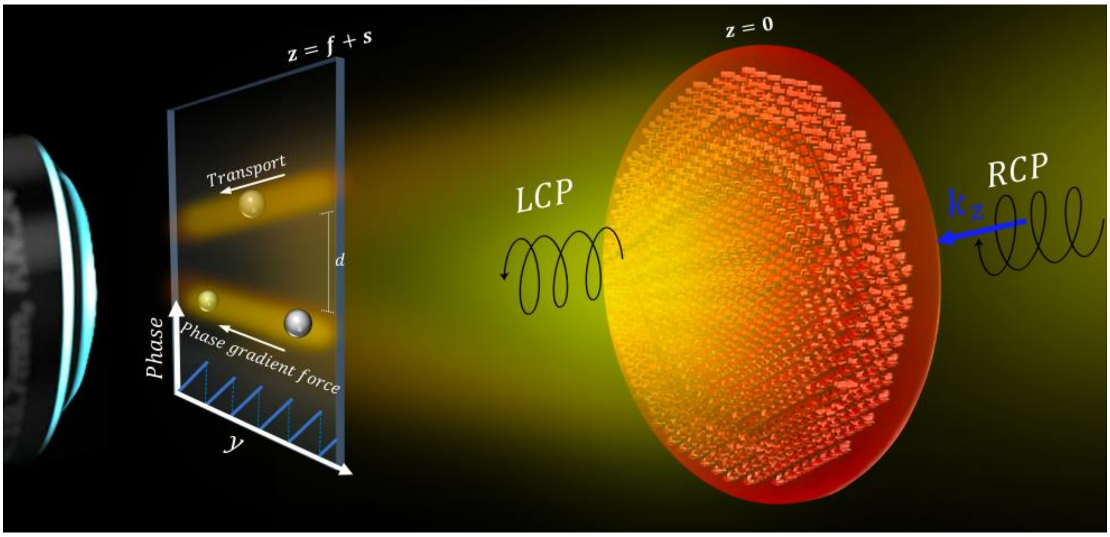

Figure 6.1: Transport of particles in two lines.

In this paper, an ultrathin cylindrical metasurface is designed and fabricated to trap and push particles along its focal line. The required phase profile was experimentally realized using arrays of nanofins with locally varying rotation angles (PB method). The metasurface is optimized to work at λ=1064 and with amorphous silicon (a-Si) building blocks arranged in a square lattice on a glass substrate. As discussed in **Chapter 3**, the confinement achieved through the intensity gradient in the transverse plane pointed to the focal line. So, the particles outside the focal area move laterally toward the trapping line. Then, the trapped particles move in the expected direction due to the phase gradient but with a discontinuation motion due to the existence of the intensity hot spots in the focal line. We found that the beam deflector phase gradient adds unwanted intensity fluctuations that tend to lock particles to specific positions. To decrease the influence of the intensity hotspots, the target plane was located in the defocusing plane of the metalens. Due to diffraction effects, a relatively smooth intensity distribution has been observed in the translation of the particles.

Paper II

Transverse optical gradient force in untethered rotating metaspinners

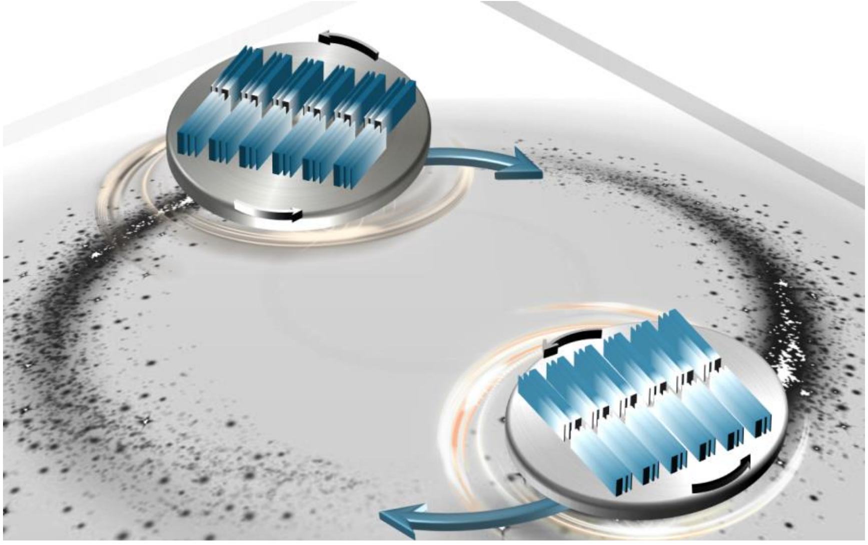

Figure 6.2: CCW Spinning and CW orbiting of metaspinners.

This work presents a novel design strategy for optically controlled swimmers, referred to as *metaspinners*. The design relies on metagratings arranged in such a way that the optical reaction forces generated by changes in the linear momentum of light produce an optical torque, causing the metaspinners to rotate. The paper explores how the rotational motion of the metaspinners can be controlled by the spin component of the incident light, how the photothermal effects can influence the rotation frequency and moreover, how nonslip boundary conditions between the spinner and chamber can limit the surrounding fluidic flows.

The key finding is that when a metaspinner spins off-center from the light beam, it experiences a tangential optical force. As a result, when several metaspinners gather within a laser beam, they not only spin around their own axes but also collectively move together in a circular path. In this scenario, the tangential force is stronger than the hydrodynamic interaction forces, leading pairs or groups of co-rotating metaspinners to have orbital motion that opposes their spinning direction. This behavior is different from anything seen in previous studies of similar systems.

This observation led to the conceptualization of a new type of effective optical gradient force that acts perpendicular to the classical optical gradient force, with its sign determined by the handedness of the metaspinner particle. The unique interplay between spinning and orbital motions in metaspinners opens up exciting possibilities for developing new types of optomechanical systems. Moreover, the concept of metaspinners could have significant applications in the study of fundamental physical phenomena, providing a novel platform for investigating light-matter interactions at small scales.

Paper III

Harnessing photon recoil for enhanced torque on light-driven

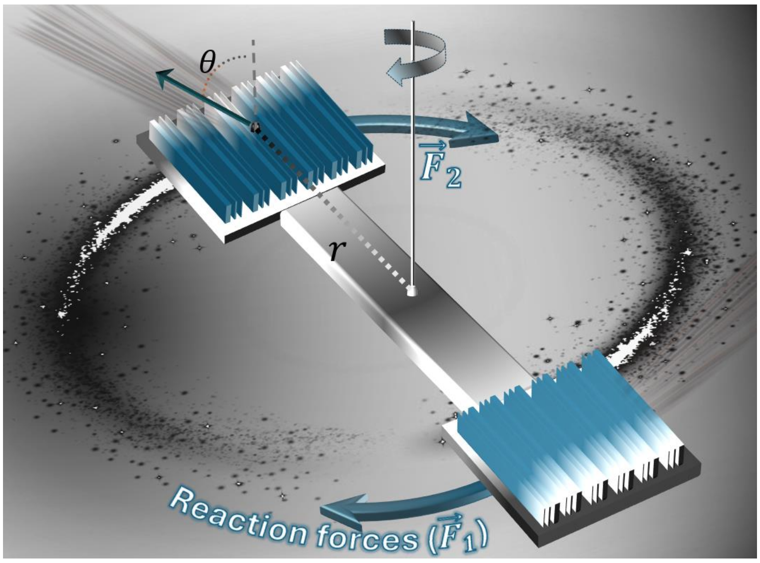

Figure 6.3: Rotor with a single arm.

This paper demonstrates a controllable and steady rotation of cross-shaped metarotor and an application of them in rotating tens of microscopic objects. In this work, the effectiveness of deflective metagratings has been studied in the creation of optical torques. To harness reaction forces into optical torque, we engineered cross-shaped structures with varying numbers of arms, each equipped with metagratings at their arm tips. This design circumvents fabrication constraints associated with rotor detachment. In our analysis of rotor rotational dynamics, a nonlinear region is identified at the higher incident light power. The paper shows that this nonlinearity arises from changes in viscosity, induced by the photothermal heating of gratings at higher intensities.

This work also evaluates the mechanical capabilities of the rotors by implementing computational fluid dynamics simulations. These simulations indicate that the fluidic velocity decays within a few micrometers in both radial and z-directions. Furthermore, the experiments show that these rotors can rotate clusters of a few hundred beads with a size of 7 µm while retaining 80% of their initial velocity. The experiments in this paper demonstrate the remarkable mechanical power transferability of these metarotor, suggesting promising applications in microfluidic channels such as mixers, pumps, and gates.

Outlook

The future of optical manipulation and optical tweezers is set for remarkable advancements, with applications spanning from biomedical research to quantum computing. As technology evolves, we can expect enhanced precision in manipulating nanoparticles, cells, and even individual molecules, leading to breakthroughs in drug delivery, nanomaterials, and the assembly of quantum systems. The integration of metasurfaces, which can shape and control light in unprecedented ways, will enable more versatile and compact optical tweezers, allowing for multiple particle manipulation, higher resolution, and on-chip integration.

The arrival of optically flat structures, which can precisely control light at the nanoscale, will significantly enhance the capabilities of optical tweezers. These structures will allow for more versatile beam shaping, higher resolution, and multiple particle manipulation similar to what we introduce in **Paper I**. While the integration of metasurfaces into optical tweezer technology represents a significant jump forward, it is still in its early stages, with immense potential for further development. Current applications of metasurfaces in optical manipulation are just beginning to demonstrate their capabilities, such as enhanced beam shaping and improved trapping efficiency. This ongoing development will likely unlock new applications and dramatically expand the possibilities for optical tweezers in scientific research and industry.

Optical tweezer technology has been instrumental in studying the behavior of active particles, providing a means to control their movement and interactions in a highly controlled environment. The study of microscopic particles suspended in liquids has had a profound impact on science and engineering. A hundred years ago, experiments observing their random motion helped prove the existence of atoms. In the 20th century, research focused on how these systems behave when in thermal equilibrium with their environment. However, recent studies on self-propelling particles, which operate out of equilibrium with external stimuli, have opened up new possibilities. These active particles can move in directed ways, adapt to their surroundings, and form complex group behaviors, similar to how living microorganisms do. For example, Janus microspheres or microrods, despite their simplicity, have already led to breakthroughs, such as understanding plankton behavior, creating self-assembling robotic swarms, and improving drug delivery systems. To push the boundaries of this research even further, we need to develop smart, programmable swimmers capable of gathering and processing information from their surroundings. The advent of miniaturized metasurfaces could mark a revolutionary step in this direction. These engineered structures hold the potential to not only enhance the capabilities of microscopic particles but also to unveil new types of forces and interactions, as demonstrated in our **Paper II**. Further developments in this field could lead to entirely new systems, driving significant progress in fields ranging from material science to biomedical engineering. Moreover, in a preliminary study, we observed that a metavehicle could interact with the bottom of the cover glass by changing the chemical properties of the surface. In this experiment, we have deposited 5 nm chromium which is less than the nominal roughness of a cover glass. Figure 6.4 shows a metavehicle can detour from its straight path and follow the deposited Cr. This preliminary result shows that there is more room to study this kind of surface interaction to make a smart swimmer that can also scan and sense the environment.

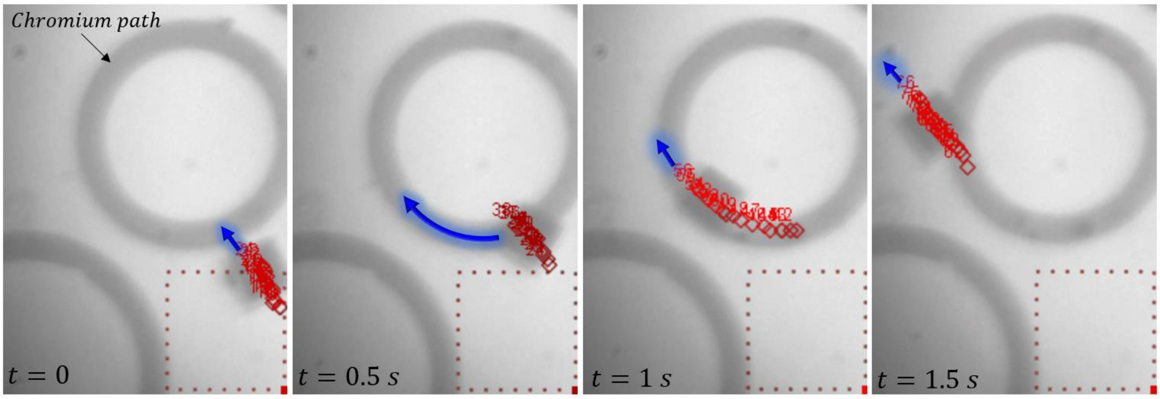

Figure 6.4: Surface interaction of a metavehicle with 5 nm evaporated chromium.

Research on particle manipulation spans a wide range of scales. Numerous studies have demonstrated the manipulation of millimeter-sized and larger particles using techniques such as magnetic actuation. Similarly, extensive work has been done on manipulating particles in the 100 nm to 10 μm range using optical tweezers. However, the manipulation of particles in the tens of micrometers range remains relatively underexplored, largely due to challenges caused by gravity and viscous drag forces in low Reynolds number regimes. In **Paper III** we tried to push this limit and unlock a new application of metasurfaces in creation of unprecedented optical torque from a light source. This rotating object can function as an intermediate tweezer, transferring contactless mechanical power to secondary objects. One improvement that can be implemented is moving toward three-dimensional trapping which can give more degrees of freedom to metagratings-based particles in swimming and moving around.

Another area of exploration is the precise control of rotational placement along the z-axis. However, as shown in **Chapter 4**, counterpropagating beams can cause the rotors to rotate at both the top and bottom sides of the chamber. Achieving three-dimensional stable beam-riding remains a challenge that requires further investigation. One potential approach involves incorporating a curved design, as suggested in [178]. Supporting this approach, our observations during the fabrication process of the metarotors revealed that the SiO_2 arms can be deliberately bent. This bending is achieved by controlling the stress applied to the SiO_2 during its detachment from the Si wafer using SF_6 gas, as illustrated in Figure 6.5. This finding opens new possibilities for investigating beam-riding stability in these rotors.

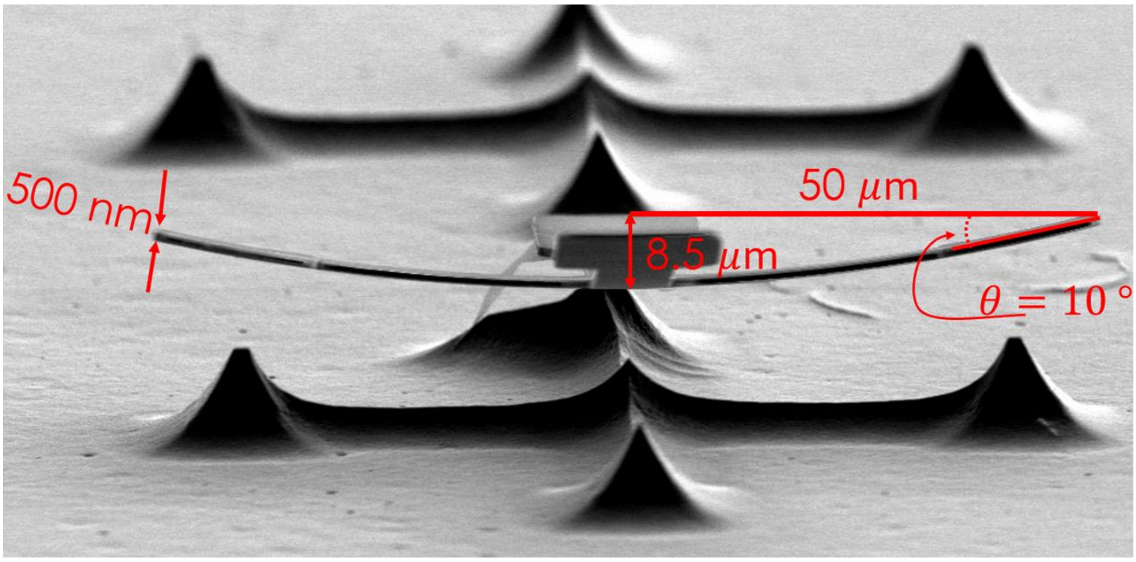

Figure 6.5: A curved passive rotor is suggested for adding structural stability for beam-riding. The curvature can be adjusted by controlling the ratio of detachment times between the central and outer parts of the rotor. This can be further controlled by adjusting the width of the SiO_2 layer at the center relative to the tips of the rotor.

Finally, as a next step, it would be valuable to explore the potential of these elements as a functional platform. For example, Figure 6.6 illustrates optical images of a translating metalens driven by surrounding beam deflectors. Further research could investigate how precise control of reaction forces enables accurate positioning of the metalens, paving the way for innovative applications in advanced optical manipulation.

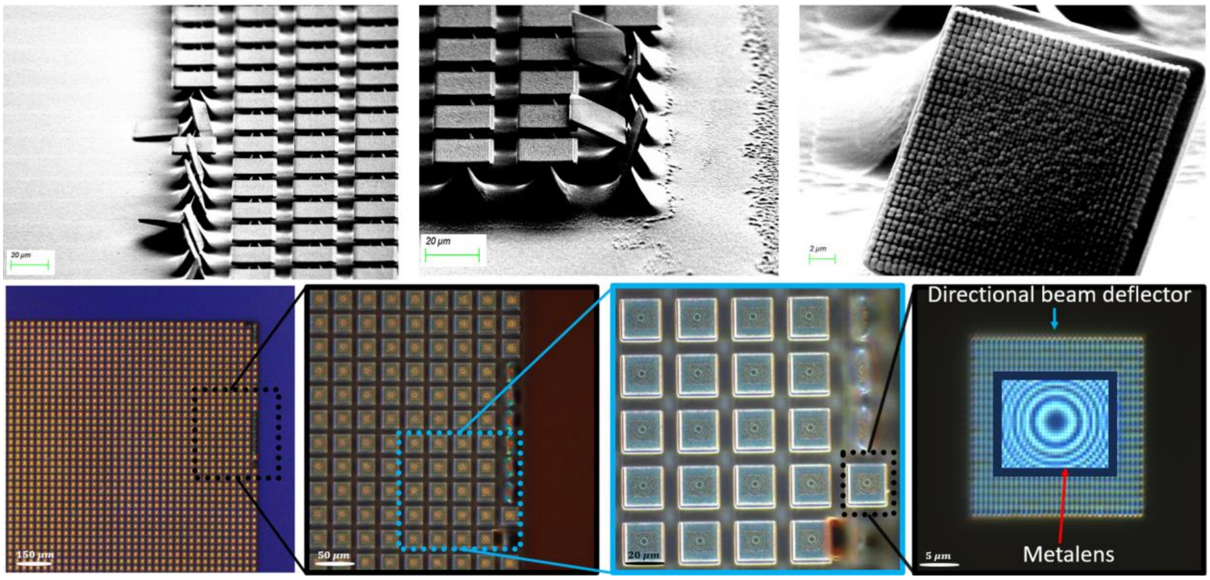

Figure 6.6: Bifunctional metaparticles. SEM and optical images of fabricated metalenses at center and beam deflectors at edges to provide reaction force to move the metalens.

Bibliography

1. P. Vukusic, et al., "Colour mixing in wing scales of a butterfly," *Nature* **404**, 457-457 (2000).
2. P. Vukusic and J. R. Sambles, "Photonic structures in biology," *Nature* **424**, 852-855 (2003).
3. R. A. Potyrailo, et al., "Towards outperforming conventional sensor arrays with fabricated individual photonic vapour sensors inspired by Morpho butterflies," *Nature Communications* **6**, 7959 (2015).
4. D. R. Smith, et al., "Metamaterials and negative refractive index," *Science* **305**, 788-792 (2004).
5. P. Huo, et al., "Hyperbolic metamaterials and metasurfaces: fundamentals and applications," *Advanced Optical Materials* **7**, 1801616 (2019).
6. G. Yoon, et al., "Challenges in fabrication towards realization of practical metamaterials," *Microelectronic Engineering* **163**, 7-20 (2016).
7. N. Li, et al., "Large-area metasurface on CMOS-compatible fabrication platform: driving flat optics from lab to fab," *Nanophotonics* **9**, 3071-3087 (2020).
8. Y. Dong, et al., "Si metasurface half-wave plates demonstrated on a 12-inch CMOS platform," *Nanophotonics* **9**, 149-157 (2020).
9. N. Yu, et al., "Light propagation with phase discontinuities: generalized laws of reflection and refraction," *Science* **334**, 333-337 (2011).
10. A. Ashkin and J. Dziedzic, "Optical levitation in high vacuum," *Appl Phys Lett* **28**, 333-335 (1976).
11. M. J. Padgett, et al., *Optical Tweezers: methods and applications* (CRC press, 2010).
12. P. Jones, et al., *Optical tweezers* (Cambridge University Press Cambridge, 2015).
13. G. Volpe, et al., "Roadmap for optical tweezers," *Journal of Physics: Photonics* **5**, 022501 (2023).
14. E. M. Purcell, "Life at low Reynolds number," in *Physics and our world: reissue of the proceedings of a symposium in honor of Victor F Weisskopf*, (World Scientific, 2014).

15. S. Banerji, et al., "Imaging with flat optics: metalenses or diffractive lenses?," *Optica* **6**, 805-810 (2019).
16. P. Genevet, et al., "Recent advances in planar optics: from plasmonic to dielectric metasurfaces," *Optica* **4**, 139-152 (2017).
17. J. Hu, et al., "A review on metasurface: from principle to smart metadevices," *Frontiers in Physics* **8**, 586087 (2021).
18. Y. He, et al., "Optical metalenses: fundamentals, dispersion manipulation, and applications," *Frontiers of Optoelectronics* **15**, 24 (2022).
19. C. L. Holloway, et al., "An overview of the theory and applications of metasurfaces: The two-dimensional equivalents of metamaterials," *IEEE Antennas and Propagation Magazine* **54**, 10-35 (2012).
20. W.-L. Hsu, et al., "Review of metasurfaces and metadevices: advantages of different materials and fabrications," *Nanomaterials* **12**, 1973 (2022).
21. S. Alkunte, et al., "Functionally Graded Metamaterials: Fabrication Techniques, Modeling, and Applications—A Review," *Processes* **12**, 2252 (2024).
22. V.-C. Su, et al., "Advances in optical metasurfaces: fabrication and applications," *Optics express* **26**, 13148-13182 (2018).
23. J. Rho, "Metasurfaces: Subwavelength nanostructure arrays for ultrathin flat optics and photonics," *MRS Bulletin* **45**, 180-187 (2020).
24. L. Huang, et al., "Metasurface holography: from fundamentals to applications," *Nanophotonics* **7**, 1169-1190 (2018).
25. K. Achouri and C. Caloz, *Electromagnetic metasurfaces: Theory and applications* (John Wiley & Sons, 2021).
26. S. M. Kamali, et al., "A review of dielectric optical metasurfaces for wavefront control," *Nanophotonics* **7**, 1041-1068 (2018).
27. A. C. Overvig, et al., "Dielectric metasurfaces for complete and independent control of the optical amplitude and phase," *Light: Science & Applications* **8**, 92 (2019).
28. A. Arbabi, et al., "Dielectric metasurfaces for complete control of phase and polarization with subwavelength spatial resolution and high transmission," *Nature Nanotechnology* **10**, 937-943 (2015).
29. E. Schonbrun, et al., "Reconfigurable imaging systems using elliptical nanowires," *Nano Letter* **11**, 4299-4303 (2011).
30. S. Sun, et al., "High-efficiency broadband anomalous reflection by gradient meta-surfaces," *Nano Letter* **12**, 6223-6229 (2012).

31. M. Khorasaninejad, et al., "Polarization-insensitive metalenses at visible wavelengths," *Nano Letter* **16**, 7229-7234 (2016).

32. Y. Cheng, et al., "Ultra-sparse metasurface for high reflection of low-frequency sound based on artificial Mie resonances," *Nature Materials* **14**, 1013-1019 (2015).

33. V. E. Babicheva and A. B. Evlyukhin, "Mie-resonant metaphotonics," *Advances in Optics and Photonics* **16**, 539-658 (2024).

34. M. Decker, et al., "High-efficiency dielectric Huygens' surfaces," *Advanced Optical Materials* **3**, 813-820 (2015).

35. S. Pancharatnam, "Generalized theory of interference and its applications: Part II. Partially coherent pencils," in *Proceedings of the Indian Academy of Sciences-section a*, (Springer, 1956), 398-417.

36. J. C. Gutiérrez-Vega, "Pancharatnam–Berry phase of optical systems," *Optics Letters* **36**, 1143-1145 (2011).

37. D. Lin, et al., "Dielectric gradient metasurface optical elements," *Science* **345**, 298-302 (2014).

38. G. V. Naik, et al., "Alternative plasmonic materials: beyond gold and silver," *Advanced materials* **25**, 3264-3294 (2013).

39. S. Sun, et al., "Gradient-index meta-surfaces as a bridge linking propagating waves and surface waves," *Nature Materials* **11**, 426-431 (2012).

40. W. Cao, et al., "Broadband polarization conversion with anisotropic plasmonic metasurfaces," *Scientific Reports* **7**, 8841 (2017).

41. N. Segal, et al., "Controlling light with metamaterial-based nonlinear photonic crystals," *Natature Photonics* **9**, 180-184 (2015).

42. A. Hassanfiroozi, et al., "A Toroidal-Fano-Resonant metasurface with optimal cross-polarization efficiency and switchable nonlinearity in the Near-Infrared," *Advanced Optical Materials* **9**, 2101007 (2021).

43. Z. Xu, et al., "CMOS-compatible all-Si metasurface polarizing bandpass filters on 12-inch wafers," *Optics Express* **27**, 26060-26069 (2019).

44. C. Zheng, et al., "All-silicon chiral metasurfaces and wavefront shaping assisted by interference," *Science China: Physics, Mechanics and Astronomy* **64**, 114212 (2021).

45. J. Li, et al., "All-silicon metasurfaces for polarization multiplexed generation of terahertz photonic orbital angular momentum superposition states," *Journal of Materials Chemistry C* **9**, 5478-5485 (2021).

46. I. O. Oguntoye, et al., "Silicon nanodisk Huygens metasurfaces for portable and low-cost refractive index and biomarker sensing," *ACS Applied Nano Materials* **5**, 3983-3991 (2022).

47. Y. Wu, et al., "TiO2 metasurfaces: From visible planar photonics to photochemistry," *Science advances* **5**, eaax0939 (2019).

48. Q. Zhou, et al., "Generation of Perfect Vortex Beams by Dielectric Geometric Metasurface for Visible Light," *Laser & Photonics Reviews* **15**, 2100390 (2021).

49. V. J. Einck, et al., "Scalable nanoimprint lithography process for manufacturing visible metasurfaces composed of high aspect ratio TiO2 meta-atoms," *ACS Photonics* **8**, 2400-2409 (2021).

50. J. Kim, et al., "Metasurface holography reaching the highest efficiency limit in the visible via one-step nanoparticle-embedded-resin printing," *Laser & Photonics Reviews* **16**, 2200098 (2022).

51. B. H. Chen, et al., "GaN metalens for pixel-level full-color routing at visible light," *Nano Letter* **17**, 6345-6352 (2017).

52. Z. Guo, et al., "High-efficiency visible transmitting polarizations devices based on the GaN metasurface," *Nanomaterials* **8**, 333 (2018).

53. M.-H. Chen, et al., "Polarization-insensitive GaN metalenses at visible wavelengths," *Scientific Reports* **11**, 14541 (2021).

54. C.-S. Park, et al., "Structural color filters based on an all-dielectric metasurface exploiting silicon-rich silicon nitride nanodisks," *Optics Express* **27**, 667-679 (2019).

55. S. Colburn, et al., "Broadband transparent and CMOS-compatible flat optics with silicon nitride metasurfaces," *Optical Materials Express* **8**, 2330-2344 (2018).

56. J.-H. Yang, et al., "Structural colors enabled by lattice resonance on silicon nitride metasurfaces," *ACS Nano* **14**, 5678-5685 (2020).

57. M. Juodėnas, et al., "High-angle deflection of metagrating-integrated laser emission for high-contrast microscopy," *Light: Science & Applications* **12**, 251 (2023).

58. N. Shitrit, "Surface-emitting lasers meet metasurfaces," *Light: Science & Applications* **13**, 37 (2024).

59. R. Gao, et al., "Optical characterization of silicon nitride metagrating-based lightsails for self-stabilization," *ACS Photonics* **9**, 1965-1972 (2022).

60. X. Shi, et al., "Metasurface inverse design using machine learning approaches," *Journal of Physics D: Applied Physics* **53**, 275105 (2020).

61. Z. Li, et al., "Empowering metasurfaces with inverse design: principles and applications," *ACS Photonics* **9**, 2178-2192 (2022).

62. Y. Li, et al., "Multifunctional Metasurface Inverse Design Based on Ultra-Wideband Spectrum Prediction Neural Network," *Advanced Optical Materials* **12**, 2302657 (2024).

63. R. E. Christiansen and O. Sigmund, "Inverse design in photonics by topology optimization: tutorial," *Journal of the Optical Society of America B* **38**, 496-509 (2021).

64. S. Chen, et al., "Metasurface-empowered optical multiplexing and multifunction," *Advanced Materials* **32**, 1805912 (2020).

65. Z. Zhang, et al., "Manipulations of vectorial-structured light by spatially interleaved metasurfaces of quarter-wave-plate meta-atoms," *Journal of Lightwave Technology* (2024).

66. S. Im Sande, et al., "Spin-controlled generation of a complete polarization set with randomly-interleaved plasmonic metasurfaces," *Opto-Electronic Advances* **7**, 240076-240071-240076-240079 (2024).

67. Y. Zhou, et al., "Multilayer noninteracting dielectric metasurfaces for multiwavelength metaoptics," *Nano Letter* **18**, 7529-7537 (2018).

68. P. Naseri and S. V. Hum, "A generative machine learning-based approach for inverse design of multilayer metasurfaces," *IEEE Transactions on Antennas and Propagation* **69**, 5725-5739 (2021).

69. Q. He, et al., "Tunable/reconfigurable metasurfaces: physics and applications," *Research* (2019).

70. X. Zhang, et al., "Reconfigurable metasurface for image processing," *Nano Letter* **21**, 8715-8722 (2021).

71. T. Gu, et al., "Reconfigurable metasurfaces towards commercial success," *Natature Photonics* **17**, 48-58 (2023).

72. C. U. Hail, et al., "Optical metasurfaces: evolving from passive to adaptive," *Advanced Optical Materials* **7**, 1801786 (2019).

73. O. A. M. Abdelraouf, et al., "Recent Advances in Tunable Metasurfaces: Materials, Design, and Applications," *ACS Nano* **16**, 13339-13369 (2022).

74. D.-H. Kwon, et al., "Optical planar chiral metamaterial designs for strong circular dichroism and polarization rotation References and links," *Optics express* **16**, 11802-11807 (2008).

75. T. Cao, et al., "Strongly tunable circular dichroism in gammadion chiral phase-change metamaterials," *Optics Express* **21**, 27841-27841 (2013).
76. J. Hu, et al., "All-dielectric metasurface circular dichroism waveplate," *Scientific Reports* **7**, 41893 (2017).
77. Z. Ma, et al., "All-dielectric planar chiral metasurface with gradient geometric phase," *Optics Express* **26**, 6067-6067 (2018).
78. S. A. Asefa, et al., "Chiral metasurfaces: a review of the fundamentals and research advances," *Applied Sciences* **13**, 10590 (2023).
79. D. Lee, et al., "Metasurfaces-based imaging and applications: from miniaturized optical components to functional imaging platforms," *Nanoscale Advances* **2**, 605-625 (2020).
80. A. John-Herpin, et al., "Metasurface-Enhanced Infrared Spectroscopy: An Abundance of Materials and Functionalities," *Advanced Materials* **35**, 2110163 (2023).
81. J. Yang, et al., "Active optical metasurfaces: comprehensive review on physics, mechanisms, and prospective applications," *Reports on Progress in Physics* **85**, 036101 (2022).
82. Y. Shi, et al., "Optical manipulation with metamaterial structures," *Applied Physics Reviews* **9**, 3 (2022).
83. G. Lee, et al., "The perspectives of broadband metasurfaces and photo-electric tweezer applications," *Nanophotonics* **11**, 1783-1808 (2022).
84. Z. Shen and X. Huang, "A review of optical tweezers with metasurfaces," *Photonics* **10**, 623 (2023).
85. W. T. Chen, et al., "A broadband achromatic metalens for focusing and imaging in the visible," *Nature Nanotechnology* **13**, 220-226 (2018).
86. J. Kepler, "De cometis libelli tres," (1963).
87. J. C. Maxwell, "LI. On physical lines of force," *The London, Edinburgh, and Dublin Philosophical Magazine and Journal of Science* **21**, 338-348 (1861).
88. J. C. Maxwell, "A treatise on electricity and magnetism," *Clarendon Press google schola* **2**, 3408-3425 (1873).
89. P. Lebedev, "Untersuchungen ber die druckkrfte des lichtes," *Annalen der Physik* **311**, 433458 (1901).
90. A. Einstein, "On a heuristic point of view concerning the production and transformation of light," *Annalen der Physik* **17**, 1-16 (1905).
91. A. H. Compton, "A quantum theory of the scattering of X-rays by light elements," *Physical review* **21**, 483 (1923).

92. R. Frisch and O. Stern, "Anomalien bei der spiegelnden Reflexion und Beugung von Molekularstrahlen an Kristallspaltflächen. I," *Zeitschrift für Physik* **84**, 430-442 (1933).
93. A. Ashkin, "Acceleration and trapping of particles by radiation pressure," *Physical review letters* **24**, 156 (1970).
94. A. Ashkin, et al., "Observation of a single-beam gradient force optical trap for dielectric particles," *Optics letters* **11**, 288-290 (1986).
95. K. Svoboda and S. M. Block, "Biological applications of optical forces," *Annual review of biophysics and biomolecular structure* **23**, 247-285 (1994).
96. K. C. Neuman and S. M. Block, "Optical trapping," *Review of scientific instruments* **75**, 2787-2809 (2004).
97. D. G. Grier, "A revolution in optical manipulation," Nature **424**, 810-816 (2003).
98. I. Heller, et al., "Optical tweezers analysis of DNA–protein complexes," Chemical reviews **114**, 3087-3119 (2014).
99. H. Xin, et al., "Optical Forces: From Fundamental to Biological Applications," *Advanced Materials* **32**, 2001994 (2020).
100. A. Magazzù and C. Marcuello, "Investigation of soft matter nanomechanics by atomic force microscopy and optical tweezers: A comprehensive review," *Nanomaterials* **13**, 963 (2023).
101. K. O. Greulich, *Micromanipulation by light in biology and medicine: the laser microbeam and optical tweezers* (Springer Science & Business Media, 2012).
102. O. M. Marago, et al., "Optical trapping and manipulation of nanostructures," *Nature Nanotechnology* **8**, 807-819 (2013).
103. J. Li, et al., "Micro/nanorobots for biomedicine: Delivery, surgery, sensing, and detoxification," *Science robotics* **2**, eaam6431 (2017).
104. A. I. Bunea and J. Glückstad, "Strategies for optical trapping in biological samples: Aiming at microrobotic surgeons," Laser & Photonics Reviews **13**, 1800227 (2019).
105. K. Dholakia and T. Čižmár, "Shaping the future of manipulation," *Nature Photonics* 2011 5:6 **5**, 335-342 (2011).
106. Y. Harada and T. Asakura, "Radiation forces on a dielectric sphere in the Rayleigh scattering regime," *Optics communications* **124**, 529-541 (1996).
107. C. F. Bohren and D. R. Huffman, *Absorption and scattering of light by small particles* (John Wiley & Sons, 2008).
108. L. Novotny and B. Hecht, *Principles of nano-optics* (Cambridge university press, 2012).

109. B. T. Draine and P. J. Flatau, "Discrete-dipole approximation for scattering calculations," *Journal of the Optical Society of America A* **11**, 1491-1499 (1994).

110. A. Taflove, et al., "Computational electromagnetics: the finite-difference time-domain method," *The Electrical Engineering Handbook* **3**, 15 (2005).

111. T. A. Nieminen, et al., "Optical tweezers computational toolbox," *Journal of Optics A: Pure and Applied Optics* **9**, S196 (2007).

112. A. Ashkin and J. P. Gordon, "Stability of radiation-pressure particle traps: an optical Earnshaw theorem," *Optics letters* **8**, 511-513 (1983).

113. Y. Roichman, et al., "Optical forces arising from phase gradients," *Physical review letters* **100**, 013602 (2008).

114. Y.-J. L. Chu, et al., "Measurements of radiation pressure owing to the grating momentum," *Physical review letters* **121**, 063903 (2018).

115. A. S. Swakshar, et al., "Broadband radiation pressure on a small period diffractive film," *Optics Express* **30**, 45279-45287 (2022).

116. G. A. Swartzlander Jr, "Theory of radiation pressure on a diffractive solar sail," *Journal of the Optical Society of America B* **39**, 2556-2563 (2022).

117. J. Siegel, et al., "Self-stabilizing laser sails based on optical metasurfaces," *ACS Photonics* **6**, 2032-2040 (2019).

118. O. Ilic and H. A. Atwater, "Self-stabilizing photonic levitation and propulsion of nanostructured macroscopic objects," *Natature Photonics* **13**, 289-295 (2019).

119. D. Andrén, et al., "Microscopic metavehicles powered and steered by embedded optical metasurfaces," *Nature Nanotechnology* **16**, 970-974 (2021).

120. L. Allen, et al., "Orbital angular momentum of light and the transformation of Laguerre-Gaussian laser modes," *Physical Review A* **45**, 8185 (1992).

121. N. Simpson, et al., "Mechanical equivalence of spin and orbital angular momentum of light: an optical spanner," *Optics letters* **22**, 52-54 (1997).

122. Y, Alison, et al., "Orbital angular momentum: origins, behavior and applications." *Advances in optics and photonics* **3**, 161-204 (2011).

123. Y. Bao, et al., "A Minimalist Single-Layer Metasurface for Arbitrary and Full Control of Vector Vortex Beams," *Advanced Materials* **32**, 6 (2020).

124. M. Padgett and R. Bowman, "Tweezers with a twist," *Natature Photonics* **5**, 343-348 (2011).

125. H. Rubinsztein-Dunlop, et al., "Roadmap on structured light," *Journal of Optics* **19**, 013001 (2016).

126. S. H. Simpson, et al., "Polarization-induced torque in optical traps," *Physical Review A—Atomic, Molecular, and Optical Physics* **76**, 043408 (2007).

127. R. A. Beth, "Direct Detection of the Angular Momentum of Light," *Physical Review* **48**, 471-471 (1935).

128. R. A. Beth, "Mechanical Detection and Measurement of the Angular Momentum of Light," *Physical Review* **50**, 115-125 (1936).

129. A. T. O'Neil, et al., "Intrinsic and Extrinsic Nature of the Orbital Angular Momentum of a Light Beam," *Physical Review Letters* **88**, 053601 (2002).

130. M. Liu, et al., "Light-driven nanoscale plasmonic motors," *Nature Nanotechnology* **5**, 570-573 (2010).

131. V. N. Constantinescu, *Laminar viscous flow* (Springer Science & Business Media, 2012).

132. A. V. Arzola, et al., "Rotation, oscillation and hydrodynamic synchronization of optically trapped oblate spheroidal microparticles," *Optics Express* **22**, 16207-16207 (2014).

133. J. Elgeti, et al., "Physics of microswimmers—single particle motion and collective behavior: a review," *Reports on progress in physics* **78**, 056601 (2015).

134. F. Martinez-Pedrero, et al., "Colloidal Microworms Propelling via a Cooperative Hydrodynamic Conveyor Belt," *Physical Review Letters* **115**, 13 (2015).

135. S. H. Simpson, et al., "Synchronization of colloidal rotors through angular optical binding," *Physical Review A* **93**, 2 (2016).

136. P. Figliozzi, et al., "Driven optical matter: Dynamics of electrodynamically coupled nanoparticles in an optical ring vortex," *Physical Review E* **95**, 2 (2017).

137. A. Modin, et al., "Hydrodynamic spin-orbit coupling in asynchronous optically driven micro-rotors," *Nature Communications* **14**, 1-9 (2023).

138. C. J. Reeves, et al., "Emergence of lanes and turbulent-like motion in active spinner fluid," *Communications Physics* **4**, 92 (2021).

139. H.-W. Huang, et al., "Adaptive locomotion of artificial microswimmers," *Science Advances* **5**, eaau1532 (2019).

140. M. Hippler, et al., "Controlling the shape of 3D microstructures by temperature and light," *Nature Communications* **10**, 232 (2019).

141. Y. Sun, et al., *Field-driven micro and nanorobots for biology and medicine* (Springer, 2022).

142. H. Ceylan, et al., "Mobile microrobots for bioengineering applications," *Lab on a Chip* **17**, 1705-1724 (2017).

143. M. Sitti and D. S. Wiersma, "Pros and Cons: Magnetic versus Optical Microrobots," *Advanced Materials* **32**, 1906766 (2020).

144. A.-I. Bunea, et al., "Light-powered microrobots: challenges and opportunities for hard and soft responsive microswimmers," *Advanced Intelligent Systems* **3**, 2000256-2000256 (2021).

145. W. Yang, et al., "Light-powered microrobots: Recent progress and future challenges," *Optics and Lasers in Engineering* **161**, 107380 (2023).

146. R. Di Leonardo, et al., "Bacterial ratchet motors," *Proceedings of the National Academy of Sciences* **107**, 9541-9545 (2010).

147. A. W. Feinberg, "Biological soft robotics," *Annual review of biomedical engineering* **17**, 243-265 (2015).

148. L. Sun, et al., "Biohybrid robotics with living cell actuation," *Chemical Society Reviews* **49**, 4043-4069 (2020).

149. N. Pellicciotta, et al., "Light controlled biohybrid microbots," *Advanced Functional Materials* **33**, 2214801 (2023).

150. R. S. Rikken, et al., "Manipulation of micro-and nanostructure motion with magnetic fields," *Soft matter* **10**, 1295-1308 (2014).

151. H. Zhou, et al., "Magnetically driven micro and nanorobots," Chemical Reviews **121**, 4999-5041 (2021).

152. N. Ebrahimi, et al., "Magnetic actuation methods in bio/soft robotics," *Advanced Functional Materials* **31**, 2005137-2005137 (2021).

153. P. Sharan, et al., "Microfluidics for microswimmers: engineering novel swimmers and constructing swimming lanes on the microscale, a tutorial review," *Small* **17**, 2007403 (2021).

154. Q. Wang and L. Zhang, "External power-driven microrobotic swarm: from fundamental understanding to imaging-guided delivery," *ACS Nano* **15**, 149-174 (2021).

155. T. D. Edwards and M. A. Bevan, "Controlling colloidal particles with electric fields," *Langmuir* **30**, 10793-10803 (2014).

156. J. Chen, et al., "Thermal optofluidics: principles and applications," *Advanced Optical Materials* **8**, 1900829 (2020).

157. K. J. Rao, et al., "A force to be reckoned with: a review of synthetic microswimmers powered by ultrasound," *Small* **11**, 2836-2846 (2015).

158. Y. Xiao, et al., "Acoustics-actuated microrobots," *Micromachines* **13**, 481-481 (2022).

159. J. Wang, et al., "Light-driven micro/nanomotor for promising biomedical tools: principle, challenge, and prospect," *Accounts of chemical research* **51**, 1957-1965 (2018).

160. S. Jones, et al., "Photothermal heating of plasmonic nanoantennas: influence on trapped particle dynamics and colloid distribution," *ACS Photonics* **5**, 2878-2887 (2018).

161. S. Jones, et al., "Strong transient flows generated by thermoplasmonic bubble nucleation," *ACS Nano* **14**, 17468-17475 (2020).

162. M. Lahikainen, et al., "Tunable photomechanics in diarylethene-driven liquid crystal network actuators," *ACS Applied Materials & Interfaces* **12**, 47939-47947 (2020).

163. P. F. Luo, et al., "Photomechanical polymer hydrogels based on molecular photoswitches," *Journal of Polymer Science* **59**, 2246-2264 (2021).

164. M. Herath, et al., "Light activated shape memory polymers and composites: A review," *European Polymer Journal* **136**, 109912 (2020).

165. S. Yu, et al., "Recent progress on motion control of swimming micro/nanorobots," *View* **2**, 20200113 (2021).

166. P. Y. Chiou, et al., "Massively parallel manipulation of single cells and microparticles using optical images," *Nature* **436**, 370-372 (2005).

167. S. Zhang, et al., "Reconfigurable multi-component micromachines driven by optoelectronic tweezers," *Nature Communications* **12**, 5349 (2021).

168. S. Liang, et al., "A versatile optoelectronic tweezer system for micro-objects manipulation: transportation, patterning, sorting, rotating and storage," *Micromachines* **12**, 271 (2021).

169. S. Zhang, et al., "Optoelectronic tweezers: a versatile toolbox for nano-/micro-manipulation," *Chemical Society Reviews* **51**, 9203-9242 (2022).

170. G. Vizsnyiczai, et al., "Light controlled 3D micromotors powered by bacteria," *Nature Communications* **8**, 15974 (2017).

171. S. Bianchi, et al., "An optical reaction micro-turbine," *Nature Communications* **9**, 4476 (2018).

172. D. J. Stevenson, et al., "Light forces the pace: optical manipulation for biophotonics," *Journal of biomedical optics* **15**, 041503-041503-041521 (2010).

173. I. Minin, et al., "Optical manipulation of micro-and nanoobjects based on structured mesoscale particles: a brief review," *Atmospheric and Oceanic Optics* **33**, 464-469 (2020).

174. Y. Y. Tanaka, et al., "Plasmonic linear nanomotor using lateral optical forces," *Science Advances* **6**, eabc3726 (2020).

175. X. F. Wu, et al., "Light-driven microdrones," *Nature Nanotechnology* **17**, 477-+ (2022).

176. U. G. Būtaitė, et al., "Indirect optical trapping using light driven micro-rotors for reconfigurable hydrodynamic manipulation," *Nature Communications* **10**, 1215-1215 (2019).

177. D. M. Sullivan, *Electromagnetic simulation using the FDTD method* (John Wiley & Sons, 2013).

178. R. Gao, et al., "Dynamically stable radiation pressure propulsion of flexible lightsails for interstellar exploration," *Nature Communications* **15**, 4203 (2024).